MEASUREMENTS OF Cd AND Hg ORGAN BURDENS USING PGNAA AND XRF

MEASUREMENTS OF CADMIUM AND MERCURY ORGAN BURDENS USING PROMPT GAMMA NEUTRON ACTIVATION ANALYSIS AND X-RAY FLUORESCENCE

By

JOANNA GRINYER, B.Sc.

A Thesis

Submitted to the School of Graduate Studies

in Partial Fulfilment of the Requirements

for the Degree

Doctor of Philosophy

McMaster University

DOCTOR OF PHILOSOPHY (2008)
(Medical Physics)

McMaster University
Hamilton, Ontario

TITLE: MEASUREMENTS OF CADMIUM AND MERCURY ORGAN BURDENS USING PROMPT GAMMA NEUTRON ACTIVATION ANALYSIS AND X-RAY FLUORESCENCE

AUTHOR: Joanna Grinyer

SUPERVISOR: David R. Chettle

NUMBER OF PAGES: xi, 113

ABSTRACT

This thesis describes the development and improvement of prompt gamma neutron activation analysis and x-ray fluorescence techniques with the goal of reducing the minimum detection limit of cadmium and mercury for non-invasive measurement of occupationally exposed individuals. The detection of cadmium in the liver and kidneys with prompt gamma neutron activation analysis was investigated in this thesis. The cadmium minimum detection limit was determined to be 1.7 mg in the kidney and 3.3 ppm in the liver. This represents a reduction in the minimum detection limit by a factor of 2 in the kidney and 1.4 in the liver, and this improvement was achieved through optimization of a ^{238}Pu-Be-based prompt gamma neutron activation analysis system at McMaster University. This system is now ready for *in vivo* measurement of cadmium-exposed workers, and possibly for individuals with high levels of environmental exposure. The prompt gamma neutron activation analysis technique was determined to be unsuitable for *in vivo* mercury measurement in the kidney due to a high detection limit of 315 ppm. This figure was a factor of 23 worse than the detection limit of cadmium in the kidney, when a factor of 10 worse was expected. A comparison was made of mercury and cadmium to chlorine, which is a well-known neutron activation element, and the source of discrepancy was determined to be the enhanced detectability of cadmium due to the non-thermal nature of the ^{238}Pu-Be neutron energy spectrum and the non-$1/\nu$ behaviour of the cadmium thermal neutron capture cross-section. Since the prompt gamma neutron activation analysis technique was not sensitive enough for mercury detection, a source-based x-ray fluorescence system was developed. This system is based on a ^{109}Cd source that emits 88 keV gamma-rays, a source collimator and planar hyperpure germanium detector in a backscatter (approximately 180°) geometry. Minimum detection limits of 3.9 ppm

for a bare kidney phantom and 5.0 ppm for a kidney phantom at 1 cm depth in a torso phantom were obtained. The planar detection system reduced the bare phantom minimum detection limit by a factor of 11 compared to previous source-based x-ray fluorescence studies, however the torso phantom minimum detection limit remains comparable to that of polarized x-ray fluorescence studies. Attempts at improving the mercury minimum detection limit with a cloverleaf detection system (detector consisting of four electronically separate hyperpure germanium crystals) and stronger gamma-ray source were not successful, and currently both the planar and cloverleaf detection systems have a similar minimum detection limit of about 5 ppm at 1 cm kidney depth. In addition, the *in vivo* measurement of two patients with possible mercury exposure using the cloverleaf x-ray fluorescence system is discussed.

Acknowledgements

First and foremost I would like to thank Dr. David Chettle for being my mentor throughout my graduate studies. I am honoured to have worked with David who is a great and experienced researcher. I am grateful for his words of encouragement and his patience in answering even the most naive question from a young researcher. David has taught me to be a better scientist and a better person, and without him, this thesis would not be possible.

I must acknowledge my supervisory committee, Dr. Soo-Hyun Byun, Dr. Joanne O'Meara and Dr. Bill Prestwich, for their direction and help in shaping my research project. Their experience and insight was invaluable. In particular, I am grateful to Byun for his help in the preliminary stages of my research, and for always being there in case I had a question.

There are many more wonderful people that need to be mentioned. I would like to thank Dr. Fiona McNeill for many invaluable discussions, all of the members of the Occupational Nuclear Medicine Research Group, Wendy Malarek, Fiona Ahlang and Vera Iarossi for helping with the administrative side of research, Norbert Boehling for his help in many of my computer disasters, and Scott McMaster, John Cave and Jason Falladown for their help at the accelerator lab.

I am grateful to my husband Geoff for all his love, constant support and

understanding, to my baby daughter Daniela for her smiles during the tough times and for making my work even more worthwhile, and to my family in Poland and Pennsylvania for all their good wishes. Of course I must mention Cleo, my faithful companion and loving troublemaker, whom I get to take on walks everyday and think about life and research.

Contents

List of Tables

List of Figures

Chapter 1

Introduction

Heavy metals such as cadmium or mercury occur naturally in the environment in small amounts. They are an innate ingredient in soil, rocks and water and are not harmful if present in low natural concentrations. Some parts of the world have higher natural soil concentrations of cadmium, such as central Canada, east Arctic and Jamaica (Howe *et al.*, 2005, Riget *et al.*, 2005)). Natural mercury levels are elevated in regions such as west Arctic, Great Lakes region, Gulf of Mexico and the Atlantic Ocean (Riget *et al.*, 2005, US Geological Survey). However, due to certain human activities the concentrations of these metals can increase due to ingestion or inhalation. Exposure to larger than natural amounts of cadmium or mercury can have a detrimental effect on human health. This is particularly true in occupational settings where workers can be acutely or chronically exposed and monitoring of exposure is essential. This thesis focuses on non-invasive methods which allow for monitoring of chronic worker exposure to cadmium or mercury by measuring the organ burdens of these metals.

1.1 Cadmium

Cadmium is a soft bluish-white metal with an atomic number, Z, of 48. It is a Group IIB metal with chemical properties similar to zinc and mercury. Cadmium is typically found in the +2 oxidation state. Cadmium has a density of 8.65 g cm^{-3} at room temperature, a melting point 321°C and a boiling point of 767°C (CRC Handbook, 2007). Naturally occurring cadmium isotopes are listed in Table 1.1, and are found in the soil, rocks and oceans, usually with zinc. Most cadmium is obtained as a by-product from the refinement of zinc ores. In fact, cadmium was discovered in 1817 during the purification of zinc carbonate. Since its relatively recent discovery, it has become widely used in a variety of products such as nickel-cadmium batteries, pigments, alloys, soldering materials and stabilizers for plastics to name a few. Cadmium is toxic to humans and due to its dispersal through increased industrial use has become an environmental pollutant as well as a source of occupational exposure.

Table 1.1: Natural cadmium isotopes (Table of Nuclides).

Isotope	Natural abundance (%)	Isotope	Natural abundance (%)
^{106}Cd	1.25	^{112}Cd	24.13
^{108}Cd	0.89	^{113}Cd	12.22
^{110}Cd	12.49	^{114}Cd	28.73
^{111}Cd	12.80	^{116}Cd	7.49

1.1.1 Human exposure to cadmium

Cadmium is a natural component in rocks and soil, and is therefore ingested as part of the human diet due to its uptake by crops. The largest source of environmental exposure to cadmium comes from ingestion of food that is grown in naturally cadmium-containing soil. Two-thirds of ingested cadmium comes from plant products and the remainder from animal products. Typical amounts ingested from dietary sources amount to 10 to 30 μg per day (Satarug and Moore, 2004). In addition, tobacco is a major source of exposure to smokers, with cadmium amounts inhaled from tobacco smoke exceeding normal ingested amounts. In fact, kidney levels are 2 to 3 times greater in smokers than non-smokers (Satarug and Moore, 2004). The use of cadmium in industry has led to additional deposition of cadmium into air, soil and water due to environmental pollution, and subsequent contamination of food sources.

Increased industrial use of cadmium has led to occupational exposure becoming a significant concern in industrial activities such as cadmium and nickel mining, production and recycling of nickel-cadmium batteries, soldering, zinc smelting, and pigment production. The largest contemporary usage of cadmium is in nickel-cadmium batteries. For occupational exposure, inhalation of cadmium oxide fumes is the main pathway for both acute and chronic exposure.

1.1.2 Health effects of cadmium

The most common routes of exposure are ingestion and inhalation of cadmium. Cadmium absorption due to ingestion is approximately 5%, although certain individuals are predisposed to a 20 to 30% absorption rate due to the increased expression of a metal transporter protein (Satarug and Moore, 2004). Inhalation of cadmium leads to a 10 to 50% absorption rate depending on the particle size. This difference in

absorption rates between inhaled and ingested cadmium is one of the reasons cadmium levels in smokers are higher than non-smokers for non-occupationally exposed populations.

Once cadmium enters the bloodstream from either the gastrointestinal tract or the lung, it travels to the liver where it stimulates the production of a protein called cadmium metallothionein. This protein travels directly to the kidneys where it binds with excreted cadmium to form a complex that is then re-absorbed by the kidney. This mechanism leads to an accumulation of cadmium in the kidneys with a biological half-life of about 30 years (Friberg, 1984). The total cadmium in the body at 50 years of age for a non-occupationally exposed individual is approximately 50 mg. Of this, one half is found in the kidneys (mostly the cortex), one sixth in the liver and the rest throughout the body (Friberg, 1984, Satarug and Moore, 2004). Cadmium levels in occupationally exposed individuals are higher than those of the general public and can greatly vary, with upper limits reaching 600 ppm in the kidney and 120 ppm in the liver (Börjesson *et al.*, 1998). Typically, cadmium is introduced into the body through long-term exposure at low concentrations, hence the discussion of health effects will be of the chronic effects of cadmium.

Kidney dysfunction occurs when cadmium levels increase such that not enough metallothionein is produced to capture cadmium, and this is when cadmium becomes toxic. This can occur at cadmium levels as low as 50 ppm (Satarug and Moore, 2004). Renal symptoms include proteinuria (excretion of protein in urine), increased calcium excretion, dysuria (painful and difficult urination), and polyuria (frequent urination). Symptoms of more severe damage can include pain in the location of the kidneys. Irreversible kidney damage can occur before symptoms are present. At very high cadmium concentrations, the kidney is sufficiently damaged that accumulated

cadmium is excreted and the kidney is not capable of re-absorbing it. It is worth mentioning that heavily exposed populations such as people with Itai-itai disease (a disease with numerous symptoms resulting from cadmium poisoning) have up to 2.5 times higher liver concentrations compared to kidney concentrations (Uetani *et al.*, 2006).

Other chronic effects include emphysema and related shortness of breath, which may lead to an early death. In addition, cadmium inhibits the absorption of calcium in the kidneys, leading to increased calcium urinary secretion and subsequent alteration of vitamin D metabolism. Also, the presence of cadmium in bone is thought to accelerate calcium and phosphate loss in bone and to impair bone mineralization (Wittman and Hu, 2002). These processes may lead to osteoporosis (loss of bone tissue) and osteomalacia (softening of the bones). Cadmium is thought to be a carcinogen as an increase in lung and prostate cancer has been observed for exposed individuals, although the evidence is not conclusive (Wittman and Hu, 2002).

1.1.3 Monitoring of occupational exposure

Cadmium accumulates in the kidney and liver and thus these sites are particularly important in occupational cadmium monitoring. Biomonitoring of cadmium in the workplace is commonly done through blood and urine concentration measurements. The biological half-life of cadmium in the blood is between 75 and 130 days, and anywhere from months to years in the urine (Börjesson *et al.*, 1998). However, blood and urine concentrations are influenced by recent exposure and therefore may not reflect the total organ burden. In the case of urine monitoring, kidney damage may lead to increased cadmium excretion and may alter the results. In order to prevent adverse health effects described above and especially irreversible kidney damage, it is

crucial to measure the total organ burden in the kidney and liver where the majority of cadmium accumulates. One method involves performing a biopsy to obtain the concentration in the organ, however such an invasive procedure carries risk for the patient and is not practical for regular monitoring of workers. Another method to measure the total organ burden is to use a non-invasive *in vivo* technique such as prompt gamma neutron activation analysis or x-ray fluorescence. Both methods are discussed in detail in Sections 1.3 and 1.6.

Prompt gamma neutron activation analysis can be used to detect cadmium in the kidneys and liver. The main advantage of this method is the large thermal neutron capture cross-section of ^{113}Cd, and the relatively high energy prompt gamma-ray at 559 keV (compared to characteristic x-ray energy of cadmium, see below). This means that the depth of the kidney and liver will not greatly affect the detectability of cadmium, due to the penetrability of thermal neutrons and relatively small attenuation of the emitted gamma-ray. This technique is useful for measuring the total organ burden of cadmium. To date, many groups have detected cadmium *in vivo* in the kidney and liver. A summary of these results is listed in Table 1 of Chapter 2.

X-ray fluorescence is not practical for a site such as the kidney or liver due to the depth of these organs. The K-edge of cadmium is 26.71 keV, so in order to maximize the photoelectric cross-section one must use photons with an energy just above the K-edge energy. Since the thickness of tissue overlying the kidney can be about 5 cm, this would lead to a significant attenuation of incoming photons. Similarly, emitted characteristic K x-rays have an even lower energy (23.17 keV or less) that would be attenuated by tissue. To date, only one group has measured kidney cadmium by polarized *in vivo* x-ray fluorescence and obtained a detection limit of 8 ppm at 30 mm of overlying tissue (Christoffersson and Mattsson, 1983).

This detection limit rises rapidly for greater tissue thicknesses due to the attenuation of incoming and emitted photons. In addition, the majority of cadmium signals come from the outermost layer of the kidney and only a small portion of the signal comes from deeper layers, and thus using x-ray fluorescence does not give the total kidney burden as in the case of neutron activation.

1.2 Mercury

Mercury is a silvery liquid metal at room temperature with a density of 13.534 g cm^{-3} at room temperature. The melting point of mercury is -38.83°C and it has a boiling point of 356.73°C (CRC Handbook, 2007). The atomic number of mercury is 80, it belongs to group IIB of the periodic table, and typically is found in a +2 oxidation state. Naturally occurring isotopes of mercury are tabulated in Table 1.2.

Table 1.2: Natural mercury isotopes (Table of Nuclides).

Isotope	Natural abundance (%)	Isotope	Natural abundance (%)
^{196}Hg	0.15	^{201}Hg	13.18
^{198}Hg	9.97	^{202}Hg	29.86
^{199}Hg	16.87	^{204}Hg	6.87
^{200}Hg	23.10		

Volcanic eruptions are a major source of natural mercury in the atmosphere and soil. Most commonly, mercury is found as cinnabar ore (HgS) in nature. Since the industrial age, the levels of mercury in the environment have increased due to its use in various industries such as battery production, gold and other metal smelting, dentistry and as a by-product of coal-burning. In addition, mercury enters the environment via

landfills and waste incineration. Mercury has long been known to be detrimental to human health and is a significant source of occupational exposure in various industries.

1.2.1 Human exposure to mercury

Trace amounts of mercury are normally present in the human body from dietary sources. As a result of wide usage of mercury in industrial activities it can be a source of exposure to workers and to the public. Exposure to the public occurs when mercury is released into the environment as a result of industrial activity or natural phenomena such as volcanic activity. It is estimated that 3000 tonnes of mercury per year are released due to industrial activity worldwide (WHO 1991). There are two main forms of mercury: organic and inorganic. Mercury in either organic or inorganic form can cause a number of adverse health effects. Organic mercury contributes to environmental exposure and is introduced into the body as methylmercury from the food chain, water or air. Ingestion of mercury-containing seafood is of particular concern, especially for pregnant and nursing mothers. Inorganic mercury comes from industrial sources in the forms of elemental mercury and its vapour, and is the source of both acute and chronic occupational exposure.

Metallic mercury or "quicksilver" can pose health risks if inhaled as a vapour. Similarly, mercury vapour from dental amalgams can be inhaled, but a clear impact of amalgams on health has not been proven. The most common form in occupational exposure is the inhalation of mercury vapours. Exposure occurs in a variety of industries such as mercury mining, gold mining and refining, metal sulfide ore smelting, cement production, chloroalkali and thermometer factories, production and handling of dental amalgam and refuse incineration (WHO 1991, Börjesson *et al.* 1998).

1.2.2 Health effects of inorganic mercury

One purpose of this thesis is to develop measurement techniques to make it possible to monitor the extent of chronic occupational exposure in order to prevent possible adverse health effects of mercury. Therefore the discussion of health effects is confined to those that result from low-concentration, long-term inhalation of inorganic mercury as opposed to environmental exposure to the public from organic mercury.

Mercury vapour is absorbed by the lungs, crosses lung cell membranes and enters the bloodstream and interstitial body fluids where it is oxidized to form mercury ions (WHO 1976). It is then distributed throughout the body where it accumulates primarily in the kidneys, and to a much lesser extent in the liver and brain. Approximately 50 to 90% of inhaled mercury vapour is deposited in the kidneys according to animal models (WHO 1991), however, the details of the mechanism by which mercury is absorbed in the kidney are not well known (Clarkson and Magos, 2006). Ingestion of metallic mercury leads to negligible absorption (less than 1%) by the gastrointestinal tract. Elimination of mercury from the body takes place via urine and faeces. The biological half-life of mercury in the body varies widely among different tissues. In blood, the biological half-life ranges between 3 and 45 days. In urine, it is 40 to 90 days with a long-term component on the scale of years. The biological half-life is 40 to 60 days for the whole body, 20 days for the brain (although a long-term component may be present) and 50 to 200 days in the kidney (Börjesson, 1998).

Typical mercury levels in occupationally exposed individuals cover a wide range of values. A case study on a deceased worker at the end of a 14-year period of occupational exposure show tissue concentrations of 25 ppm in the kidney, 1.2 ppm in the liver, 0.72 ppm in the lung and 0.014-0.018 ppm in the cerebellum (Barregard *et al.*, 1999). These values are typical for occupationally exposed individuals, with

the exception of the unusually low cerebellum concentration. More representative cerebellum concentrations are on the order of 0.2-2 ppm (Kosta *et al.*, 1975). In the general population, typical kidney levels are 1 ppm or less.

Chronic exposure to low levels of mercury can lead to proteinuria and kidney damage as mercury accumulates in the kidney (WHO, 1991). Mercury levels on the order of 25 ppm have been associated with nephrotic syndrome (Kazantis, 1962). Nephrotic syndrome includes glomerular and tubular damage, albuminuria (albumin present in the urine) and edema. In many cases, irreversible damage to the kidney occurs before symptoms are noticed. Other chronic effects include mild tremor, vision impairment, memory loss and irritability, but mercury levels that cause these neurological problems are unknown (Clarkson and Magos, 2006). There is a possibility that occupational exposure to mercury can cause lung damage, and autoimmune diseases, but conclusive evidence is lacking. Due to the unclear relationship between urine and kidney levels and the onset of symptoms, as well as the possibility of some individuals being more sensitive to mercury exposure (WHO, 1991), it is difficult to assign a threshold at which symptoms of exposure start.

1.2.3 Monitoring of occupational exposure

The most common method of monitoring occupational exposure to mercury is through blood and urine sampling. It is believed that mercury urine levels reflect the total kidney burden (Magos and Clarkson, 2006), however it is unknown if this is true in humans. Furthermore, mercury blood and urine levels are heavily influenced by recent exposure to this element and the presence of methylmercury from dietary sources. Also, urinary elimination of mercury may change if the kidney is damaged and may further confound the relationship between mercury urine and kidney content

(Börjesson *et al.*, 1995).

Since kidneys contain the most mercury in the body, they are the best site at which to monitor occupational exposure. In order to monitor for mercury exposure effectively, one requires a non-invasive *in vivo* method which reflects the kidney burden of mercury without any assumptions about the relationship between urine and kidney mercury. By measuring the kidney burden of workers, prevention of kidney damage and other adverse health effects can be possible. Since the threshold values that cause certain health effects are uncertain, future measurement of mercury burdens and correlation with symptoms may help determine the levels of mercury which cause various conditions related to exposure.

Both prompt gamma neutron activation and x-ray fluorescence have been used to detect mercury in the kidney non-invasively. In a study by Smith *et al.*, 1982, a cyclotron beam was used to produce neutrons with a mean energy of 2.5 to 3 MeV. The proton beam from the cyclotron was pulsed to increase the signal to noise ratio in the prompt gamma spectrum that was collected by irradiating a kidney phantom within a water tank torso phantom. A 15% efficient (relative to a 7.6 cm by 7.6 cm NaI detector) Ge(Li) detector was used to collect the spectra resulting in a kidney detection limit of 54 ppm. This result is too high to perform *in vivo* measurements of occupationally exposed individuals, except in cases of extremely high exposure. Recall that occupationally exposed individuals are on the order of only 25 ppm. In the same study, x-ray fluorescence measurements with a ^{57}Co source and 85° detection geometry on bare kidney phantoms yielded a detection limit of 44 ppm. Again, this detection limit is unsuitable for meaningful *in vivo* measurements.

Using polarized x-rays to perform x-ray fluorescence has improved the detection limit of mercury by approximately a factor of 2. The main advantage of

polarizing the x-ray beam is to reduce the background counts thereby giving a higher signal to noise ratio and a lower detection limit. In one study with polarized x-ray fluorescence, a detection limit of 25 ppm was obtained (Börjesson *et al.*, 1995). Here, an x-ray therapy apparatus was modified by plane polarizing the beam with an aluminum target for a 90° detection geometry. Upon measuring chloroalkali plant and thermometer factory workers, several workers exceeded the kidney detection limit. However, the relatively high detection limit meant that an exact kidney concentration could not be measured. A similar polarized x-ray fluorescence study at McMaster University obtained a detection limit of 26 ppm after optimization of the polarized x-ray fluorescence apparatus (O'Meara *et al.*, 2000).

The detection limit of mercury is currently too high to perform meaningful *in vivo* measurements of occupationally exposed workers. A kidney detection limit of 10 ppm or less is desired as kidney damage has been observed at these mercury levels. In order to lower the detection limit of mercury, two methods were explored in this thesis: prompt gamma neutron activation and x-ray fluorescence.

1.3 Prompt gamma neutron activation analysis

Prompt gamma neutron activation analysis (PGNAA) is based on a radiative capture or (n,γ) reaction. In this method, thermal neutrons are used as a probe to detect material of interest in a sample. Neutrons are captured by the nucleus of the atom in question, and this is followed by emission of gamma-rays by the excited product nucleus. In PGNAA, the emission of gamma-rays following neutron capture takes place almost simultaneously with the neutron capture, as the excited state of the reaction product typically has a half-life on the order of pico-seconds. For example,

the first excited state in ^{114}Cd has a half-life of 10 pico-seconds.

The main advantage of using neutrons for *in vivo* detection is that slow ($E \leq 0.5$ eV) and thermal neutrons ($E \simeq 0.025$ eV) penetrate low Z materials like those found in human tissue and mostly undergo elastic scattering with the medium. This is advantageous for the *in vivo* measurement of organs such as kidneys and liver that can have a significant thickness of overlying tissue. Since very low neutron energies are required, the Q-value of the reaction (n,γ) has to be positive, and the thermal neutron capture cross-section has to be large enough in order for detection to be possible. One disadvantage of PGNAA for *in vivo* measurements is that detection of the gamma-rays has to take place simultaneously with the activation. Background generated by neutron activation of all other elements in the body can lead to a lower measurement sensitivity. This is particularly true for soft tissue and water due to the generation of a 2.223 MeV gamma-ray and its Compton continuum from the ^{1}H(n,γ)^{2}H reaction. For this work, hyperpure germanium (HPGe) detectors were used, because of the required high resolution (approximately 2 keV at 1.332 MeV) to detect full-energy photopeaks generated by cadmium and mercury. An n-type HPGe was used due to the fact that neutron damage can be largely repaired by annealing the detector. In addition to the (n,γ) background, the interaction of neutrons in the germanium detector itself gives rise to additional gamma-rays. Long-term exposure of the detector to neutrons reduces the detector resolution, and regular annealing is required.

1.3.1 Neutron source for prompt gamma neutron activation analysis

The neutron source for PGNAA of cadmium and mercury consists of a ^{238}Pu-Be source encased in a collimation and shielding assembly. The ^{238}Pu-Be source has a half-life of 87.4 years and is composed of two separate sources with a combined activity of 17.4 Ci (640 GBq) with a neutron emission rate of approximately 4×10^7 s^{-1}. The source emits a spectrum of neutron energies up to 11 MeV, with an average neutron energy of approximately 4 MeV. The ^{238}Pu-Be neutron spectrum is shown in Figure 1.1. Fast neutrons emitted are moderated, i.e. slowed down by a Be premoderator and by the water tank phantom placed in front of the collimator so that a relatively large amount of neutrons are thermalized such that they can undergo thermal neutron capture by cadmium or mercury. Despite this, there is a large portion of neutrons with higher energies and as such they do not contribute to the reaction and only contribute to the total dose.

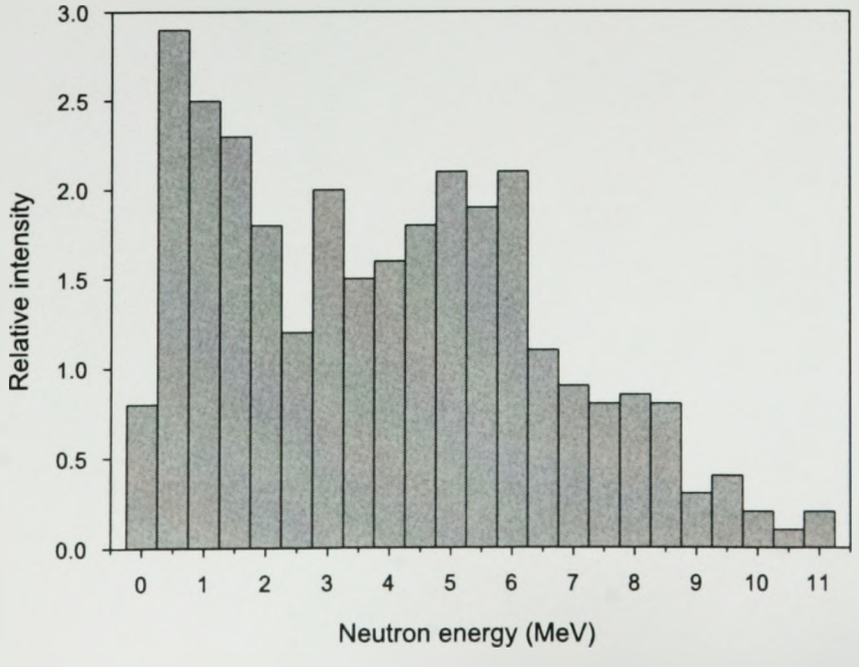

Figure 1.1: ^{238}Pu-Be neutron source spectrum (Block *et al.*, 1967).

The collimation and shielding assembly houses the removable ^{238}Pu-Be neutron source. A beryllium premoderator is encased in an aluminum can and its function is to soften the neutron spectrum while simultaneously acting as a neutron multiplier via the ^{9}Be(n,2n)^{8}Be reaction. Surrounding the neutron source and beryllium premoderator is a central steel tube (9 cm inner diameter), which in turn is surrounded by a graphite block. These are surrounded by alternating layers of steel and high density polyethylene. Within the collimator, a gamma-ray shield for the detector is composed of lead, hevimet (tungsten alloy) and bismuth blocks. The entire assembly is encased in borated resin shielding surrounded by a vinyl cover and is approximately 1 m^3 in size. The apparatus including the ^{238}Pu-Be source is portable although it first must be disassembled and transported in parts. The source can be removed and placed in a steel drum filled with a borax/parrafin mixture for storage or transportation. The partially disassembled collimator is pictured in Figure 1.2.

Figure 1.2: Portable ^{238}Pu-Be neutron source shielding apparatus. Above: assembled collimator surrounded by borated resin plates, below: partially assembled collimator, with visible steel and graphite cylinder, and alternating steel and polyethylene plates.

1.3.2 Prompt gamma neutron activation analysis of cadmium

One isotope of cadmium, ^{113}Cd, has a relatively large thermal neutron capture cross-section of 20,600 b compared to other elements which typically have cross-sections of about 1 b. The natural abundance of ^{113}Cd is 12.22% (see Table 1.1 and 1.3), and thus the elemental cross-section is about 2500 b. Although other isotopes of cadmium have large natural abundances, their cross-sections are too small for *in vivo* measurement of trace amounts of cadmium (see Table 1.3). Thus, ^{113}Cd is the only feasible candidate for successful neutron activation.

Table 1.3: Thermal neutron cross-sections of Cd isotopes (IAEA Database for PG-NAA).

Isotope	Natural abundance (%)	σ (b)	Elemental σ (b)
^{110}Cd	12.49	11	1.37
^{111}Cd	12.80	24	3.07
^{113}Cd	12.22	20600	2517

Prompt gamma neutron activation of cadmium is based on the neutron capture reaction by ^{113}Cd:

$$^{113}\mathrm{Cd} + \mathrm{n} \rightarrow {}^{114}\mathrm{Cd}^{*} \rightarrow {}^{114}\mathrm{Cd} + \gamma \tag{1.1}$$

The most intense gamma-ray emitted following the de-excitation of ^{114}Cd has an energy of 559 keV. Other gamma-rays emitted such as the 651 keV gamma-ray are less intense and are not used in the detection of cadmium (see Table 1.4). At low levels of exposure in an occupational setting one would expect to see the most intense gamma-ray at 559 keV gamma-ray only. Figure 1.3 shows a typical gamma-ray

spectrum following thermal neutron capture by ^{113}Cd using a water phantom filled with 160 ppm of ^{113}Cd. The largest contribution to the background under the 559 keV peak is from the Compton continuum of the 2.223 MeV peak from ^{1}H(n,γ)^{2}H. In the vicinity of the 559 keV peak, the spectrum also contains a 478 keV gamma-ray peak from ^{10}B, a 511 keV annihilation peak, and a 596 keV peak from the inelastic neutron scatter with ^{76}Ge in the detector itself (see Figure 1.4). The dominant feature in Figure 1.4 is the Doppler-broadened 478 keV gamma-ray photopeak from the recoiling ^{7}Li emitted following the ^{10}B(n,α)^{7}Li* reaction. The methodology of *in vivo* PGNAA of cadmium is described in detail in Chapter 2. The neutron source used for activation is described in Section 1.3.1.

Table 1.4: Prompt gamma-rays emitted by ^{114}Cd following thermal neutron capture (National Nuclear Data Center). Only those with relative intensities greater than 5% are listed. I_{max} refers to gamma-rays emitted per neutron capture, and has a value of 72.7% (Berkeley National Laboratory).

E (keV)	I/I_{max} (%)	E (keV)	I/I_{max} (%)
559	100.00	806	5.87
576	6.01	1209	5.5
651	18.94	1364	6.2
725	5.99		

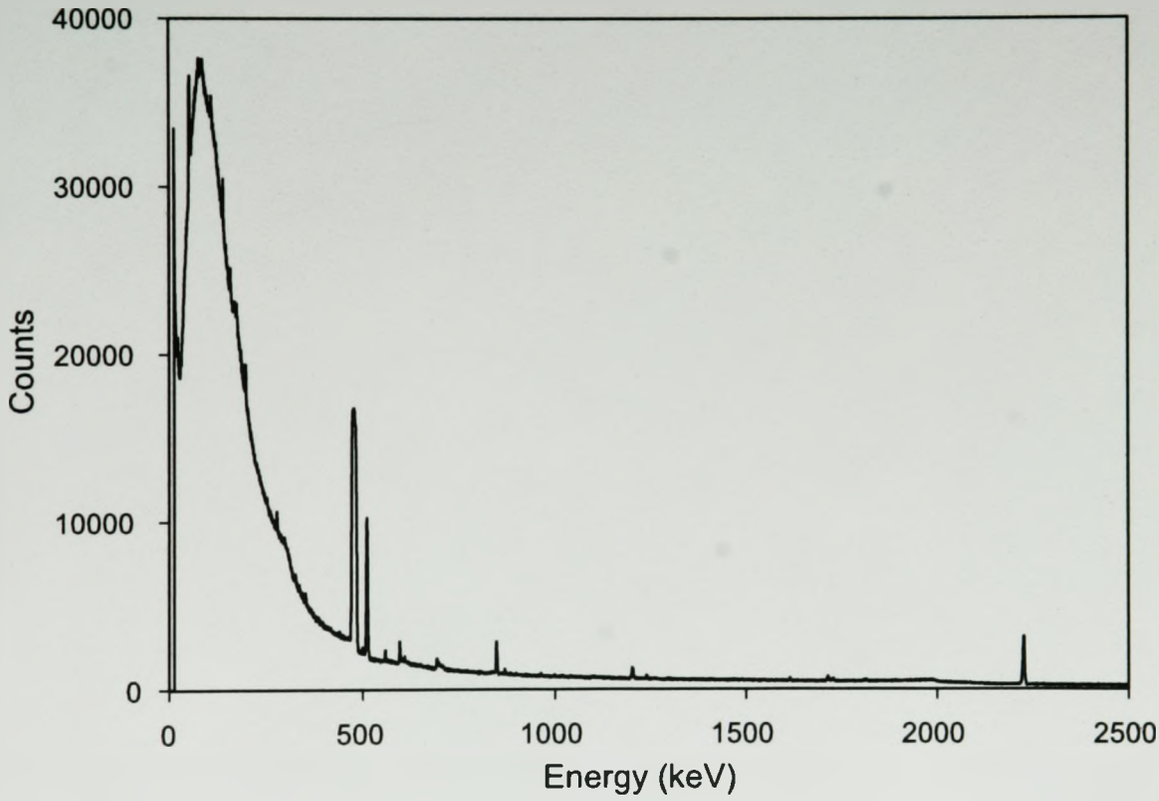

Figure 1.3: A typical prompt gamma neutron activation gamma-ray spectrum showing a range of gamma-ray energies from 0 to 2500 keV. This spectrum was collected with a 160 ppm Cd liver phantom inside a water tank phantom for 2000 s live time.

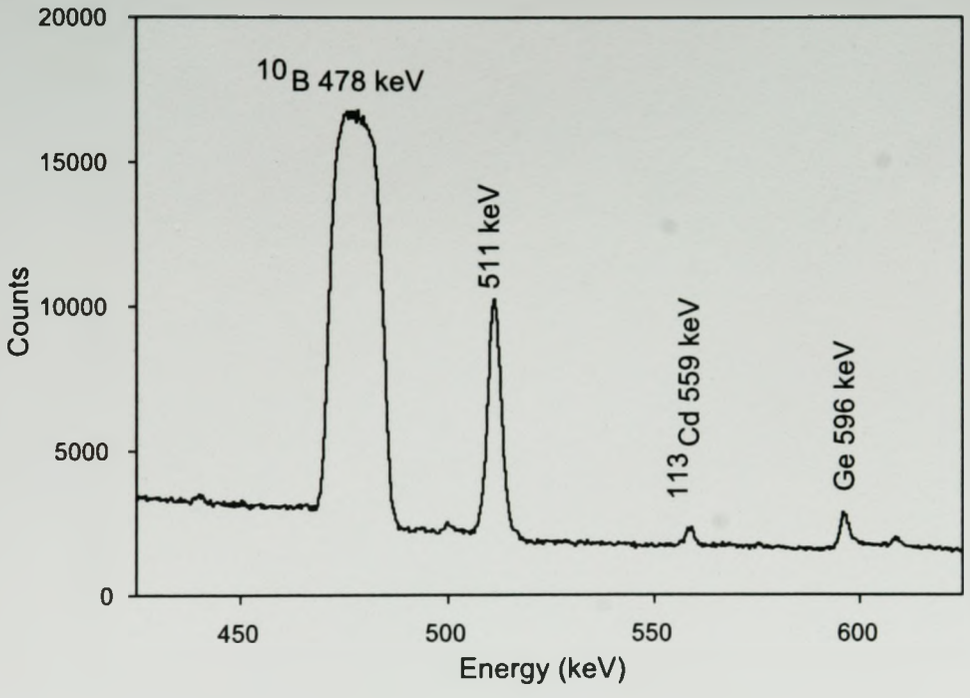

Figure 1.4: Neutron activation spectrum showing the Cd 559 keV gamma-ray collected for 2000 s live time with a 160 ppm liver phantom. Other nearby features include a ^{10}B 478 keV gamma-ray, an annihilation peak at 511 keV and and Ge inelastic scatter peak at 596 keV.

1.3.3 Prompt gamma neutron activation analysis of mercury

Measurement of mercury *in vivo* is also possible due to the relatively large thermal neutron cross-section of ^{199}Hg of 2150 b. Since the natural abundance is 16.87%, the elemental cross-section is 363 b. Although this is much smaller than the cross-section of ^{113}Cd, it is still larger than the cross-sections of typical elements in the body and is significant for use in *in vivo* measurements. Other isotopes of mercury have much smaller elemental cross-sections or a much lower abundance, therefore ^{199}Hg is the isotope through which PGNAA is possible (see Table 1.5). The thermal neutron capture reaction in this case is:

$$^{199}\mathrm{Hg} + \mathrm{n} \rightarrow {}^{200}\mathrm{Hg}^{*} \rightarrow {}^{200}\mathrm{Hg} + \gamma \tag{1.2}$$

Table 1.5: Thermal neutron cross-sections of Hg isotopes (IAEA Database for PGNAA).

Isotope	Natural abundance (%)	σ (b)	Elemental σ (b)
^{196}Hg	0.15	3190	4.79
^{198}Hg	9.97	2	1.99
^{199}Hg	16.87	2150	363
^{201}Hg	13.18	5.7	0.75
^{199}Hg	6.87	0.43	0.30

The most intense gamma-ray emitted by ^{200}Hg following neutron capture has an energy of 368 keV, and other gamma-rays have much lower intensities (see Table 1.6). Since only a weak signal is expected in *in vivo* trace element measurement, only the most intense gamma-ray is considered in the analysis. A typical gamma-ray spectrum following thermal neutron capture is shown in Figure 1.5. It is similar to

Table 1.6: Prompt gamma-rays emitted by ^{200}Hg following thermal neutron capture (National Nuclear Data Center). Only those with relative intensities greater than 5% are listed. I_{max} refers to gamma-rays emitted per neutron capture, and has a value of 81.3% (Berkeley National Laboratory).

E (keV)	I/I_{max} (%)	E (keV)	I/I_{max} (%)
368	100.00	4739	8.9
661	6.86	4842	6.1
1263	5.5	5050	6.1
1570	7.8	5658	7.6
1693	13.9	5967	17.0
2002	6.5	6458	6.3

that of cadmium except for the fact that the mercury peak at 368 keV is located on the lower energy side of the 478 keV gamma-ray that results from ^{10}B. Boron is an integral part of the shielding (see Section 1.3.1), and cannot be eliminated from the spectrum. Unlike cadmium, detection of mercury is inhibited further by the presence of the Compton continuum from both the 478 keV and 2.223 MeV gamma-ray peaks. In addition, the nearby presence of the 352 keV gamma-ray from the thermal neutron capture of ^{56}Fe further complicates the spectrum.

The method of PGNAA of mercury is analogous to that of cadmium. The same experimental method was used and the only difference was in the data analysis. Details of data analysis spectrum fitting are described in Section 1.5.

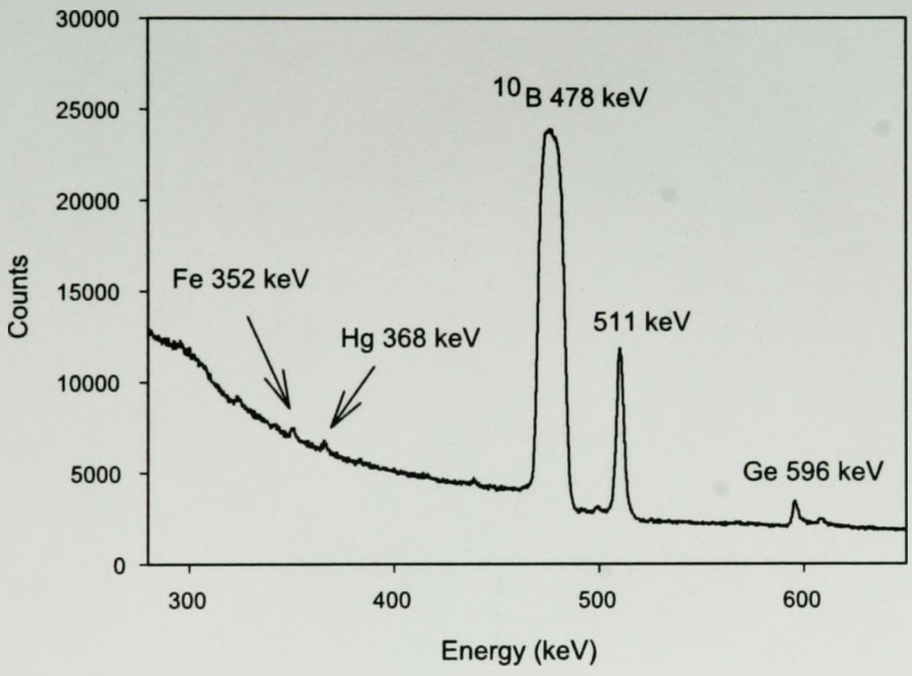

Figure 1.5: Neutron activation spectrum showing the Hg 368 keV gamma-ray, located on a steep background on the lower energy side of the 478 keV gamma-ray from ^{10}B. The 352 keV Fe peak is in close proximity to the 368 keV gamma-ray. This spectrum was collected with a 2500 ppm kidney phantom inside a water tank phantom for 2000 s live time.

1.4 X-ray fluorescence

There are four main possible interactions of photons with matter: photoelectric absorption, Compton scattering, pair production and coherent (Rayleigh) scattering. With the exception of pair production, each process is important in the detection of trace elements *in vivo*.

The photoelectric effect is based on the interaction of a photon with the electrons of atoms. The incident photon ejects an electron from an atomic shell (such as the K shell), and an ionized atom is created. The energy of the electron is given by

$$E_e = h\nu - E_b \tag{1.3}$$

where E_e is the photoelectron energy, $h\nu$ is the energy of the incident photon and E_b is the electron binding energy. The vacancy left by the ejected electron is filled by an electron from a higher shell, which gives rise to an x-ray whose discrete energy is the difference in shell energies. This is followed by a rearrangement of the atomic electrons and leads to the capture of a free electron from the medium to create a neutral atom. The basis of x-ray fluorescence is to detect the characteristic x-rays that accompany the photoelectric process. A schematic of x-ray fluorescence is shown in Figure 1.6. Alternatively, the excited atom can transfer its energy to an electron in an outer shell, after which this electron (called an Auger electron) is ejected. Auger electron emission is typical for low-Z elements, and for higher-Z elements x-ray fluorescence yields exceed 90%. For mercury, the K fluorescence yield is 96.6%.

The most energetic x-rays are generated by the filling of a K shell vacancy and are called K x-rays. Similarly, L x-rays are generated from filling a L shell vacancy, and M x-rays are generated from filling of a M-shell vacancy, but their energies are

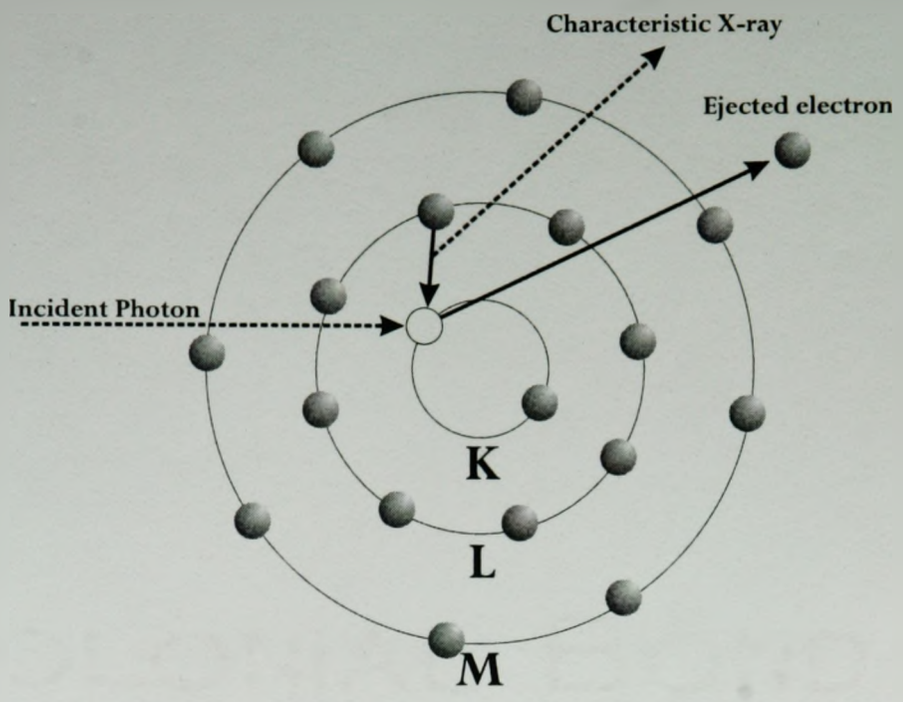

Figure 1.6: Schematic of x-ray fluorescence.

considerably lower than K x-rays. Since mercury is to be detected in the kidneys, the large thickness of overlying tissue would largely attenuate all but the K x-rays. The detection of mercury therefore takes place through K x-ray fluorescence and will be referred to as x-ray fluorescence or XRF for brevity. Mercury K x-rays and corresponding energies and intensities are listed in Table 1.7. A typical mercury XRF spectrum is shown in Figure 1.7.

The relatively high energies of mercury K x-rays allow for the detection in an organ such as the kidney. X-ray fluorescence of cadmium in the liver or kidney, on the other hand, is not an ideal method since the most energetic K x-ray is at 26 keV and therefore would be largely attenuated in several centimetres of tissue.

Compton scatter is another important process that results from the interaction of photons with matter. An incoming photon is not absorbed by the atom as with the photoelectric effect, but is instead scattered by an angle θ, transferring a portion of its energy to the recoil electron. The resultant energy of the scattered photons, on

Table 1.7: Mercury K x-rays and their intensities (Berkeley National Laboratory Atomic Data).

X-ray	Energy (keV)	Intensity (per 100 K-shell vacancies)	Shell transition
$K_{\alpha 1}$	70.818	46.3	L_3 - K
$K_{\alpha 2}$	68.894	27.5	L_2 - K
$K_{\beta 1,3}$	80.255/79.824	10.70/5.59	M_3/M_2 - K
$K_{\beta 2',2''}$	82.545/82.435	2.56/1.31	N_3/N_2 - K
$KO_{2,3}$	83.028	0.64	O_3/O_2 - K

the assumption that the electron involved is unbound and stationary, is

$$h\nu' = \frac{h\nu}{1 + \frac{h\nu}{m_0c^2}(1 - \cos\theta)} \tag{1.4}$$

where $h\nu$ is the energy of the incident photon, m_0c^2 is the rest mass of the electron, and θ is the scattering angle, which can vary from 0 to 180°. The probability of Compton scattering increases linearly with atomic number Z and therefore is a dominant feature in an XRF spectrum (see Figure 1.7).

Pair production commonly takes place if the energy of a photon is greater than 1022 keV, or two times the electron rest mass, m_0c^2. The photon in this case has sufficient energy to create an electron-positron pair. The positron subsequently annihilates and creates two annihilation photons. Since the energies of photons used in XRF are much lower than 1022 keV, this process does not occur in mercury XRF.

Coherent or Rayleigh scatter is most probable for photons with energies less than several hundred keV and for high Z materials. A photon scatters coherently from the atom in the medium without losing energy. The differential cross-section for

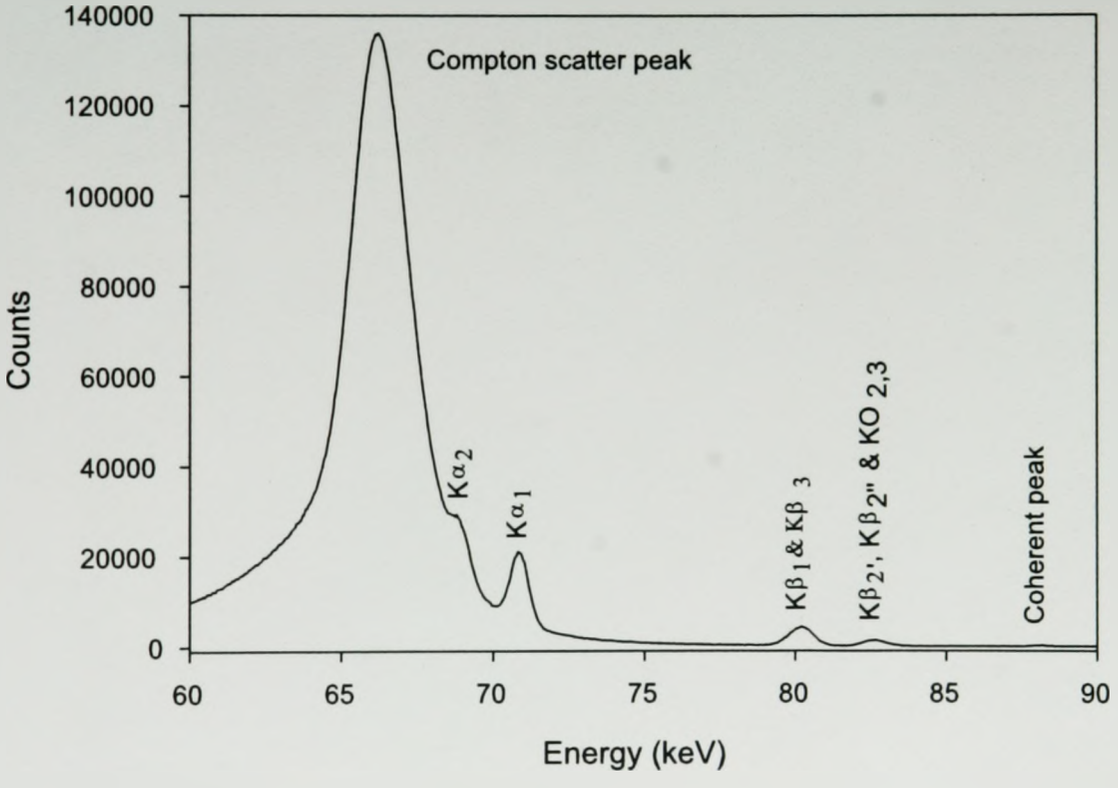

Figure 1.7: X-ray fluorescence spectrum of mercury with ^{109}Cd source (with phantom containing 2500 ppm of mercury). The coherent photopeak at 88 keV is not clearly visible on the scale used.

coherent scattering is given by

$$\frac{d\sigma}{d\Omega} = \frac{1}{2}r^2\left(1+\cos^2\theta\right)|F(q)|^2 \tag{1.5}$$

where r is the classical radius of the electron, θ is the scatter angle, and F(q) is the atomic form factor, which is dependent on the atomic number of the scatterer, energy of the photon and scattering angle. At very small angles, the coherent scatter probability varies as Z^2, while at angles close to 180° the probability becomes Z^5 or Z^6 for 88 keV. Since the detection geometry of mercury XRF is approximately 180° (discussed in detail in Chapter 4), the coherent scatter gamma-ray is present in an XRF spectrum (Figure 1.7) despite the presence of primarily low Z tissue-equivalent materials. The coherent scatter peak can be used to normalize x-ray signals from trace elements, such as lead, in bone (Somervaille *et al.*, 1985).

1.4.1 X-ray fluorescence photon source

The K absorption edge of mercury is at 83.1 keV and therefore ideally one requires the external photon energy to be just above the absorption edge in order to excite the atom in question (see Figure 1.8). There are two main types of photon sources for XRF of mercury: radioisotope gamma-rays or x-rays from an x-ray tube. Both methods have been attempted in the past (see Section 1.2.3). Polarized XRF has been used extensively, however the detection limit remains high. Since only one study attempted to detect mercury with source-excited XRF (with ^{57}Co, Smith *et al.*, 1982), the feasibility of using source-excited XRF to detect mercury was explored in this thesis.

There are two main considerations when choosing a source: (1) its energy must be above and as close as possible to the 83.1 keV absorption edge of mercury

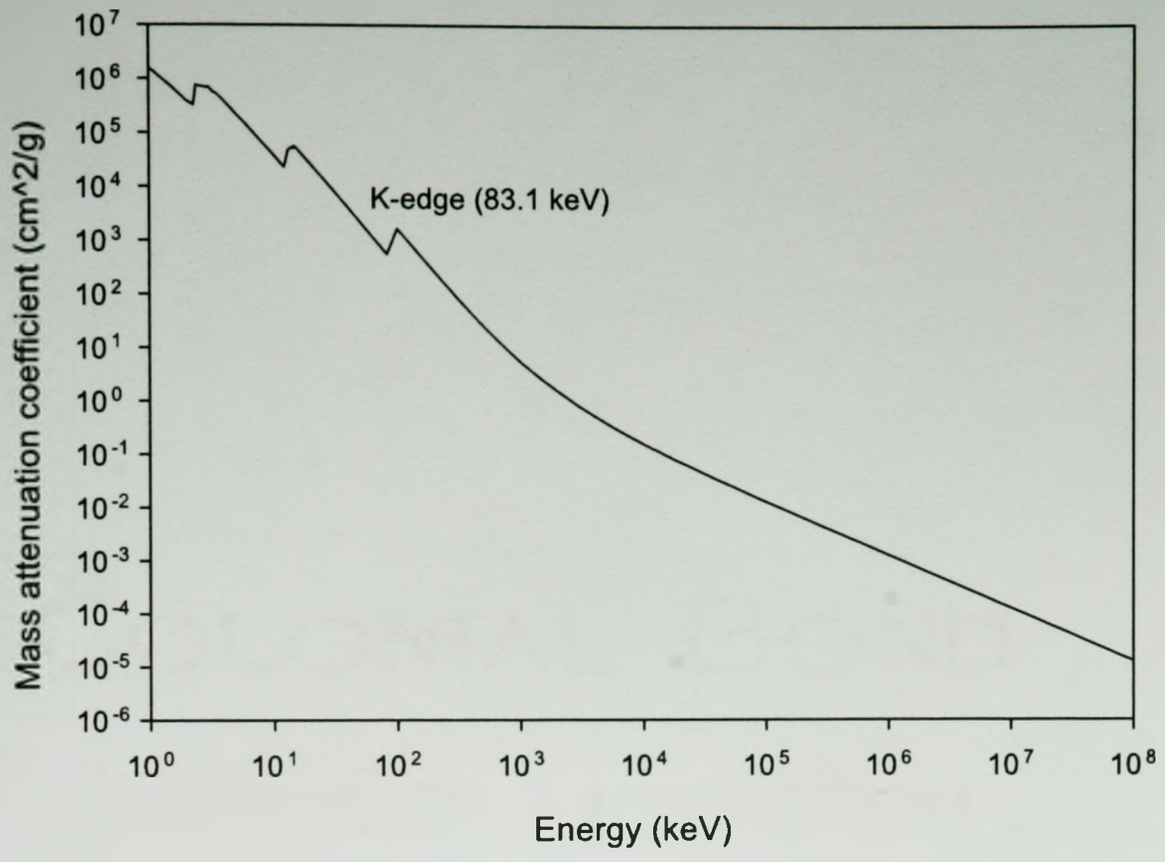

Figure 1.8: Photoelectric cross-section of mercury, with the K-edge at 83.1 keV (XCOM).

and (2) the interference of the Compton peak with mercury x-rays should be kept to a minimum. There are several sources that can be used to excite mercury atoms in the kidney. Table 1.8 lists possible sources along with the energy of the Compton peak at 90° and 180° detection geometry. The best choice for excitation of mercury atoms is ^{109}Cd in the 180° detection geometry since its energy is the closest to the absorption edge and the energy of the 180° Compton-scattered gamma-ray is below the K_α x-rays (see Table 1.7). Although the energies of ^{153}Gd gamma-rays are still relatively close to the absorption edge, the Compton scatter energies are interfering with both the K_α and K_β x-rays in either 90° and 180° detection geometry. The Compton-scattered gamma-rays of ^{57}Co are well-away from mercury x-rays, however

previous attempts at using ^{57}Co (Smith *et al.*, 1982) yielded a relatively high detection limit. This was partly due to the fact that the gamma-ray energies were well above the absorption edge. The same is true for ^{144}Ce and ^{141}Ce. Therefore, ^{109}Cd was chosen for source-excited XRF of mercury.

Table 1.8: Possible gamma-ray sources for XRF of mercury.

Source	Half-life (d)	E_γ (keV)	E_γ', 90° scatter (keV)	E_γ', 180° scatter (keV)
^{109}Cd	462.4	88.0	75.1	65.5
^{153}Gd	240.4	97.4 103.2	81.8 85.9	70.5 73.5
^{57}Co	271.8	121.9 136.3	98.4 107.6	82.5 88.9
^{144}Ce	284.9	133.5	105.8	87.7
^{141}Ce	32.5	145.4	113.2	92.7

Cadmium-109 decays via electron capture (EC) to the first excited state of ^{109}Ag with a half-life of 462.4 days. ^{109}Ag decays to the ground state by internal conversion (IC) with a 96.3% probability and by 88.0 keV gamma-ray emission with a 3.7% probability. The decay scheme of ^{109}Cd is shown in Figure 1.9. Internal conversion also causes the emission of characteristic Ag K x-rays with energies of 22 and 25 keV. These photons are too low in energy to excite mercury atoms, hence they only contribute to patient dose and create additional signal that has to be processed by detection electronics. In order to reduce the emission of Ag x-rays, a 0.7 mm copper attenuator was placed in front of the source collimator (see Chapter 4, Figure 2). This

copper filter virtually eliminates Ag x-rays, making ^{109}Cd a monoenergetic 88 keV gamma-ray source. A backscatter (approximately 180°) geometry was used, hence the energy of the Compton peak is at approximately 66 keV.

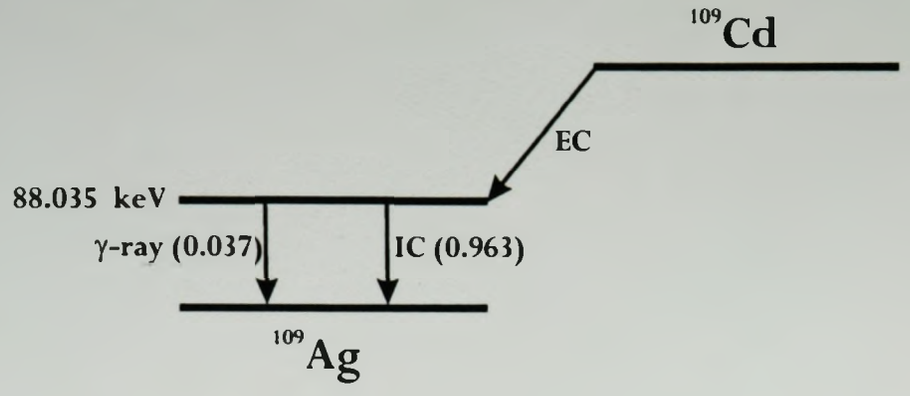

Figure 1.9: Decay scheme of ^{109}Cd (Table of Nuclides).

1.5 Spectrum analysis

In order to obtain quantitative information from a photon spectrum to perform an *in vivo* cadmium or mercury measurement, it is necessary to extract the number of counts in a given gamma-ray or x-ray peak. Therefore, a flexible and reliable method is needed to estimate the photon peak area and the associated uncertainty. Many commercially available spectral fitting programs exist and are most likely adequate in many applications for linear fit functions comprised of normally distributed data. However, in the case of spectrum analysis, data follows Poisson statistics and the need for a non-linear fitting algorithm arises in order to fit individual photopeaks. The main task of a fitting program for spectrum analysis is to fit a user-defined function to the data, determine best-fit parameters for that function, determine the uncertainty in the best-fit parameters, and calculate a goodness of fit parameter such as the χ^2 statistic. The χ^2 statistic is the basis of least-squares fitting methods and can be

written as (Bevington, 1969)

$$\chi^2 = \sum_{i=1}^{N} \frac{(y_i - y_{fit})^2}{\sigma_i^2}, \tag{1.6}$$

where y_i are the individual data points, N is the number of data points, σ_i^2 are the variances and y_{fit} is value of the fit function in the i^{th} bin and is comprised of n fit parameters. The minimization of the χ^2 surface in n parameter space is the basis of the least squares fitting method.

1.5.1 Levenberg-Marquardt fitting method

The Levenberg-Marquardt algorithm is a non-linear least-squares fitting routine that minimizes the χ^2 using a smooth interpolation between two search methods: (1) the gradient search method and (2) the curvature method (Marquardt, 1963, Bevington, 1969, Press *et al.*, 1992). The gradient search method of least squares is based on the incrementation of all fit parameters simultaneously and calculation of a gradient of χ^2 for a given set of fit parameters. This method follows the "direction of steepest descent" toward a global minimum. As it approaches the minimum, the gradient of χ^2 and thus increment steps on fit parameters tend to zero, making it difficult to approach the true minimum and increasing computation time. Thus, the gradient search method works best when far from the minimum.

When the gradient search method step size is less than a defined threshold level in the fitting program, the Levenberg-Marquardt method switches to the curvature method, which is based on the direct calculation of the χ^2 surface curvature by taking the second derivative of χ^2. The first increment step in the curvature method jumps close to the minimum when the curvature of the χ^2 surface is calculated. The next couple of iterations get closer to the minimum and the calculation is terminated

when it is not statistically significant to continue the calculation, namely when the increment step in the fit parameter is significantly less than the error on that parameter. The curvature method is most useful when close to the true minimum. Since the Levenberg-Marquardt method allows for convergence after only a small number of iterations by switching between the gradient search and curvature methods, it is the adopted method for fitting of spectral data and of multiple data sets. A detailed description of the Levenberg-Marquardt method can be found in basic statistical and data analysis textbooks (Bevington, 1969, Press *et al.*, 1992).

For counting experiments, the definition of χ^2 in Equation 1.6 is not valid since the variance on the individual data points σ_i becomes the square root of the number of counts per bin. If there are no counts in a particular bin the χ^2 is not defined. In order to avoid this, the fit function itself, y_{fit}, can be used to estimate the variance and the definition of χ^2 becomes (Bevington, 1969)

$$\chi^2 = \sum_{i=1}^{N} \frac{(y_i - y_{fit})^2}{y_{fit}}. \tag{1.7}$$

This definition was used for the χ^2 minimization in the Levenberg-Marquardt algorithm in this thesis. The basic recipe for the algorithm was taken from Press *et al.*, 1992. The complete program was originally written to fit exponential decay curves (G. Grinyer, 2004), and has been modified to fit spectral peaks. The computation of best-fit parameters begins with a user-defined fit function and a set of guess parameters. The program allows for the reading in of one or more data sets and defining the region of the spectrum to fit. The output of the program is a set of best-fit parameters with uncertainties, and the reduced χ^2 (Equation 1.7 divided by the degrees of freedom, $(N-n)$). In addition, the program outputs the photopeak area with uncertainty. As the peak area tends to zero, the location of the peak wanders away from the expected peak position. Therefore the peak position is randomly constrained to within 0.25 σ

to 0.5 σ of the location of the peak, which is deduced from the fitting of higher concentration spectra. The peak position was not fixed due to possible detector gain shifts in the course of the experiment.

The choice of an appropriate fit function to describe the photon peak and background is one of the most important considerations, and is crucial in obtaining an unbiased estimate of the peak area and subsequent concentration. If the fit function does not accurately describe the data, the program may not converge or convergence may result in an improper value being deduced for the peak area. Thus, the fit function was tailored to each set of photopeaks resulting from PGNAA of cadmium and mercury, and XRF of mercury. The following sections describe the fitting procedures and fit functions used for the analysis of both PGNAA and XRF spectra.

1.5.2 Analysis of cadmium PGNAA spectra

The fit function to be used to fit a gamma-ray photopeak should be physically reasonable in order to describe the shape of the peak and background. An important constraint when choosing a fit function is the number of free parameters the program has to calculate since a large number of free parameters may cause the algorithm to fall into local minima and not converge on the best-fit parameters. It can also lead to large (or infinite) covariances between fitted parameters. Although almost any physical feature can be incorporated into the fit function, a high parameter number fit that describes every possible physical process contributes little to the overall fit and in fact hinders it by not allowing for convergence on best-fit parameters.

The fit function consists of the gamma-ray peak of interest, the background underneath and in the vicinity of the peak, and any other spectral features in the

vicinity of the peak, if required. In order to describe the cadmium 559 keV gamma-ray peak, a Gaussian function is adequate to include two basic features of a detected gamma-ray: a delta function at 559 keV and its broadening which depends on the resolution of the detector. A gamma-ray peak can be modeled by a Gaussian if the count rate is low, the background is low, the electronics are stable and their settings optimized, and the detector is not damaged. If this is not the case then the gamma-ray peak becomes skewed and a modified function is needed (see Equation 1.11 below). For cadmium PGNAA in this work, there was no need to include any other peaks (for example 575 keV peak from Ge) as they are sufficiently far away from the 559 keV peak. The background underneath the 559 keV cadmium peak was approximated by a linear function. The following five parameter fit function y_{fit} was used to fit cadmium spectra in PGNAA analysis:

$$y_{fit} = a_3 + a_1 x + a_2 \exp\left[-\frac{1}{2}\left(\frac{\mathrm{x} - \mathrm{a}_4}{\mathrm{a}_5}\right)^2\right]. \tag{1.8}$$

The fit parameters are designated as a_1: slope of the linear background, a_2: amplitude of the Cd 559 keV peak, a_3: constant of straight line background, a_4: position of the Cd 559 keV peak, and a_5: width of the Cd 559 keV peak. Here, the "width" parameter refers to the standard deviation (σ) and not the full-width at half-maximum (FWHM) of the peak. Of these parameters, the width (a_5) is fixed at a value determined by fitting a cadmium spectrum of a high concentration phantom. The area of the peak, A is calculated from

$$A = \sqrt{2\pi} \times \text{Amplitude} \times \text{Width} = \sqrt{2\pi}\mathrm{a}_2\mathrm{a}_5. \tag{1.9}$$

Upon fitting spectra for a set of phantoms with varying concentrations (0 to 121 mg for kidney phantoms and 0 to 160 ppm for liver phantoms) and calculating the peak area for each concentration using Equation 1.9, a calibration line (peak area

as a function of cadmium concentration or weight) was plotted. A weighted linear fit is used to extract the slope (or sensitivity) and intercept, which are used to calculate the minimum detection limit (MDL) and, in the case of an *in vivo* measurement, the concentration or weight of cadmium present in the organ. The MDL is defined as twice the uncertainty in the 0 ppm or 0 mg phantom, σ_0, divided by the slope of the calibration line, S:

$$MDL = 2 \times \left(\frac{\sigma_0}{S}\right). \tag{1.10}$$

The function in Equation 1.8 is sufficient for fitting spectra, however as the detector becomes neutron-damaged the peaks become skewed with the lower energy side being wider than the upper energy side. In order to describe this phenomenon, a second fit function with two different width parameters was used:

$$y_{fit} = \begin{cases} a_3 + a_1 x + a_2 \exp\left[-\frac{1}{2}\left(\frac{x-a_4}{a_5}\right)^2\right] & x \leq a_4 \\ a_3 + a_1 x + a_2 \exp\left[-\frac{1}{2}\left(\frac{x-a_4}{a_6}\right)^2\right] & x > a_4. \end{cases} \tag{1.11}$$

where the parameters are those described above with a_5 and a_6 corresponding to the cadmium 559 keV peak widths on the lower and upper energy side, respectively. Both widths were determined from a separate spectrum and fixed at this value for calibration fitting to determine the peak area as described above. Figure 2 of Chapter 2 shows an example of a fit to the 559 keV gamma-ray in a cadmium PGNAA spectrum.

1.5.3 Analysis of mercury PGNAA spectra

Fitting of mercury spectra follows the same procedure as for cadmium. However, several modifications were made to the function in Equation 1.8. First, the 368 keV mercury peak is located on a steeper Compton background (see Figure 1.5) and

therefore an exponential background was used instead of a linear background. Second, the presence of a prompt gamma-ray at 352 keV from the ^{56}Fe(n,γ)^{57}Fe reaction made it necessary to fit both peaks simultaneously to obtain an overall good fit in the region. Therefore, the function used to fit the mercury spectra was:

$$y_{fit} = a_1 \exp\left[a_2 x\right] + a_3 \exp\left[-\frac{1}{2}\left(\frac{x - a_4}{a_5}\right)^2\right] + a_6 \exp\left[-\frac{1}{2}\left(\frac{x - a_4 + b}{a_7}\right)^2\right], \quad (1.12)$$

where b is the number of channels between the 368 and 352 keV peaks. The seven parameters in the above function are a_1: constant of the exponential background, a_2: rate of change of the exponential background, a_3: amplitude of the Hg 368 keV peak, a_4: position of the Hg 368 keV peak, a_5: width of the Hg 368 keV peak, a_6: amplitude of the Fe 352 keV peak, and a_7: width of the Fe 352 keV peak. Figure 1.10 shows an example of a mercury spectrum and resulting fit.

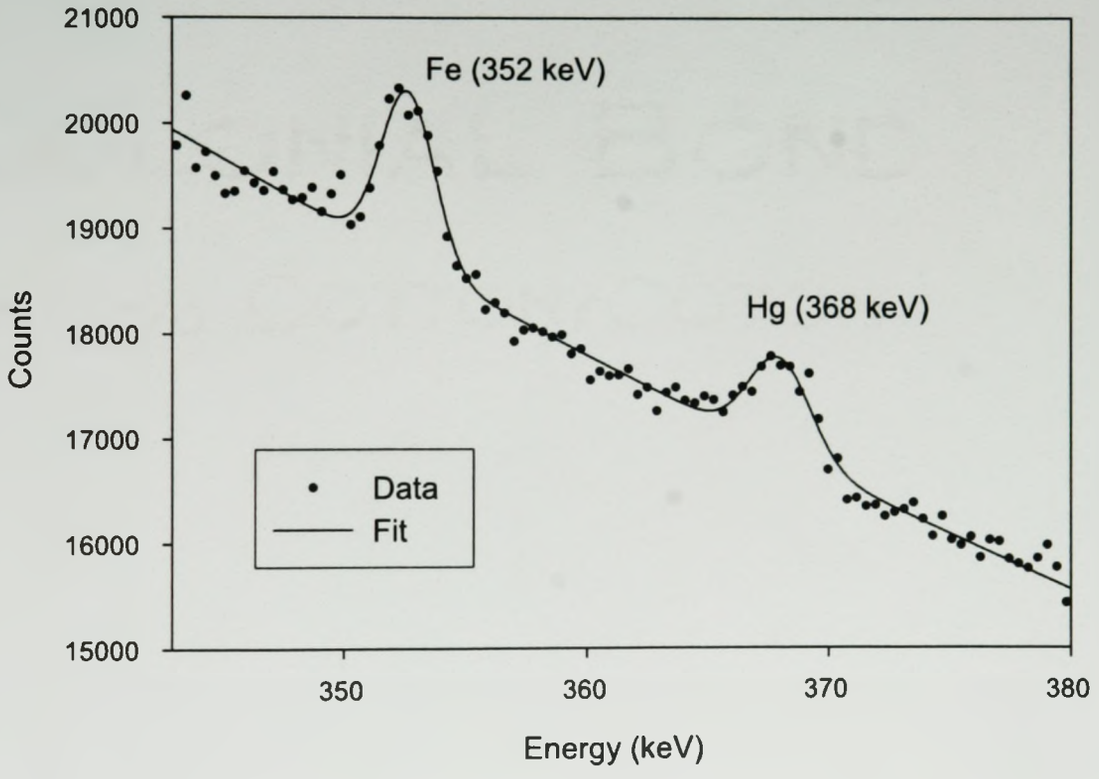

Figure 1.10: An example of a Hg spectrum showing the 368 keV gamma-ray and resulting fit for a 125 mL kidney phantom containing 2500 ppm of Hg. Due to the proximity of the Fe 352 keV peak, both peaks were included in the fit.

1.5.4 Analysis of chlorine PGNAA spectra

An analysis of chlorine spectra was necessary for the comparison study in Chapter 3. Several chlorine photopeaks from the $^{35}Cl(n,\gamma)^{36}Cl$ reaction were analyzed: 517, 1164, 1951, 1959 and 6110 keV. At the time of the experiment, the detectors were neutron damaged therefore a two-width function (see Equation 1.11) was used to fit all chlorine peaks. In addition, the 517 keV peak is in close proximity to the 511 keV annihilation peak so the function had to include both peaks (analogous to mercury, see Equation 1.12). Similarly, the 1951 and 1959 keV had to be analyzed together. An example of a fit to chlorine spectra is shown in Figure 2 of Chapter 3.

1.5.5 Analysis of mercury XRF spectra

The analysis of mercury XRF spectra is more complex than that of the PGNAA spectra due to the presence of many x-ray peaks that overlap and that are located on a complex background. There were seven K x-rays of mercury (see Table 1.7) that were analyzed, in addition to the coherent peak at 88 keV. The $K_{\alpha 1}$ x-ray at 70.818 keV and the $K_{\alpha 2}$ x-ray at 68.894 keV were well resolved in the spectrum, however their fitting is complicated by their location and proximity to the large Compton peak at 66 keV. In addition, the $K_{\alpha 2}$ peak was barely visible in the presence of the torso phantom (water tank), therefore both peaks along with the upper energy side of the Compton peak had to be fit together. The background under the K_{α} x-rays was best described as a double exponential function. The relative amplitude of $K_{\alpha 1}$ to $K_{\alpha 2}$ was fixed at a value known from literature (see Table 1.7), and distances between peaks were determined from the energy calibration. The nine-parameter, three-peak

function used to fit the K_α peaks was

$$\begin{aligned} y_{fit} &= a_3 \exp\left[a_1 x\right] + a_5 \exp\left[a_6 x\right] + a_2 \exp\left[-\frac{1}{2}\left(\frac{x - a_7}{a_8}\right)^2\right] \\ &+ \frac{a_2}{AMP} \exp\left[-\frac{1}{2}\left(\frac{x - a_7 + b_1}{a_8}\right)^2\right] \\ &+ a_4 \exp\left[-\frac{1}{2}\left(\frac{x - a_7 + b_2}{a_9}\right)^2\right]. \end{aligned} \tag{1.13}$$

The nine parameters in Equation 1.13 are a_1: rate of change of the exponential background 1, a_2: amplitude of the $K_{\alpha 1}$ peak, a_3: constant of the exponential background 1, a_4: amplitude of the Compton peak, a_5: constant of the exponential background 2, a_6: rate of change of exponential background 2, a_7: position of the $K_{\alpha 1}$ peak, a_8: width of the K_α peaks, a_9: width of the Compton peak, and b_1 is the number of channels between the $K_{\alpha 1}$ and $K_{\alpha 2}$ peaks, b_2 is the number of channels between the $K_{\alpha 1}$ and Compton peaks, and AMP is the relative amplitude of the $K_{\alpha 1}$ to $K_{\alpha 2}$ and has a value of 1.68 (see Table 1.7). The widths of the K_α and Compton peaks were fixed at a predetermined value. The widths of the Hg K x-rays were deduced from fitting of the 88 keV coherent peak and its best-fit width parameter. An example of the fit in the $K_{\alpha 1}$ region in shown in Figure 1.11.

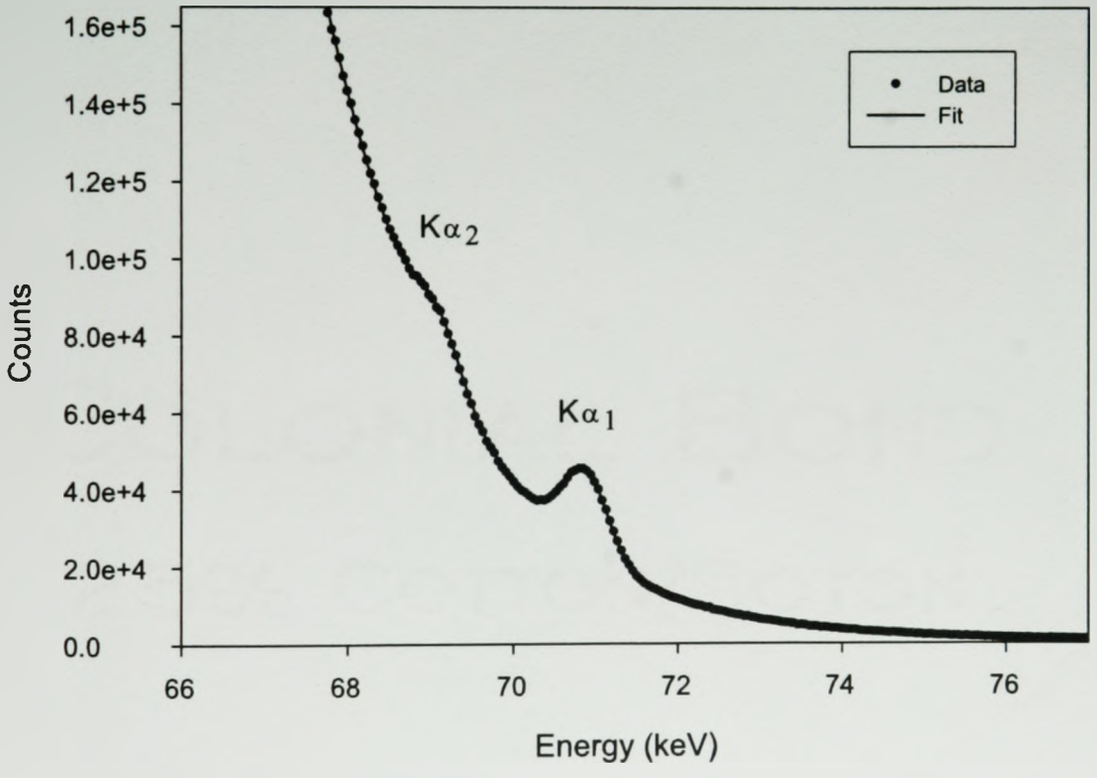

Figure 1.11: An example of a fit to data in the K_α region collected with a 2500 ppm kidney phantom at 1 cm depth in the torso phantom.

The $K_{\beta 1}$ x-ray at 80.255 keV and the $K_{\beta 3}$ x-ray at 79.824 keV are close in energy and therefore are not resolved in the photon spectrum, appearing as a single photopeak. As a result, these were fit with their relative amplitudes fixed. These K_β x-rays are sufficiently far away from the Compton peak that the background was described as a single exponential. The fit function that describes the $K_{\beta 1}$ and $K_{\beta 3}$ peaks is

$$\begin{aligned} y_{fit} &= a_3 \exp\left[a_1 x\right] + a_2 \exp\left[-\frac{1}{2}\left(\frac{x - a_4}{a_5}\right)^2\right] \\ &+ \frac{a_2}{AMP} \exp\left[-\frac{1}{2}\left(\frac{x - a_4 + b}{a_5}\right)^2\right] \end{aligned} \tag{1.14}$$

The parameters in the above equation are a_1: rate of change of the exponential background, a_2: amplitude of the $K_{\beta 1}$ peak, a_3: constant of exponential background, a_4: position of the $K_{\beta 1}$ peak, a_5: width of the K_β peaks, b is the number of channels between the K_β peaks, and AMP is the relative amplitude of $K_{\beta 1}$ to $K_{\beta 3}$ and has a value of 1.91. An example of a fit to $K_{\beta 1}$ and $K_{\beta 3}$ peaks is in Chapter 4, Figure 4.

The $K_{\beta 2'}$ (82.545 keV), $K_{\beta 2''}$ (82.435 keV) and $KO_{2,3}$ (83.028 keV) are also in close proximity to each other and were fit together. The five-parameter, three-peak function that describes them is

$$\begin{aligned} y_{fit} &= a_3 \exp\left[a_1 x\right] + a_2 \exp\left[-\frac{1}{2}\left(\frac{x - a_4}{a_6}\right)^2\right] + \frac{a_2}{AMP_1} \exp\left[-\frac{1}{2}\left(\frac{x - a_4 + b_1}{a_6}\right)^2\right] \\ &+ \frac{a_2}{AMP_2} \exp\left[-\frac{1}{2}\left(\frac{x - a_4 - b_2}{a_6}\right)^2\right] \end{aligned} \tag{1.15}$$

The five parameters in Equation 1.15 are a_1: rate of change of the exponential background, a_2: amplitude of the $K_{\beta 2'}$ peak, a_3: constant of the exponential background, a_4: position of the $K_{\beta 2'}$ peak, a_5: width of the K_β and $KO_{2,3}$ peaks, b_1 is the number of channels between the $K_{\beta 2'}$ and $K_{\beta 2''}$ peaks, b_2 is the number of channels between the $K_{\beta 2'}$ and $KO_{2,3}$ peaks, AMP_1 is the relative amplitude of $K_{\beta 2'}$ to $K_{\beta 2''}$

with a value of 1.95, and AMP_2 is the relative amplitude of $K_{\beta 2'}$ to $KO_{2,3}$ with a value of 4.00.

The coherent gamma-ray at 88 keV was fit as a single peak on an exponential background:

$$y_{fit} = a_3 \exp\left[a_1 x\right] + a_2 \exp\left[-\frac{1}{2}\left(\frac{x - a_4}{a_5}\right)^2\right]. \tag{1.16}$$

The five parameters in the above equation are a_1: rate of change of the exponential background, a_2: amplitude of the coherent peak, a_3: constant of the exponential background, a_4: position of the coherent peak, and a_5: width of the coherent peak.

The main purpose of fitting the coherent gamma-ray peak was to determine its width in order to fix the widths of Hg K x-rays at this value. Since energies of K x-rays were sufficiently close to 88 keV, the widths were assumed to be the same as the coherent peak.

Upon fitting each set of peaks separately to obtain the peak area as a function of mercury concentration, a calibration line was plotted and a weighted linear fit was used to calculate the slope and MDL using Equation 1.10. The individual MDLs were combined using Equation 2 in Chapter 4 to obtain the final MDL.

1.6 Thesis preface

Chapter 1 gives an introduction to the occupational exposure-related health effects and existing monitoring methods of cadmium and mercury. It also includes the description of the two methods that are the subject of this thesis: prompt gamma neutron activation analysis and x-ray fluorescence. In addition, Chapter 1 contains details of data analysis and spectrum fitting.

Chapter 2 describes the detection of cadmium in the liver and kidney using prompt gamma neutron activation analysis. As a result of optimization of the *in vivo* cadmium detection system, the minimum detection limit in the liver and kidneys is low enough to allow for monitoring of occupationally exposed individuals.

Chapter 3 is a comparison study of the relative detectability of mercury, cadmium and chlorine in order to explain the relatively low mercury sensitivity of the PGNAA detection system. When the three elements were compared, cadmium had a higher than expected sensitivity, mostly due to its non-$1/\nu$ thermal neutron cross-section dependence. The detection limit of mercury using PGNAA was too high to be applicable to *in vivo* measurements.

Chapter 4 describes the development of an x-ray fluorescence system for the detection of kidney mercury *in vivo*. This source-based system, which includes a planar hyperpure germanium detector, succeeded in lowering the minimum detection limit for both a bare kidney phantom and kidney phantom in a torso phantom. The results achieved with the planar detection system were comparable to previous polarized x-ray fluorescence results, but for a lower dose to the subject.

Chapter 5 includes results obtained with a cloverleaf detection system for source-based mercury x-ray fluorescence. Experiments with bare kidney phantoms yielded promising results, however torso phantom experiments yielded a detection limit comparable to those obtained with the planar detection system. *In vivo* measurements performed on two patients with the cloverleaf system are also described in detail.

The final chapter, Chapter 6, is a discussion of thesis conclusions and of possible future research directions for the improvement of cadmium and mercury detection methods.

Chapter 2

In Vivo Prompt Gamma Neutron Activation of Cadmium in the Kidney and Liver (Article I)

2.1 Introduction to Article I

The work presented in the following Article deals with the detection of cadmium using prompt gamma neutron activation analysis with the ^{238}Pu-Be neutron source. The main emphasis of this research was to improve the measurement sensitivity in the kidneys and liver in order for this method to be applicable for *in vivo* monitoring of cadmium exposure of occupationally exposed individuals. The lowering of the minimum detection limit (MDL) was accomplished by optimizing the source and collimator arrangement, exploring several detector configurations and positioning, improving the liver phantom sizing to resemble the human liver more closely, and developing a robust cadmium peak fitting procedure. The performance of the

McMaster cadmium system was compared to other systems using the figure of merit, F, a detector-independent parameter that includes the MDL, dose and detector performance parameters.

The research presented in Article I was undertaken primarily by the author of this thesis, with initial help from Dr. Soo-Hyun Byun in phantom making and experimental set-up, and under the guidance of Dr. David Chettle. The Levenberg-Marquardt algorithm (Press *et al.*, 1992, Bevington, 1969) was used to fit spectral peaks. The original computer code used to fit exponential decay curves (G. Grinyer, 2004) was modified by the author of this thesis from its original form to fit photopeaks, and in particular the cadmium 559 keV gamma-ray peak. The modifications are described in detail in Section 1.5.1. The article manuscript was written by the author of this thesis.

2.2 Contents of Article I

Available online at www.sciencedirect.com
SCIENCE DIRECT
Applied Radiation and Isotopes 63 (2005) 475–479
Applied Radiation and Isotopes
www.elsevier.com/locate/apradiso

In vivo prompt gamma neutron activation analysis of cadmium in the kidney and liver

J. Grinyer*, S.H. Byun, D.R. Chettle

Medical Physics and Applied Radiation Sciences Unit, McMaster University, Hamilton, Ont., Canada L8S 1H2

Received 20 December 2004; received in revised form 28 March 2005; accepted 24 May 2005

Abstract

An existing McMaster University in vivo prompt gamma neutron activation analysis system has been improved in order to reduce the cadmium detection limit in the kidney and liver. The detection limit for the kidney was found to be 1.7 mg, a greater than factor of 2 improvement over the previous results obtained at McMaster. The liver detection limit was determined to be 3.3 ppm. The corresponding skin dose for these measurements was only 0.5 mSv. The effect of kidney position on the detection limit also was examined. Figures of merit were calculated in order to compare the performance of the current system to others.

Keywords: In vivo neutron activation analysis; Cadmium; Detection limit; Kidney; Liver

1. Introduction

Cadmium is a toxic heavy metal found in a variety of industrial and environmental settings. It is commonly encountered in mining, smelting and other important industrial processes during which workers may become occupationally exposed through inhalation of cadmium oxide dust and fumes. There are relatively small environmental contributions to cadmium body burdens from water and food intake, and cigarette smoking. Cadmium accumulates in the liver and kidneys, but it is the latter organ's function that may become impaired due to high levels of this metal. Occupationally exposed individuals are at highest risk for cadmium-related diseases such as kidney dysfunction, emphysema, osteomalacia and osteoporosis due to chronic exposures (Friberg et al., 1974). In order to prevent these, it is essential to monitor cadmium levels in the liver and kidneys.

There are several ways of assessing cadmium exposure. The first is to monitor urine and blood samples of workers; however, these indicate recent exposure only and do not directly reflect accumulated body burdens. Another method is to use in vivo prompt gamma neutron activation analysis, a non-invasive technique that measures the total cadmium content in the liver and kidneys. This method has been successfully used for many years (Franklin et al., 1990) and recent work has improved this technique further (McNeill and Chettle, 1998). In addition to neutron activation, polarized X-ray fluorescence has been used in vivo to detect cadmium in the kidney (Christoffersson and Mattsson, 1983). The feasibility of measuring cadmium in bone using X-ray fluorescence is also currently being investigated at McMaster.

In vivo prompt gamma neutron activation analysis is based on the thermal neutron capture of a stable isotope of cadmium, ^{113}Cd. The thermal neutron cross-section

*Corresponding author. Tel.: +1 905 5259 140x26328; fax: +1 905 522 5982.
E-mail address: grinyej@mcmaster.ca (J. Grinyer).

0969-8043/$ - see front matter © 2005 Elsevier Ltd. All rights reserved.
doi:10.1016/j.apradiso.2005.05.046

for the $^{113}Cd(n,\gamma)^{114}Cd$ reaction is 20,600 b. The natural abundance of ^{113}Cd is 12.3%, thus the effective elemental cross-section is about 2500 b, which is sufficiently large for in vivo studies. A subject is irradiated with neutrons and prompt gamma rays emitted following neutron capture are measured. The most prominent cadmium prompt gamma ray has an energy of 559 keV, which corresponds to the first excited to ground-state transition of ^{114}Cd. Liver or kidney cadmium content is determined through the measurement of the 559 keV gamma-ray intensity.

The purpose of this work was to improve an existing in vivo prompt gamma neutron activation analysis system in order to reduce the detection limit of cadmium, such that this technique can be used for better occupational exposure assessment and for certain cases of environmental exposure.

2. Methods

The prompt gamma neutron activation system involves two ^{238}Pu–Be sources with 17.4 Ci of total activity within a shielding and collimation apparatus that has been previously described (Fedorowicz et al., 1993). The basic structure of the apparatus has not been altered. It consists of the two neutron sources and a beryllium premoderator that softens the high energy neutron spectrum and acts as a neutron multiplier via the $^{9}Be(n,2n)^{8}Be$ reaction. Neutrons are shielded by tubes of steel and graphite, and collimated by alternating layers of polyethylene and steel. Blocks of lead, tungsten and bismuth shield detectors during measurement. The entire arrangement is encased by borated resin plates. A polyethylene tank filled with water approximating the torso is placed at the exit of the collimator. Phantoms with known amounts of cadmium in water simulating the kidney and liver can be placed inside the water tank at specific locations and irradiated.

Previously, two large surface area (51 mm diameter × 21 mm length) planar HPGe detectors were used (McNeill and Chettle, 1998). These were arranged such that one detector was below the other and connected to the same dewar, and thus both detectors were inevitably located at off-axis positions with respect to the phantom. In this work, the planar detectors were replaced by a large volume coaxial HPGe detector (58 mm diameter × 57 mm length, 35% efficiency relative to a 3 in × 3 in NaI detector at 1.33 MeV, 2.0 keV resolution at 1.33 MeV) and a smaller coaxial HPGe detector (51 mm diameter × 21 mm length, 10% efficiency relative to a 3 in × 3 in NaI detector at 1.33 MeV, 2.2 keV resolution at 1.33 MeV). These detectors were placed side by side at approximately a 90° angle, such that the more efficient coaxial detector was on the same axis as the phantom. A schematic of the apparatus used is shown in Fig. 1.

Another modification to the system has been to determine the optimal positions of the various components in order to maximize the cadmium count rate while at the same time maintaining detector dead time at a tolerable level. The neutron source-to-detector distance was varied in 3 cm steps, and cadmium sensitivity and detection limit were determined at each position. The source was then placed at the optimal location. The water tank was shifted such that the detector–beam distance was minimized. Finally, phantoms were placed at the water tank boundary, along the large coaxial detector axis. This geometry is consistent with the location of the liver in the body, but kidney location varies widely from person to person. Kidney phantoms were measured at several dorsal and lateral depths in the water tank in order to determine the kidney position dependence on cadmium measurement sensitivity.

Once these modifications were made, detection limits were measured. The kidney was represented by a 125 g polyethylene phantom and the liver was represented by both 1 and 2 L polyethylene phantoms. For a standard man, kidney mass is 155 g and liver mass is 1800 g, while for the standard woman kidney mass is 138 g and liver mass is 1400 g (ICRP 89, 2003). Kidney phantoms contained aqueous solutions ranging from 0 to 121 mg of cadmium. Solutions of 0–160 ppm of cadmium were used in the liver phantoms. Cadmium spectra were collected for 2000 s live time by submerging each phantom at prescribed depths in the water tank. Phantom calibrations were performed by obtaining

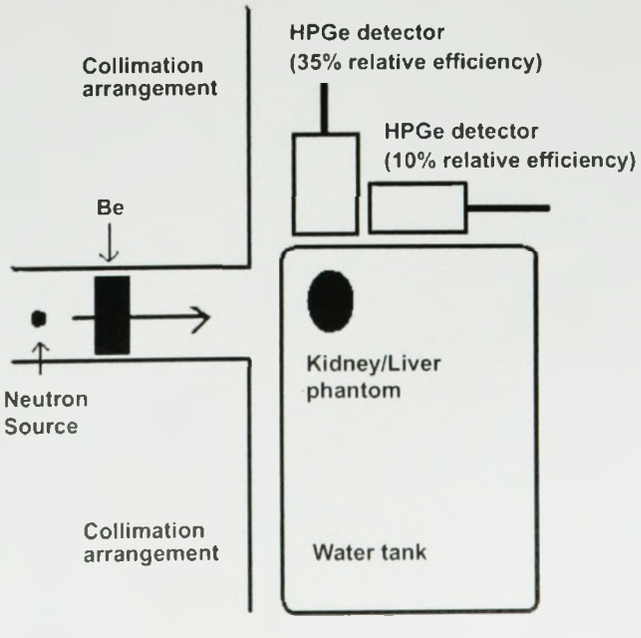

Fig. 1. Schematic diagram of the in vivo prompt gamma neutron activation analysis apparatus (top view, not to scale).

cadmium 559 keV peak areas using a Levenberg–Marquardt fitting algorithm (Press et al., 1992). Although it is easy to determine the peak area for large cadmium concentrations, at concentrations close to the detection limit the fit becomes unstable. In order to fit peaks with small numbers of counts, the peak width was fixed since it is expected to be constant for a given detector and set of electronics during a calibration measurement. Also, the peak position was restricted to fall within a region close to the position previously determined from fitting peaks with high numbers of counts. Once the peak areas were calculated, they were plotted against cadmium mass for the kidney or concentration for the liver to produce a calibration line and cadmium sensitivity was determined. The detection limit was taken as twice the uncertainty in the peak area (σ) of the 0 mg or 0 ppm phantom spectrum divided by the slope of the calibration line:

$$M_{DL} = 2 \times \left(\frac{\sigma}{slope}\right). \quad (1)$$

The results obtained from the two detectors were combined using the inverse variance weighted method in order to deduce the total detection limit.

3. Results

The previous two-detector system (McNeill and Chettle, 1998) was able to achieve a limit of 3.8 mg for the kidney. The detection limit of the older one-detector McMaster system (Fedorowicz et al., 1993) was 8.9 mg for the kidney. The results for liver phantoms had not previously been cited for the current detection system. The above method was used to determine the detection limits for the current two-detector system to be 1.7 mg for the kidney, 4.5 ppm for the 1 L liver and 3.3 ppm for the 2 L liver. All the results described here are for a 2000 s live time. The kidney detection limit is quoted in mg since the kidney is a relatively small organ and thus its total cadmium burden can be measured. The liver is a large organ and as a result can be sampled only. Hence, the liver detection limit is expressed as concentration (ppm). An example of a typical cadmium spectrum with resulting fit curve is shown in Fig. 2. The neutron skin dose rate for the system was measured to be 0.8 mSv h^{-1}, corresponding to about 0.5 mSv for a 2000 s counting time.

Improvement in the kidney detection limit by more than a factor of 2 is primarily due to the optimal placement of system components and detector changes. Source position was optimized by moving the source from its original position at 0 cm and successively moving it closer to the exit of the collimator. A plot of sensitivity and dose rate as a function of source position is shown in Fig. 3. As expected, the dose rate and

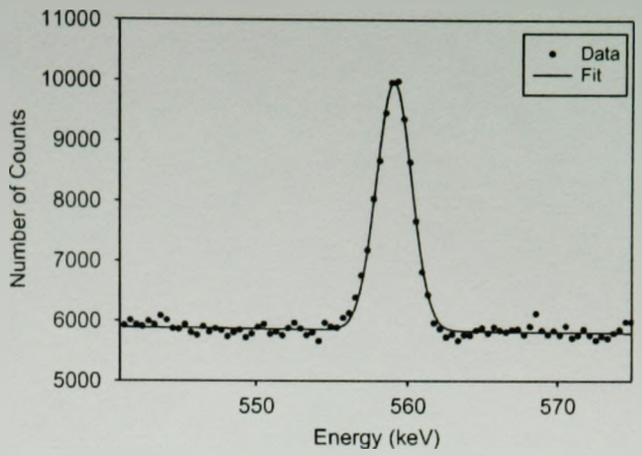

Fig. 2. An example of a spectrum showing the 559 keV peak and resulting fit for a 125 g kidney phantom containing 121 mg of cadmium.

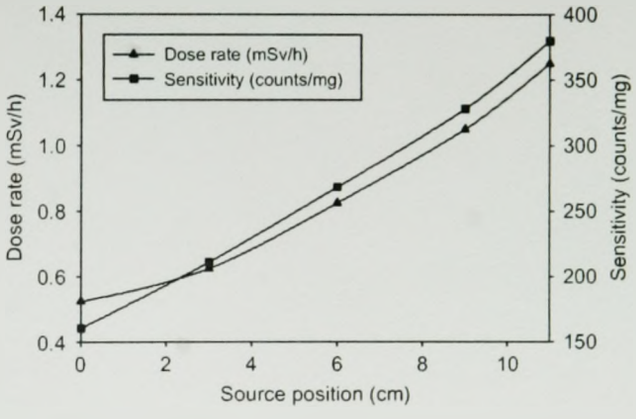

Fig. 3. Dose rate and cadmium sensitivity as a function of ^{238}Pu–Be source position. A larger value for position represents the source being moved closer to the exit of the collimator. Both dose rate and sensitivity increase as the source is moved closer.

sensitivity improve as the source is moved closer to the phantom and detector location. However, sensitivity does not vary greatly with dose rate over the relatively wide source position range. Detection limit and dose rate as a function of source position are plotted in Fig. 4. The detection limit decreases as the source is moved closer to the exit of the collimator, however, there is no more improvement past the 6 cm position although the dose rate continues to increase. Therefore, the 6 cm position was chosen as the optimal source location. Detector changes also lowered the detection limit since the combined efficiency of the two coaxial detectors is better than that of the two planar detectors used in the previous system. The geometry of the two-detector system is improved further as the more efficient detector is now directly in front of the phantom. Although the smaller secondary coaxial detector has a much lower

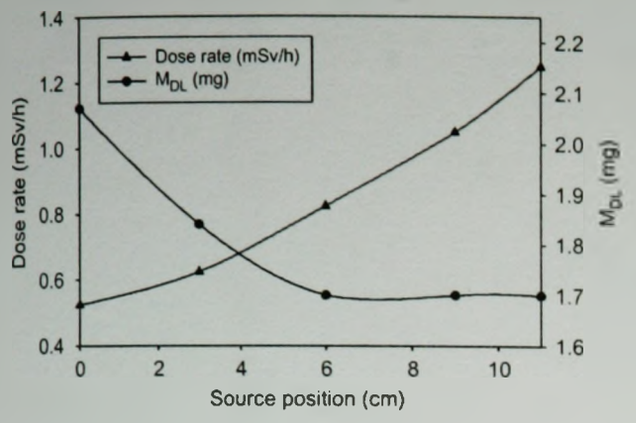

Fig. 4. Dose rate and detection limit as a function of ^{238}Pu–Be source position. There is an improvement in the detection limit as the source is moved closer, but only up to the 6 cm position. At closer distances there is no more improvement in the detection limit while the dose rate increases.

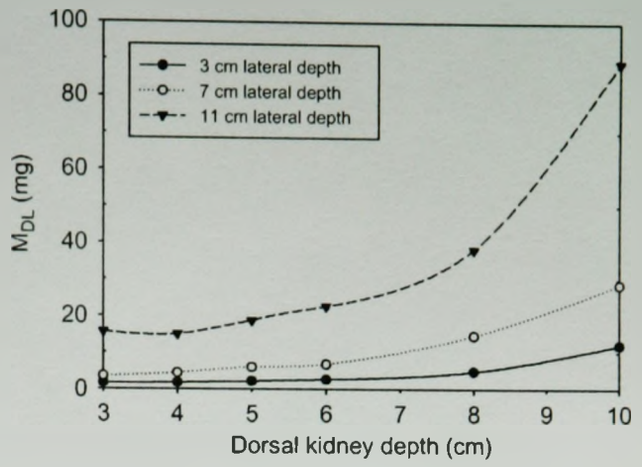

Fig. 5. Detection limit dependence on kidney phantom position. Depth represents the distance between the skin surface and the midpoint of organ.

efficiency, it does lower the detection limit by approximately 10% compared to the large coaxial detector used alone. This demonstrates that a more efficient detector in this position would contribute significantly. The liver detection limit has been lowered by a factor of 1.4 through the course of this work by increasing the size of phantoms to represent the size of the liver more accurately, while maintaining the same Cd concentration. By increasing the size, a larger portion of the phantom was exposed to the neutron beam and the detector field of view, resulting in an increase in cadmium measurement sensitivity.

Kidney position dependence on measurement sensitivity was also investigated. The effect of kidney position on the detection limit is shown in Fig. 5. The detection limit increases as a function of dorsal and lateral depth. This effect is largest for dorsal depths above 6 cm and for each increasing lateral depth. During in vivo studies, the appropriate detection limit would be assigned for an individual following an ultrasound organ depth measurement.

Although the detection limit is a sound way of comparing results, other factors such as skin dose, detector efficiency and resolution need to be included. An evaluation of the performance of an in vivo cadmium neutron activation system can be made through the use of a figure of merit, F, given by

$$F = M_{DL}\left(\frac{DE}{R}\right)^{1/2}, \tag{2}$$

where M_{DL} is the detection limit in mg or ppm (Eq. (1)), D is the skin dose (mSv), E is the detector efficiency (%) and R is the detector resolution (keV). Performance figures for the present system and an overview of other systems are given in Table 1. The figures of merit for the two detectors used in this work are presented individually due to the differences in efficiency, resolution and detection limit. The agreement of the individual figures of merit demonstrates consistency in the performance of the current system.

The figure of merit F, as defined in Eq. (2), is a detector-independent figure since the detector efficiency and resolution are included in the evaluation of system performance. If these factors are omitted, then the figure of merit would be only dependent on the detection limit and the square root of dose, making it a detector-dependent figure. For example, a detector-dependent F for the present system would be 1.5 compared to 2.4 for the previous system (McNeill and Chettle, 1998). However, a detector-independent definition of F was chosen, allowing for comparison of system performance if similar detectors are used.

4. Conclusions

The McMaster in vivo prompt gamma neutron activation analysis system has been improved. The detectors have been upgraded from two large-surface area detectors to a two-detector system with a large volume coaxial and a smaller coaxial detector. Optimal positions for system components were found and the fitting routine was improved. As a result, the detection limit for the kidney has been reduced by more than a factor of 2. The liver detection limit was reduced in the course of this work by a factor of 1.4 through the use of 2 L instead of 1 L liver phantoms. Detection limits presented in this work are sufficiently low to allow for accurate occupational and in some cases environmental cadmium exposure measurements. Future work will involve the use of an accelerator at McMaster University to produce neutrons via the ^{7}Li(p,n)^{7}Be reaction for neutron activation of cadmium. By using

Table 1
Comparison of performance characteristics of Cd detection systems

Laboratory	Organ	Skin Dose (mSv)	M_{DL}	F	Reference (Year)
McMaster	Kidney	0.5	2.0 mg[a]	6.1[a]	Present work (2004)
			3.8 mg[b]	5.9[b]	
McMaster	Kidney	0.4	3.8 mg	5.4	McNeill and Chettle (1998)
McMaster	Kidney	0.4	8.9 mg	10.3	Fedorowicz et al. (1993)
Birmingham	Kidney	1.0	5.2 mg	14.6	Franklin et al. (1990)
Birmingham	Kidney	0.9	6.4 mg	22.7	Chettle et al. (1987)
McMaster	Liver (2L)	0.5	3.8 ppm[a]	11.6[a]	Present work (2004)
			6.2 ppm[b]	9.6[b]	
McMaster	Liver (1L)	0.5	5.1 ppm[a]	15.5[a]	Present work (2004)
			9.1 ppm[b]	14.1[a]	
Birmingham	Liver	0.5	6.5 ppm	17.2	Chettle et al. (1987)
Brookhaven	Liver	4.7	1.5 ppm	10.7	Morgan et al. (1981)
Brisbane	Liver	1.0	6.7 ppm	17.4	Krauel et al. (1980)

[a]Coaxial detector—35% relative efficiency.
[b]Coaxial detector—10% relative efficiency.

low proton energies and thus lower neutron energies, the detection limit and skin dose are expected to improve.

References

Chettle, D.R., Franklin, D.M., Guthrie, C.J.G., Scott, M.C., Somervaille, L.J., 1987. In vivo and in vitro measurements of lead and cadmium. Biol. Trace Elem. Res. 13, 191–208.

Christoffersson, J.-O., Mattsson, S., 1983. Polarised X-rays in XRF-analysis for improved in vivo detectability of cadmium in man. Phys. Med. Biol. 28, 1135–1144.

Fedorowicz, R.P., Chettle, D.R., Kennett, T.J., Prestwich, W.V., Webber, C.E., 1993. A ^{238}Pu/Be facility for in vivo cadmium measurements. In: Ellis, K.J., Eastman, J.D. (Eds.), Human Body Composition. Plenum Press, New York.

Franklin, D.M., Armstrong, R., Chettle, D.R., Scott, M.C., 1990. An improved in vivo neutron activation system for measuring kidney cadmium. Phys. Med. Biol. 35, 1397–1408.

Friberg, L., Piscator, M., Nordberg, G.F., Kjellstrom, T., 1974. In Cadmium in the Environment, second ed. CRC Press, Boca Raton, FL.

ICRP Publication 89, 2003. Basic Anatomical and Physiological Data for Use in Radiological Protection: Reference Values, Pergamon Press, New York.

Krauel, J.B., Speed, M.A., Thomas, B.W., Baddeley, H., Thomas, B.J., 1980. In vivo measurement of organ tissue levels of cadmium. Int. J. Appl. Radiat. Isot. 31, 101–106.

McNeill, F.E., Chettle, D.R., 1998. Improvements to the in vivo measurement of cadmium in the kidney by neutron activation analysis. Appl. Radiat. Isot. 49, 699–700.

Morgan, W.D., Ellis, K.J., Vartskyasumura, S., Cohn, S.H., 1981. Calibration of a ^{238}Pu,Be facility for partial measurements of organ cadmium. Phys. Med. Biol. 26, 577–590.

Press, W.H., Teukolsky, S.A., Vetterling, W.T., Flannery, B.P., 1992. In Numerical Recipes in C, second ed. Cambridge University Press, Cambridge.

2.3 Additional material

Through the optimization of the *in vivo* cadmium PGNAA detection system, the MDL of cadmium in the kidney was improved by more than a factor of 2 and in the liver by a factor of 1.4. This low MDL allows for future non-invasive monitoring of workers who are exposed to cadmium.

Several factors can possibly affect the detection of cadmium in the kidney that were not discussed in the article. One is the fact that most of the cadmium can be found in the cortex, although the phantoms assume a uniform cadmium distribution. This was difficult to check experimentally, therefore simulations were performed using MCNP (Version 5), a general purpose Monte Carlo transport code. By comparing the (n,γ) reaction rates in the kidney for uniformly vs. peripherally distributed cadmium, it was determined that the difference in reaction rate was less than 5%. This is not a significant factor in the detection of cadmium. Another factor that may affect cadmium measurement is the torso size of the subject. Simulations were performed based on real torso sizes for a typical male and female, and the dorsal-to-lateral width ratio was kept fixed as the torso size was varied in the simulation. The simulations showed that the reaction rate was not changed for any torso size (see Figure 2.1). Hence, torso size does not affect the detectability of cadmium using PGNAA.

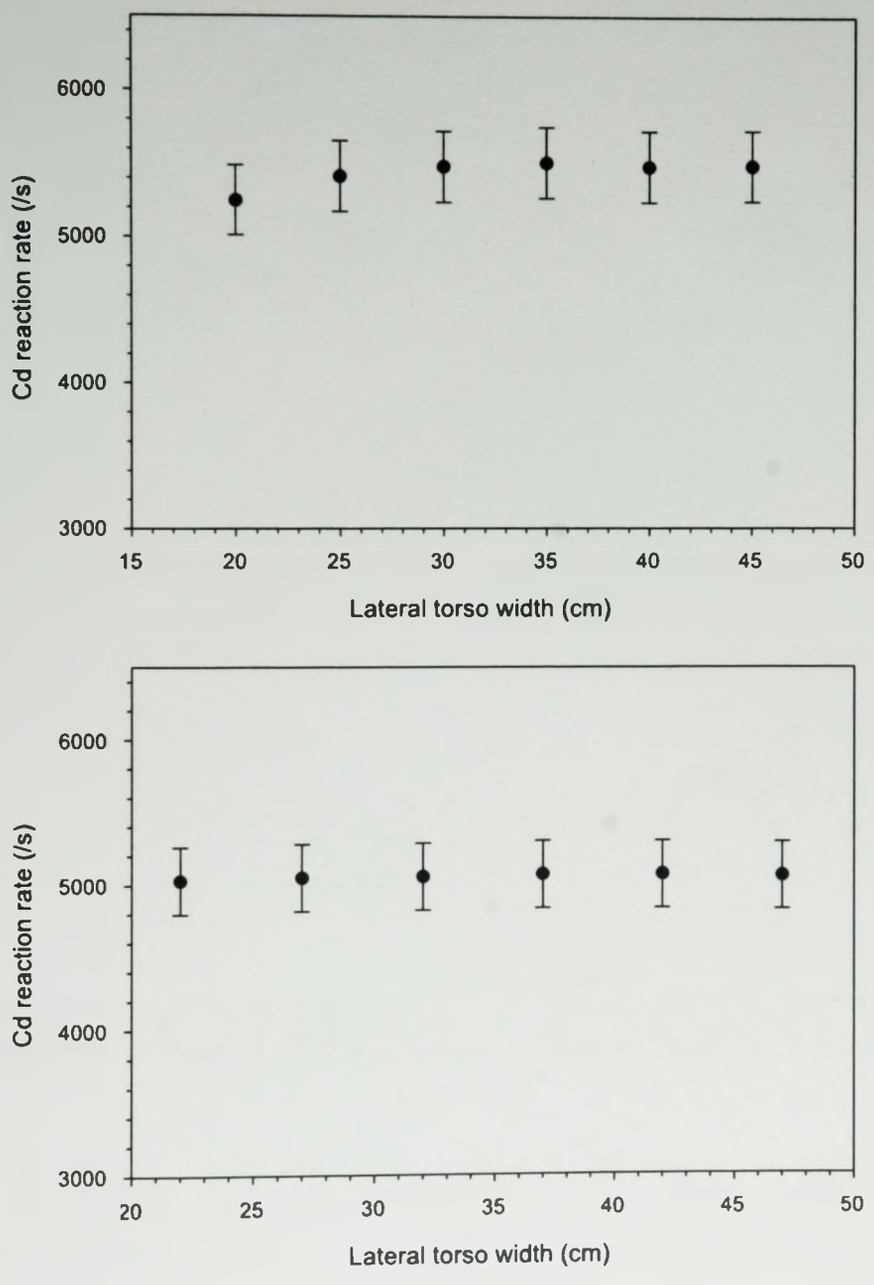

Figure 2.1: Cadmium reaction rate as a function torso size (the error bars represent a 5% relative uncertainty). Top: female torso with 0.57 ratio of dorsal-to-lateral width ratio fixed, kidney located at 3 cm (lateral) and 2 cm (dorsal). Bottom: male torso with 0.71 ratio of dorsal-to-lateral width ratio fixed, kidney located at 4 cm (lateral) and 4 cm (dorsal).

Chapter 3

Phantom Studies of Cd, Hg and Cl by Prompt Gamma Neutron Activation Analysis Using a ^{238}Pu-Be Neutron Source (Article II)

3.1 Introduction to Article II

A natural extension to the method of cadmium detection in Article I is the application of *in vivo* PGNAA to measure mercury burdens in the kidney. By using the cadmium experimental set-up for mercury kidney phantom measurements, and developing a new fit function to the resulting spectrum (see Section 1.5.3), the MDL of mercury was measured to be 315 ppm. This MDL is too high for meaningful *in vivo* measurements

of even extremely mercury-exposed workers. Based on the excellent MDL of cadmium (1.7 mg or equivalently 14 ppm), a better result was expected for mercury. Based on several factors discussed in the article, the MDL of mercury was expected to be about 10 times worse than the MDL of cadmium when in reality it was 23 times worse. Article II explains the reasons for this large MDL discrepancy by comparing ^{113}Cd and ^{199}Hg sensitivity to that of a third isotope, ^{35}Cl.

The work presented in Article II was performed by the author of this thesis with the advice of Dr. Soo-Hyun Byun, and under the supervision of Dr. David Chettle. The McMaster Nuclear Reactor experimental cadmium and mercury data used for comparison with the ^{238}Pu-Be source were supplied by Jovica Atanackovic. The fit functions for mercury and chlorine were developed by the author of this thesis. The manuscript was written by the author of this thesis.

An article that complements Article II is included in the Appendix, in which a simulation-based comparison is made between mercury, cadmium and chlorine. The Appendix article also includes a simulation dosimetry study for the ^{238}Pu-Be-based PGNAA system.

3.2 Contents of Article II

Available online at www.sciencedirect.com
ScienceDirect
Nuclear Instruments and Methods in Physics Research B 263 (2007) 262–265
NIM B
Beam Interactions with Materials & Atoms
www.elsevier.com/locate/nimb

Phantom studies of Cd, Hg and Cl by prompt gamma neutron activation analysis using a ^{238}Pu–Be neutron source

J. Grinyer *, J. Atanackovic, S.H. Byun, D.R. Chettle

Department of Medical Physics and Applied Radiation Sciences, McMaster University, Hamilton, Ontario, Canada

Available online 14 April 2007

Abstract

Prompt gamma neutron activation analysis is a means of non-invasive monitoring for occupational exposure to toxic heavy metals such as Cd and Hg. Preliminary kidney detection limits from previous phantom studies at McMaster were 13.6 ± 0.2 ppm for Cd (125 mL phantom) and 315 ± 24 ppm for Hg (125 mL phantom) using the ^{238}Pu–Be neutron source and 0.88 ± 0.01 ppm for Cd (125 mL phantom) and 16.91 ± 0.05 ppm for Hg (30 mL phantom) using the thermal neutron beam port at the McMaster Nuclear Reactor. The detection limits vary greatly between the two methods due to differences in experimental set-up, neutron energy spectra and a difference in dose by more than a factor of 100. The Hg detection limit from preliminary data is much higher than expected for both neutron source types. In order to explain the apparent detection limit discrepancy, measurements of Hg and Cd phantoms were performed using the ^{238}Pu–Be neutron source. The results were compared to phantom measurements of Cl, a well-known neutron activation element.

PACS: 29.30.Kv; 29.40.Wk; 82.80.Jp

Keywords: Neutron activation analysis; Cd; Hg; Cl; Detection limit

1. Introduction

Heavy metals, such as Cd and Hg, are toxic substances that enter the human body from environmental and industrial sources. Cd is known to accumulate in the liver and kidneys, leading to various adverse health effects. Following chronic exposure, usually as a result of occupational exposure, conditions such as kidney dysfunction, emphysema, osteoporosis and osteomalacia may develop [1]. Inorganic Hg accumulates in the kidney, therefore kidney dysfunction can result from occupational exposure [2]. Impairment of kidney function is difficult to diagnose before irreversible damage is already done and thus it is important to assess the total Hg or Cd organ burden of workers. If the accumulation of dangerous levels of these toxic heavy metals can be avoided, then adverse health effects mentioned above can be prevented.

In vivo prompt gamma neutron activation analysis (PGNAA) is a non-invasive method of measuring the total organ burden of Hg or Cd. This method has been used previously for Cd measurements with a ^{238}Pu–Be neutron source [3]. An existing ^{238}Pu–Be *in vivo* PGNAA system at McMaster University was recently optimized to lower the Cd kidney detection limit to 13.6 ± 0.2 ppm (125 mL phantom), a more than a factor of 2 improvement [4]. Due to encouraging Cd results, the possibility of Hg detection using the current system was explored. The Hg detection limit attained using the optimized system was disappointingly high at 315 ± 24 ppm (125 mL phantom). In order to perform *in vivo* measurements, a detection limit of 10 ppm or less is required.

A feasibility project for *in vivo* PGNAA of Cd and Hg using the thermal beam port at the McMaster Nuclear Reactor (MNR) was started recently [5]. The detection

* Corresponding author.
E-mail address: grinyej@mcmaster.ca (J. Grinyer).

0168-583X/$ - see front matter © 2007 Elsevier B.V. All rights reserved.
doi:10.1016/j.nimb.2007.04.106

limits in this bare phantom study were 0.88 ± 0.01 ppm for Cd (125 mL phantom) and 16.91 ± 0.05 ppm for Hg (30 mL phantom). Although these detection limits are lower than the ^{238}Pu–Be system results, at this time the irradiation conditions are not suitable for *in vivo* measurements, both due to high dose and a constrained irradiation geometry.

There is a discrepancy between the relative detectability of Hg and Cd, based on detection limits for both systems quoted above. Although the two systems are quite different, in each case the detection limit of Hg is about 20 times worse (23 for ^{238}Pu–Be; 19 for thermal beam port at MNR) than that of Cd. The expected value is 10 times worse, based on k_0-factors, relative γ-ray efficiencies and differences in background for the two elements (see Section 3). The aim of the present study is to find the source of this discrepancy by comparing the detectability of Hg and Cd to Cl, an element with a wide energy range of well-known prompt γ-rays.

2. Experimental method

The ^{238}Pu–Be PGNAA system at McMaster is composed of a collimation apparatus which houses two sources with a combined activity of 17 Ci and also acts as a neutron shield. The neutron spectrum for the ^{238}Pu–Be source includes thermal, intermediate and fast neutrons. Before moderation, the average neutron energy is 4 MeV. Sources are placed within a steel cylinder, which is in turn surrounded by a graphite cylinder. Alternating sheets of polyethylene and steel are placed around the source and cylinders to collimate the beam. The collimation apparatus has a built-in Be moderator as well as shielding for detectors. The entire arrangement is surrounded by borated resin panels. A water tank simulating the human torso is placed at the exit of the collimator and kidney phantoms are placed within it. Details of the experimental apparatus and system optimization have been described elsewhere [4,6]. The optimized system has two coaxial HPGe detectors, however, for ease of comparison between different elements in this study only the more efficient detector was used (58 mm diameter × 57 mm length, 35% efficiency relative to a 3 in. × 3 in. NaI detector at 1.33 MeV). This detector was placed as close as possible to the water tank, at a 90° angle to the neutron beam. A schematic diagram of the experimental layout is shown in Fig. 1.

Polyethylene kidney phantoms (125 mL) filled with known concentrations of Hg, Cd or Cl were irradiated with neutrons and prompt γ-ray spectra were collected simultaneously with irradiation. For each element, phantoms with varying concentrations were measured: Cd concentrations ranged from 0 to 970 ppm, Hg concentrations ranged from 0 to 2500 ppm and Cl concentrations ranged from 0 to 100,000 ppm. These particular ranges were chosen such that the spectrum for the most concentrated phantoms for each element would clearly show the γ rays of interest. Phantoms were placed in a water tank (torso) and the spectra were collected over 2000 s live time to simulate an *in vivo* measurement. γ-ray peaks were fit using the Levenberg–Marquardt algorithm [7]. A calibration line (number of counts in a peak as a function of concentration) was plotted for Hg, Cd and Cl in order to determine measurement sensitivity (S, slope) and the detection limit (M_{DL}). The M_{DL} is defined as twice the peak area uncertainty in the 0 ppm phantom, σ_0, divided by the slope, S:

$$M_{DL} = 2 \times \left(\frac{\sigma_0}{S}\right). \quad (1)$$

The sensitivity and the detection limit of Hg and Cd were determined via their most intense γ-rays at 368 keV and 559 keV, respectively. The 517 keV Cl γ-ray was selected as closest in energy to the 368 keV and 559 keV peaks. Expected and experimental sensitivities and detection limits of Hg, Cd and Cl were compared for the ^{238}Pu–Be PGNAA system. Several higher energy Cl peaks were analyzed to make a comparison of sensitivity and detection limit to their respective k_0 values.

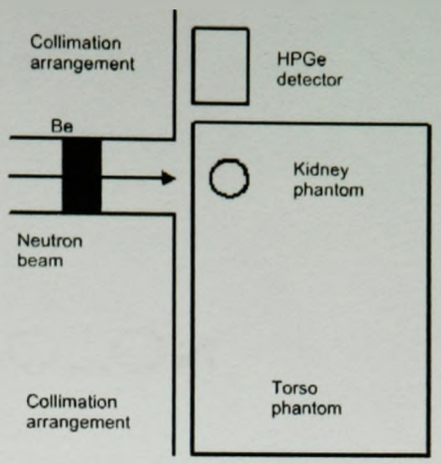

Fig. 1. Schematic diagram of the ^{238}Pu–Be prompt gamma neutron activation analysis apparatus (top view, not to scale).

3. Results and discussion

After collecting spectra for Hg, Cd and Cl on each system, the corresponding γ-ray peaks were fit to obtain peak areas. Calibration lines were plotted to obtain sensitivities and detection limits were calculated using Eq. (1). All results are listed in Table 1. Here, k_0 represents a calibration constant used for PGNAA and has a facility-independent nature [9]. Although there are other prompt γ-rays for Cd and Hg, only the most intense were considered. At the minimal concentrations encountered in an *in vivo* measurement, less intense peaks would not be visible.

When comparing the results for Cl γ-rays in Table 1, one can see there is a relationship between S and k_0. As expected, the sensitivity decreases with corresponding k_0 value. In the case of the 6110 keV γ-ray, the significantly lower efficiency of the detector at this energy contributes

Table 1
Experimental results with corresponding k_0 value

Isotope of interest	γ-ray (keV)	S (counts/ppm)	M_{DL} (ppm)	k_0 [8]
^{199}Hg	368	2.62 ± 0.23	363.8 ± 32.0	3.79
^{113}Cd	559	3.27 ± 0.4	15.7 ± 0.2	5.01
^{35}Cl	517	0.196 ± 0.005	3173 ± 81	0.648
^{35}Cl	1164	0.190 ± 0.003	3037 ± 51	0.762
^{35}Cl	1951	0.122 ± 0.004	6759 ± 247	0.541
^{35}Cl	1959	0.056 ± 0.004	14798 ± 1152	0.350
^{35}Cl	6110	0.038 ± 0.002	7032 ± 276	0.563

to a lower S value, despite a relatively high k_0. Similarly, there is in general an inverse relationship between M_{DL} and k_0.

In order to compare the relative detectability of Hg, Cd and Cl, expected and experimental sensitivity ratios were calculated and compared. For Cl, only the 517 keV γ-ray was considered since it is closest in energy to Hg and Cd lines and as such allows a relatively simple comparison. Sensitivity is proportional to k_0 and detector efficiency, ε, therefore the expected sensitivity ratio, S_x/S_y, is approximated by

$$\frac{S_x}{S_y} = \left(\frac{k_{0,x}}{k_{0,y}}\right)\left(\frac{\varepsilon_x}{\varepsilon_y}\right). \tag{2}$$

In Eq. (2), k_0 values were taken from [8] and ε was assumed to be the equal for 517 and 559 keV γ-rays. The efficiency at 368 keV was 1.97 times better than at 517 or 559 keV from a previous detector calibration. The experimental ratios were calculated using respective data from Table 1. Table 2 compares the expected and experimental sensitivity ratios. The ratio of Cd to Hg or Cl is approximately a factor of 2 greater than expected, while the ratio of Hg to Cl is close to the expected value. This suggests that the Cd result may be the source of measurement discrepancy.

To explore this possibility further, relative detection limits were included to take account of differences in background under the 368, 517 and 559 keV γ-rays (see Table 3). Since the detection limit is inversely proportional to sensitivity, S, and proportional to the uncertainty in background, σ, the expected ratio, $M_{DL,x}/M_{DL,y}$, is defined as:

$$\frac{M_{DL,x}}{M_{DL,y}} = \left(\frac{S_y}{S_x}\right)\left(\frac{\sigma_x}{\sigma_y}\right). \tag{3}$$

The level of relative background signal at 517 and 559 keV was assumed to be equal, while the background at 368 keV was approximately 2.5 times greater. Therefore, a value of $\sqrt{2.5}$ was assigned to σ_{Hg} in Eq. (3). This assumes that the signal to background ratio is $\ll 1$, as is the case here since the M_{DL} is found using the 0 ppm phantom (see Eq. (1)). Experimental M_{DL} ratios were calculated from measured values in Table 1. As seen in Table 3, the M_{DL} ratio of Hg or Cl to Cd is approximately a factor of 2 greater, even after accounting for the difference in background between the 368 and 559 keV γ-rays. The ratio between Cl and Hg is not as close to expected value as in the case of the sensitivity ratio. This may be due to the questionable assumption that the background at 517 and 559 keV is equal. In reality, the background at 517 keV is slightly higher than at 559 keV due to the close proximity of the 511 keV annihilation peak (see Fig. 2). It is difficult to account for this type of background so it can be compared directly to the background under the 368 keV. Thus, in the case of Hg and Cl, the sensitivity ratio is a better way to compare their relative detectability.

By comparing the sensitivity and detection limit ratios for Hg, Cd and Cl, it was shown that in each case the experimental Cd values were about a factor of 2 better than expected. The reason for the discrepancy is that the sensitivity estimation used in Eq. (2) is an approximation and correction factors for neutron spectrum and capture cross-section are needed [10]; however, this is beyond the scope of the present study. Both Cl and Hg are $1/v$ neutron absorbers and are not influenced by correction factors. Since ^{113}Cd is not a $1/v$ isotope, its neutron capture cross-section is heavily dependent on the neutron spectrum, and as such its k_0 value may vary by more than a factor of 2 [10]. Since the ^{238}Pu–Be source has a wide spectrum of neutron energies, it would not be surprising for correction factors for Cd k_0 to reach a factor of 2. Although it would be useful to verify this through simulation with a general purpose Monte Carlo transport code such as MCNP, no γ production data from (n, γ) reactions are available for Cd and Hg in the current version (MCNP5) and as such a comparison to experimental data is not straightforward and beyond the scope of this experimental study.

A preliminary result using the thermal beam port at MNR shows that the M_{DL} ratio of Cd to Hg (125 mL phantoms) is 14.9, which is lower than the corresponding ratio of 23.2 obtained with the ^{238}Pu–Be source. As expected, the greater degree of neutron thermalization at the MNR thermal beam port gives a ratio that is closer to the expected value. With a more thermalized beam, the departure from the k_0 value is not as pronounced as it is for the ^{238}Pu–Be neutron source.

Table 2
Comparison of expected and experimental sensitivity, S

	Expected	Experimental result
S_{Cd}/S_{Hg}	6.7	12.5
S_{Cd}/S_{Cl}	77.3	166.8
S_{Hg}/S_{Cl}	11.5	13.4

S_{Cl} refers to the 517 keV result.

Table 3
Comparison of expected and experimental detection limit, M_{DL}

	Expected	Experimental result
$M_{DL,Hg}/M_{DL,Cd}$	10.6	23.2
$M_{DL,Cl}/M_{DL,Cd}$	77.3	202.1
$M_{DL,Cl}/M_{DL,Hg}$	7.3	13.6

$M_{DL,Cl}$ refers to the 517 keV result.

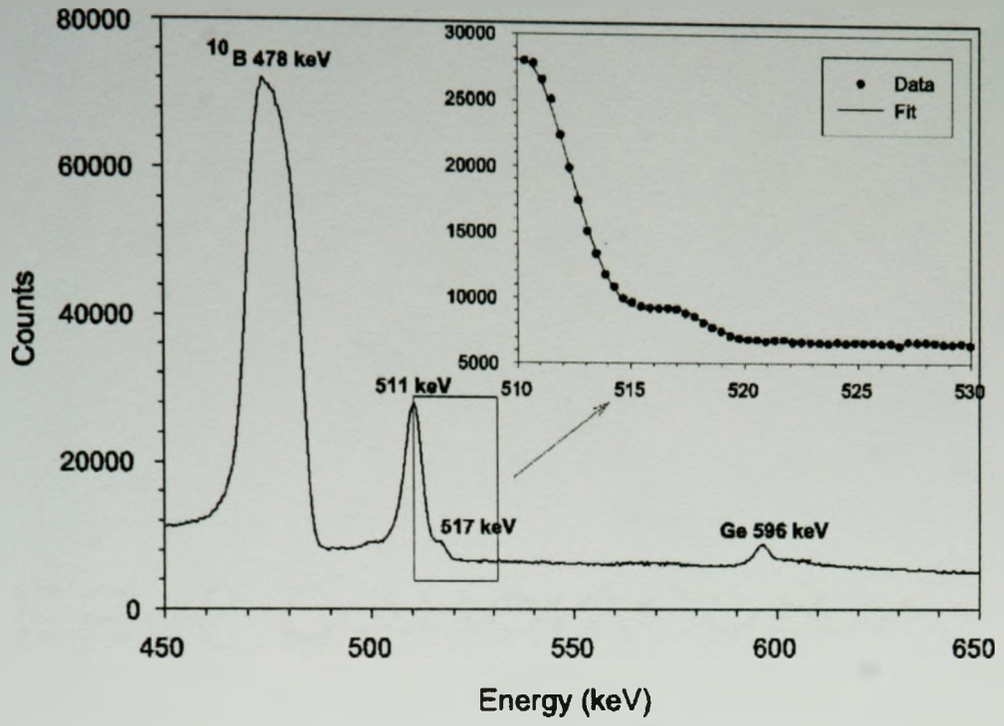

Fig. 2. γ-ray spectrum acquired with a 100,000 ppm Cl phantom. In order to fit the Cl 517 keV γ-ray, a portion of the 511 keV annihilation peak was included in the fit.

4. Conclusion

Sensitivities and detection limits of Hg and Cd were compared with those of Cl, a well-known neutron activation element. In order to make a relatively simple comparison with Cl, only the 517 keV γ-ray was considered since it lies between the Hg and Cd γ-rays of interest. The detectability of Cd was a factor of 2 greater than expected when compared to Hg and Cl. This is due to the highly non $1/v$ behaviour of the ^{113}Cd cross-section and as such the k_0 value can vary by more than a factor of 2 depending on the neutron spectrum. In the case of the ^{238}Pu–Be neutron source, used in an *in vivo* PGNAA system at McMaster University, neutrons have energies ranging up to 11 MeV and in particular are expected to have a greater proportion of neutrons in the 0.1–0.5 eV range than the thermal beam port. As a result, the k_0 value is higher than expected, allowing for an enhanced detection of Cd. The same is not true for Hg, since ^{199}Hg is a $1/v$ isotope. Through the course of this phantom study, the source of the detection limit discrepancy between Cd and Hg was found to be the enhanced detectability of Cd due to the increased neutron capture cross-section at higher neutron energies.

References

[1] L. Friberg, M. Piscator, G.F. Nordberg, T. Kjellstrom, Cd in the Environment, second ed., CRC Press, 1974.
[2] World Health Organisation, Environmental Health Criteria No. 118: Inorganic Mercury, Geneva, 1991.
[3] D.M. Franklin, R. Armstrong, D.R. Chettle, M.C. Scott, Phys. Med. Biol. 35 (1990) 1397.
[4] J. Grinyer, S.H. Byun, D.R. Chettle, Appl. Radiat. Isotopes 63 (2005) 475.
[5] J. Atanackovic, M.Sc. Thesis, McMaster University, 2004.
[6] R.P. Fedorowicz, D.R. Chettle, T.J. Kennett, W.V. Prestwich, C.E. Webber, et al., in: K.J. Ellis, J.D. Eastman (Eds.), Human Body Composition, Plenum Press, New York, 1993.
[7] W.H. Press, S.A. Teukolsky, W.T. Vetterling, B.P. Flannery, Numerical Recipes in C, second ed., Cambridge University Press, 1992.
[8] IAEA Database for PGNAA, website: www-nds.iaea.org/pgaa/.
[9] G.L. Molnár, Zs. Révay, R.L. Paul, R.M. Lindstrom, J. Radioanal. Nucl. Chem. 234 (1998) 21.
[10] G.M. Sun, S.H. Byun, H.D. Choi, J. Radioanal. Nucl. Chem. 256 (2003) 541.

Chapter 4

Detection of Mercury in the Kidney via Source-excited X-ray Fluorescence (Article III)

4.1 Introduction to Article III

Article II explained some of the reasons behind the unexpectedly high mercury MDL of 315 ppm using PGNAA. In order to be feasible for *in vivo* measurements, the MDL would have to be reduced by more than an order of magnitude. Although small improvements to the system are possible these would not increase the mercury sensitivity on a grand scale. As a result, PGNAA for the detection of mercury was abandoned and a different approach was taken: XRF. In theory, PGNAA would be a preferable method of measuring mercury in the kidney since it is a relatively deep organ, however past experiments with polarized XRF (Börjesson et al., 1995, O'Meara et al., 2000) yielded promising results.

Article III considers the detection of mercury in the kidney with a source-excited XRF system consisting of a ^{109}Cd gamma-ray source, source collimator, planar HPGe detector and torso and kidney phantoms. X-ray fluorescence spectrum fitting was developed (see Section 1.5.5) for mercury in order to extract x-ray peak areas. Article III describes detection feasibility experiments with bare kidney phantoms as well as measurements simulating an *in vivo* setting. The MDL of mercury obtained with source-excited XRF during the course of this study is low enough to attempt future measurements of occupationally exposed individuals.

The experiments in Article III were performed by the author of this thesis under the supervision of Dr. David Chettle. Dr. Marija Popovic helped in the set-up of the ^{109}Cd source and collimator. The fit functions for the K x-ray peaks and the coherent peak were developed by the author of this thesis. The manuscript was written by the author of this thesis.

4.2 Contents of Article III

X-RAY SPECTROMETRY
X-Ray Spectrom. 2007; **36**: 99–103
Published online in Wiley InterScience
(www.interscience.wiley.com) DOI: 10.1002/xrs.952

X-RAY Spectrometry

Detection of mercury in the kidney via source-excited x-ray fluorescence†

J. Grinyer,* M. Popovic and D. R. Chettle

Medical Physics and Applied Radiation Sciences, McMaster University, Hamilton, ON, L8S 4K1, Canada

Received 6 July 2006; Revised 14 December 2006; Accepted 19 December 2006

Non-invasive detection of kidney Hg *in vivo* is important in order to prevent detrimental health effects in occupationally exposed persons. In this study, preliminary results of a ^{109}Cd source-based x-ray fluorescence system for the detection of Hg in the kidney are presented. The system includes a single 50 mm diameter HPGe detector with a ^{109}Cd source mounted on the detector face for backscatter measurement geometry. A detection limit of 3.9 ppm was obtained during a bare kidney phantom feasibility study. In order to simulate an *in vivo* measurement, kidney phantoms were also placed inside a water tank representing the torso. The detection limit was 5.0 ppm at 1 cm phantom depth, as measured to the phantom boundary. As expected, Hg sensitivity decreased with kidney depth owing to the attenuation of incident ^{109}Cd γ-rays and emitted characteristic Hg K x-rays, so that at a phantom depth of 4 cm the detection limit was 44 ppm. Further improvements to the detection limit will allow future *in vivo* kidney Hg measurements of chronically exposed workers. Copyright © 2007 John Wiley & Sons, Ltd.

INTRODUCTION

Mercury is a trace metal normally present in minute amounts in the human body, typically in the form of organic Hg from dietary sources such as ingestion of fish.[1,2] Organic Hg typically affects the central nervous system and is particularly important in prenatal and childhood exposure, because it can affect brain development in children.[1] In occupational settings, inhalation of inorganic Hg and its subsequent accumulation in kidneys is of particular concern. Typical Hg kidney concentrations in workers are on the order of 25 ppm, while the general population shows concentrations of less than 1 ppm.[3–5] Chronic occupational exposure to Hg vapour can occur in a number of industries, such as Hg and Au mining and processing or battery and thermometer factories.[1,6] Inorganic Hg accumulates in the kidney, and it is this site that is at most risk to damage.[2] High levels of Hg in the kidney may lead to kidney dysfunction, usually without symptoms before irreversible damage is already done.[1,2] Damage to kidney glomeruli can lead to nephrotic syndrome in severe cases of exposure. In addition, nervous system effects such as tremor, loss of coordination, memory disturbances, vision disturbances and irritability can occur; however, it is unclear what levels of exposure induce these effects.[1,7] It is important to monitor the level of exposure to this metal in workers using a reliable, non-invasive method that can measure the total organ burden. Currently, the most common way to monitor Hg levels in the kidney is by testing blood or urine; however, the relationship between blood or urine Hg concentration and Hg content in the kidney is not well known.[3] In order to assess the total organ burden, measurement techniques using x-ray fluorescence (XRF) and prompt gamma neutron activation analysis (PGNAA) have been explored in past studies.

Preliminary investigations into detection of Hg *in vivo* by Smith *et al.*[8] included both PGNAA and XRF. In this previous PGNAA study, a detection limit of 50 ppm was achieved for an Hg kidney phantom inside a torso phantom. The detection limit using source-excited XRF with ^{57}Co and an 85° detection geometry on bare kidney phantoms was 44 ppm.

More recently, Börjesson *et al.*[3] used polarized Hg XRF with an x-ray therapy apparatus to achieve a detection limit of 25 ppm in 90° detection geometry for a 50 min measurement. The same apparatus was used in an *in vivo* study measuring the Hg kidney burden of occupationally exposed workers; however, this measurement only provided information on whether Hg was present in the kidney and did not yield a measurable concentration because of the relatively high detection limit.[3,6] O'Meara *et al.*,[9] after optimizing a polarized Hg XRF system at McMaster University, reported a 26 ppm detection limit for a 2 cm lateral kidney depth, 5 cm dorsal depth, in 90° detection geometry for a 30 min measurement. Additionally, recent PGNAA experiments at McMaster University, using a ^{238}Pu–Be neutron activation analysis system for the detection of Cd in the liver and kidneys,[10] yielded an unsuitably high Hg detection limit of 315 ppm.[11,12]

The detection limit of Hg in the kidney, whether obtained by polarized XRF or PGNAA, remains too high and has to be lowered in order to perform meaningful *in vivo* measurements. The aim of this work was to determine the feasibility of measuring kidney Hg with a source-excited XRF system using ^{109}Cd and a 180° detection geometry. The first

*Correspondence to: J. Grinyer, Medical Physics and Applied Radiation Sciences, McMaster University, 1280 Main St. West, Nuclear Research Building 124, Hamilton, ON L8S 4K1, Canada.
E-mail: grinyej@mcmaster.ca

†Paper presented as part of a special issue of papers from the 2006 European X-ray Spectrometry Conference, Paris, France, 19–23 June. Part 2.

X-RAY Spectrometry

series of experiments was a feasibility study on bare kidney phantoms, and the second series was the determination of the detection limit when the kidney phantom was placed in a torso phantom to simulate an *in vivo* measurement. Finally, the dependence of the detection limit on kidney depth was investigated. The goal of this work is to develop a technique for the measurement of Hg such that in the future *in vivo* monitoring of Hg in the kidney of occupationally exposed individuals will be possible in order to prevent detrimental health effects.

EXPERIMENTAL

The source-excited *in vivo* Hg XRF detection system is shown in Fig. 1. The system consists of a planar high-purity germanium (HPGe) detector of 50 mm diameter and 19 mm thickness (Canberra model GL2020R), a collimated ^{109}Cd excitation source in backscatter (180°) geometry and an aqueous 125 ml kidney phantom containing a known concentration of Hg solution in a polyethylene water tank, which represents the torso. Varying kidney phantom concentrations were used, ranging from 0 to 2500 ppm of Hg. Upon irradiation of the phantom, the resulting photon spectrum was acquired using the Canberra DSA-2000 digital spectrum analyzer.

The excitation source used in the Hg detection system is an encapsulated ^{109}Cd source (electroplated within a steel shell that surrounds a tungsten backing), housed in a tungsten collimator with a 6.0 mm diameter opening (Fig. 2). The 0.7 mm thick Cu filter at the opening of the collimator acts to attenuate nearly all Ag K x-rays (energies between 22 and 25 keV), which also are emitted by the ^{109}Cd source, in order to reduce unnecessary photons entering the detector. At the time of measurements, the source activity was approximately 0.25 GBq. The source emits 88.0 keV γ-rays; this energy is slightly above the 83.1 keV K-edge of Hg. This leads to the emission of a wide range of characteristic x-rays; however, only the K x-rays (energies greater than 68.9 keV) can be used in Hg detection because of the significant attenuation of lower energy x-rays in the torso.

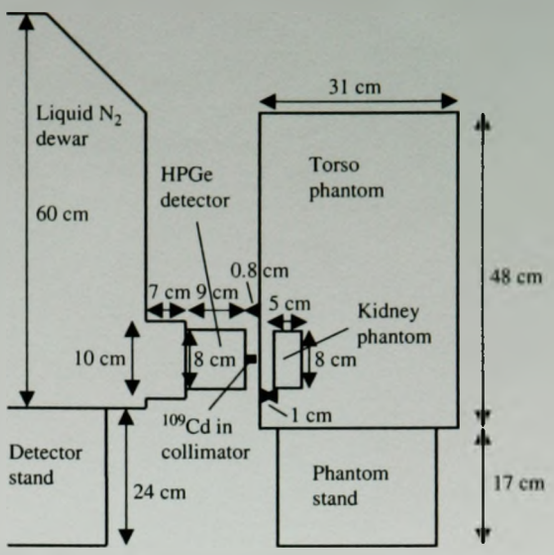

Figure 1. Side view of the source-excited XRF system for the detection of Hg in the kidney.

Bare phantom measurements: detection feasibility

For Hg detection feasibility measurements, the water tank was removed and only the bare phantom was used. The phantom was placed in front of the exit of the collimator such that the collimator exit-to-phantom distance was 2 cm for the bare phantom experiments (Fig. 2). Spectra were collected for 2000 s live time for each phantom concentration.

Measurements of kidney phantoms in the torso phantom

The kidney phantom was placed in the water tank at 1 cm depth from the tank boundary. The tank was placed against the collimator exit such that the total collimator exit-to-phantom distance was approximately 1.3 cm (tank wall is about 0.3 cm thick). The effect of kidney depth was also investigated by placing the kidney phantom at prescribed depths in the water tank. Each phantom was measured for 2000 s live time.

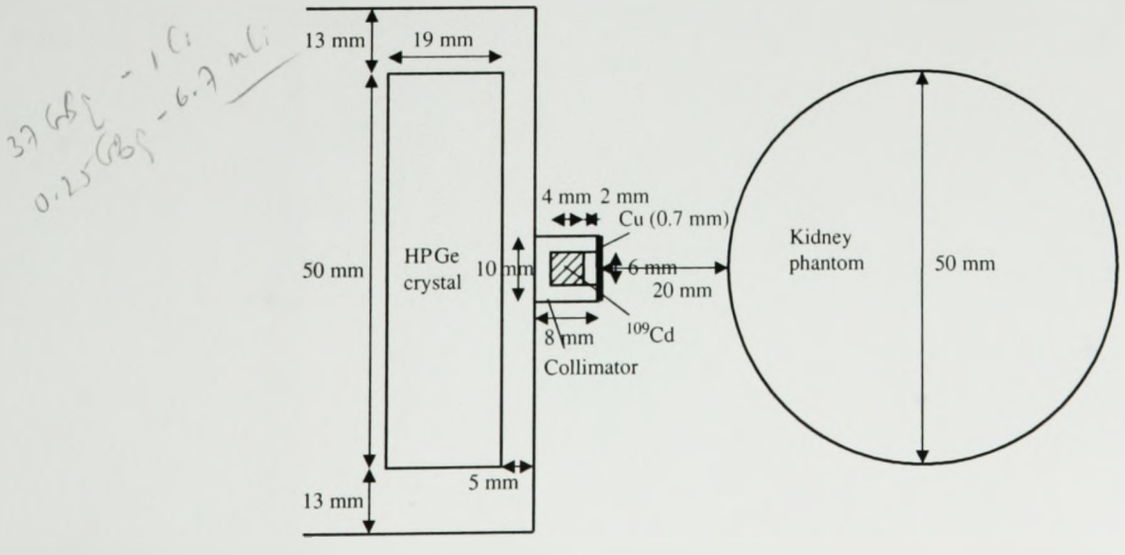

Figure 2. Top view of the bare phantom experimental set-up.

X-Ray Spectrom. 2007; **36**: 99–103
DOI: 10.1002/xrs

Minimum detection limit determination

Spectra were collected and peaks of interest were fit with the Levenberg–Marquardt algorithm[13] to obtain the peak area. X-ray peaks used in the analysis were the Kα, Kβ, $KO_{2,3}$ and the coherent scatter peak at 88.0 keV. The Kα, Kβ and $KO_{2,3}$ lines are a characteristic signature of Hg in the kidney phantom, and all are utilized to achieve a greater detection sensitivity. Since each K line emitted by Hg in the sample is independent of another line, this contributes to a reduction in the final minimum detection limit (MDL) (see 'Results and Discussion'). Owing to the complicated nature of the resulting spectrum and the close proximity of certain peaks, $K\alpha_1$ and $K\alpha_2$ were analyzed together with their relative Gaussian amplitudes fixed in order to stabilize the fit. The same procedure was used for the $K\beta_1$ and $K\beta_3$ peaks, and the $K\beta_{2'}$, $K\beta_{2''}$ and $KO_{2,3}$ peak combination (Fig. 3 inset). Once the peak areas were calculated, the number of counts in a given peak as a function of phantom concentration was plotted to obtain a calibration line. The MDL was calculated from

$$MDL = 2 \times \left(\frac{\sigma}{slope}\right) \quad (1)$$

where σ is the uncertainty in the 0 ppm phantom area (i.e. the uncertainty in the background as the peak area tends to zero) and 'slope' refers to the slope of the calibration line. The use of the above definition is appropriate for *in vivo* measurements since it allows for background and peak variation that is common from person to person. The uncertainty in background varies relatively slowly, and therefore any changes in background under Hg K x-ray peaks between individuals will have a relatively small effect on the MDL as defined in Eqn (1).[14,15] Since this work is a feasibility study with the aim of performing future *in vivo* measurements, such a definition is suitable in this context.

MDL values were calculated using Eqn (1) for each of the peak combinations described above and the coherent scatter peak, and combined using inverse variance weighted method:

$$\left(\frac{1}{MDL}\right)^2 = \left(\frac{1}{MDL_{K\alpha_1 \& K\alpha_2}}\right)^2 + \left(\frac{1}{MDL_{K\beta_1 \& K\beta_3}}\right)^2 + \left(\frac{1}{MDL_{K\beta_{2'}, K\beta_{2''} \& KO_{2,3}}}\right)^2 + \left(\frac{1}{MDL_{coh}}\right)^2 \quad (2)$$

to determine the final MDL value.

RESULTS AND DISCUSSION

A bare phantom spectrum collected using a 2500 ppm kidney phantom for 2000 s live time (corresponding to approximately 2100 s clock time) is shown in Fig. 3. For measurement feasibility studies as in the current work, the use of live time *versus* clock time does not make a difference; however, in any future *in vivo* measurements clock time would be used in order to accurately assess the dose received by the patient. The main feature and source of background in the vicinity of Hg K x-rays is the ^{109}Cd backscatter Compton peak at 66 keV. Although the Kα peaks are the most prominent x-rays in the spectrum, the underlying Compton background increases the Kα MDL because of an increased uncertainty in the background (Eqn (1)). This effect is more pronounced for the water tank spectra since there is an increase in Compton backscatter due to the presence of water.

A typical fit of $K\beta_1$ and $K\beta_3$ peaks from a phantom inside the water tank is shown in Fig. 4.

The resulting MDL values in ppm for each peak combination and the total MDL (calculated using inverse variance, Eqn (2)) are shown in Table 1. Since each characteristic Hg K x-ray emission is an independent event, the additional information provided by fitting each peak combination as described above and finding the individual MDL for each fit contribute to lowering the total MDL. For example, $K\beta_1$ and $K\beta_3$ peaks for bare kidney phantoms give an MDL of 4.6 ppm, and including the Kα peaks in the calculation would lower the MDL to 4.1 ppm (Eqn (2)). Therefore, extracting additional information by fitting Kα, Kβ, $KO_{2,3}$ peaks and

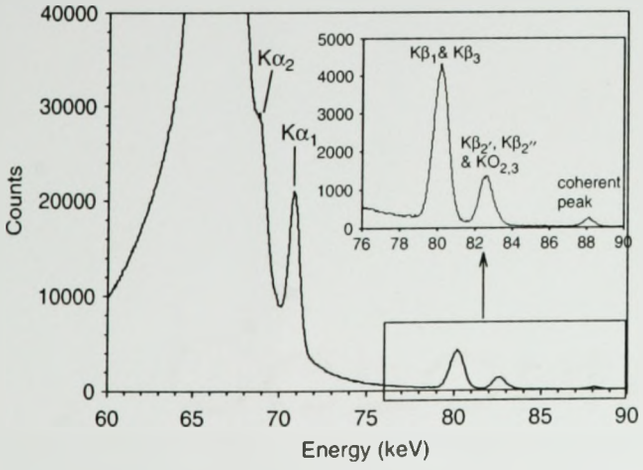

Figure 3. Spectrum of a bare phantom containing 2500 ppm of Hg. All characteristic x-rays of interest are on the upper energy side of Compton scatter peak from the 88 keV γ-rays emitted by the source.

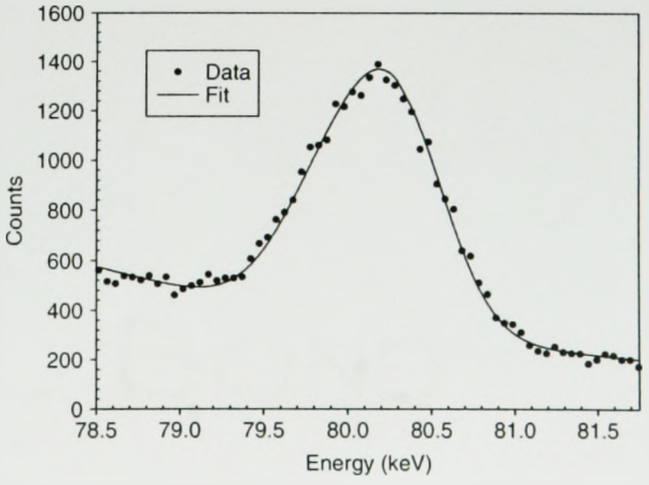

Figure 4. Example of a $K\beta_1$ and $K\beta_3$ fit (reduced $\chi^2 = 1.5$) to data from a 500 ppm kidney phantom at 1 cm depth in a torso phantom.

X-Ray Spectrom. 2007; **36**: 99–103
DOI: 10.1002/xrs

X-RAY Spectrometry

the coherent peak at 88 keV lowers the MDL to a final value of 3.9 ppm. The $K\beta_1$ and $K\beta_3$ peaks contribute most to lowering the MDL owing to the presence of the large Compton peak, as mentioned above. Although the MDL value from the coherent peak does not lower the final MDL significantly, by itself it gives a better MDL than the PGNAA value of 315 ppm.[11,12] This further highlights that XRF is a superior method to PGNAA in the detection of Hg *in vivo*.

The final MDL values of 3.9 ppm for the bare kidney phantoms and 5.0 ppm for the phantoms in the torso phantom at 1 cm depth are much lower than values previously reported. Comparing the current bare phantom result to the XRF feasibility study by Smith *et al.*[8] in which a 44 ppm MDL was obtained with a ^{57}Co source and an 85° detection geometry, there is an improvement by more than a factor of 11. The main reason for this improvement is the use of ^{109}Cd; the emitted 88.0 keV γ-rays are closer to the 83.1 keV K-edge of Hg than γ-rays emitted ^{57}Co (122.1 and 136.5 keV). Another improvement is the use of a larger detector and the inclusion of all the above-mentioned K x-rays in the analysis, as opposed to $K\alpha$ lines only.

In order to compare the results for kidney phantoms in the water tank to other studies, the effect of kidney depth on the MDL must first be taken into account. Figure 5 shows the MDL as a function of kidney depth, as measured from the tank boundary to the phantom boundary. As expected, there is a profound effect on Hg sensitivity due to the attenuation of both incident γ-rays and emitted x-rays as the depth increases. For *in vivo* studies, the depth of the patient's kidney would be measured via ultrasound such that the appropriate MDL can be applied in the measurement.

Table 1. Individual and total MDL values for bare and water tank phantoms. The total MDL was calculated using Eqn (2)

MDL (ppm)	Bare phantoms (ppm)	Phantoms in water tank at 1 cm depth (ppm)
$K\alpha_1$ and $K\alpha_2$	9.0	14.3
$K\beta_1$ and $K\beta_3$	4.6	5.7
$K\beta_{2'}$, $K\beta_{2''}$ and $KO_{2,3}$	12.0	14.2
Coherent peak	72.7	91.7
Total	3.9	5.0

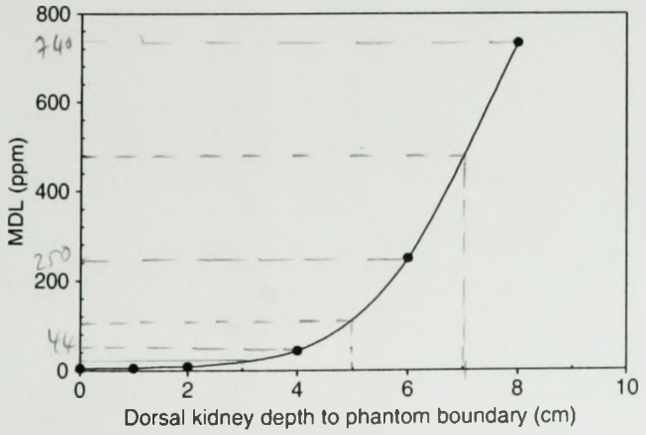

Figure 5. . Variation of MDL as a function of kidney depth, as measured from inside water tank boundary to the organ boundary (tank wall thickness is 0.3 cm; therefore at 0 cm dorsal kidney depth, the actual depth is 0.3 cm). As expected, the MDL increases rapidly with depth.

It is difficult to compare the results of the present study to the polarized XRF study by Börjesson *et al.*,[3] as the depth of the kidney was not specified for the detection limit of 25 ppm for a 50 min measurement. In addition, because of the 90° detection geometry, both the lateral and dorsal kidney depths have to be accounted for as opposed to just the dorsal depth for the 180° detection geometry. Also, using polarized XRF, O'Meara *et al.*[9] reported an MDL of 26 ppm for 2 cm lateral, 5 cm dorsal depth and 54 ppm for a 6 cm lateral, 5 cm dorsal depth, both for a 30 min live time measurement and 8 mSv skin dose. In comparison, the current MDL is 8.4 ppm at 2 cm kidney depth and 44 ppm at 4 cm depth (Fig. 5), although a simple comparison is not possible because of the additional depth parameter in polarized XRF studies. The MDL values in the current study are comparable to polarized XRF for a given kidney depth. However, a much lower skin dose rate would be delivered during a source-excited XRF *in vivo* measurement; the skin dose is expected to be approximately 1.6 mSv. With forthcoming improvements to the source-excited XRF system, the MDL is expected to be appreciably lower than with polarized XRF, for a lower measurement dose.

Future improvements to the source-excited XRF system at McMaster will involve the use of a cloverleaf HPGe detector, which consists of four electronically separate detectors, each having a 16 mm diameter and 10 mm thickness. Source strength will be appropriately increased from about 1 GBq to 10 GBq. Source strength is an important limiting factor in the large-area single detector system due to the amount of signal that can be processed by the electronics. Since four smaller electronically separate detectors will be used, the source strength can be increased significantly. In addition, the cloverleaf system has a better resolution (about 450 eV *vs* 750 eV at 88.0 keV for the single detector), and therefore less background will be present under peaks of interest, reducing the MDL further (Eqn (1)). The MDL is expected to improve by more than a factor of 2 with the cloverleaf system compared to the MDL obtained with the single detector system.[16]

CONCLUSIONS

A ^{109}Cd-based source-excited XRF system for the detection of Hg in the kidney has been developed such that future measurements of kidney Hg *in vivo* may be possible in order to prevent adverse health effects in occupationally exposed individuals. Feasibility measurements with bare kidney phantoms yielded an MDL value of 3.9 ppm, which is more than a factor of 11 better than previous source-excited measurements with ^{57}Co.[4] Kidney phantom measurements inside a water tank to simulate *in vivo* measurements were performed and the MDL was found to be 5.0 ppm at 1 cm kidney depth, measured to the phantom boundary. This result is lower than previous polarized XRF studies;[3,5] however, the MDL increases significantly with kidney depth

X-Ray Spectrom. 2007; **36**: 99–103
DOI: 10.1002/xrs

because of attenuation of incident and emitted photons. Further improvements to the source-based XRF system will include the use of a cloverleaf HPGe detector composed of four separate detector crystals and increasing the ^{109}Cd source strength. This will result in more than a factor of 2 improvement in MDL. Additionally, dosimetry will be performed to determine the dose to a patient during any future *in vivo* measurements, once the MDL is sufficiently low for these measurements to be possible.

REFERENCES

1. Clarkson TW, Magos L. *Crit. Rev. Toxicol.* 2006; **36**: 609.
2. World Health Organisation. *Environmental Health Criteria No. 118: Inorganic Mercury*. World Health Organization: Geneva, 1991.
3. Börjesson J, Barregård L, Sällsten G, Schütz A, Jonson R, Aplsten M, Mattsson S. *Phys. Med. Biol.* 1995; **40**: 413.
4. Barregård L, Sällsten G, Conradi N. *Int. Arch. Occup. Environ. Health* 1999; **72**: 169.
5. Barregård L, Svalander C, Schütz A, Westberg G, Sällsten G, Blohme I, Mölne J, Attman P-O, Haglind P. *Environ. Health Perspect.* 1999; **107**: 867.
6. Börjesson J, Mattsson S, Aplsten M. *Appl. Radiat. Isot.* 1998; **49**: 437.
7. El-Sherbeeny AM, Odom JV, Smith JE. *Cutan. Ocul. Toxicol.* 2006; **25**: 173.
8. Smith JRH, Athwal SS, Chettle DR, Scott MC. *Int. J. Appl. Radiat. Isot.* 1982; **33**: 557.
9. O'Meara JM, Börjesson J, Chettle DR. *Appl. Radiat. Isot.* 2000; **53**: 639.
10. Grinyer J, Byun SH, Chettle DR. *Appl. Radiat. Isot.* 2005; **63**: 475.
11. Grinyer J, Byun SH, Chettle DR. In *8th International Conference on Nuclear Analytical Methods in the Life Sciences (NAMLS8) Book of Abstracts*. Riode Janeiro, Brazil, 2005.
12. Grinyer J, Atanackovic J, Byun SH, Chettle DR. *Nucl. Instrum. Methods Phys. Res., Sect. B* (in press).
13. Press WH, Teukolsky SA, Vetterling WT, Flannery BP. *Numerical Recipes in C* (2nd edn). Cambridge University Press: Cambridge, 1992.
14. Chettle DR, Franklin DM, Guthrie CJG, Scott MC, Somervaille LJ. *Biol. Trace Elem. Res.* 1987; **13**: 191.
15. Börjesson J, Alpsten M, Huang S, Jonson R, Mattsson S, Thornberg C. In *Human Body Compostion*, Ellis KJ, Eastman JD (eds). Plenum Press: New York, 1993.
16. Nie H, Chettle DR, Luo L, O'Meara J. *Phys. Med. Biol.* 2006; **51**: 351.

X-Ray Spectrom. 2007, **36**: 99–103
DOI: 10.1002/xrs

Chapter 5

X-ray Fluorescence with the Cloverleaf Detection System

In order to improve the minimum detection limit of mercury using source-excited x-ray fluorescence, a cloverleaf detection system, previously used to detect lead in bone (Nie, 2005), was investigated. This system allowed a factor of 2 reduction in the detection limit of lead in bone over a planar detection system, and a similar improvement was expected in kidney mercury detection. In this chapter, the new cloverleaf system was used to perform a feasibility study using bare kidney phantoms, and based on the improvement observed was then used to measure kidney phantoms within a torso phantom. The results of the torso phantom study yielded comparable results to those of the planar detection system, and did not improve the minimum detection limit as expected. In addition, the feasibility of performing *in vivo* measurements was tested by measuring several body sites, including the kidney, of two patients with possible exposure to mercury.

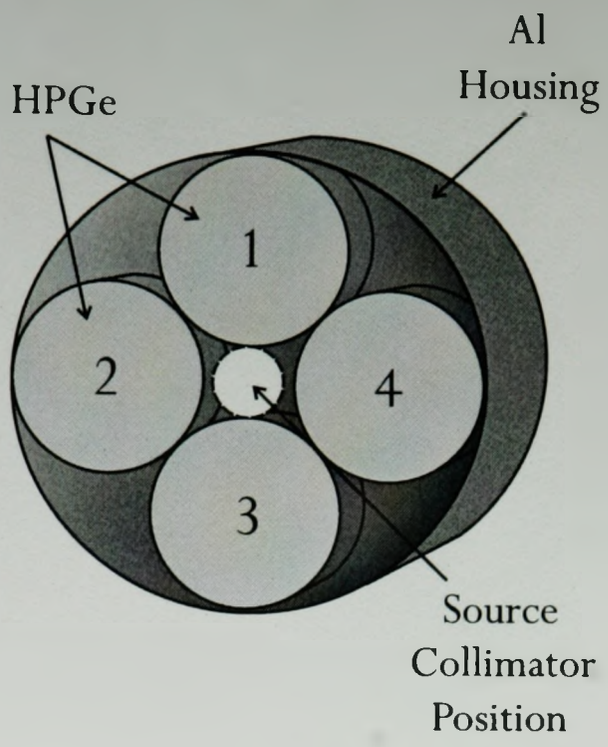

Figure 5.1: Schematic of the four detector crystals comprising the cloverleaf detector. Each crystal has a 16 mm diameter and 10 mm thickness.

5.1 Cloverleaf detection system

The cloverleaf detector consists of four electronically separate HPGe detectors, each having a 16 mm diameter and 10 mm thickness (see Figure 5.1), with four independent sets of electronics. The detector crystals are housed in a single detector unit with a 0.5 mm thick aluminum window, and a 5 mm crystal-to-window distance. Each detector has its own pre-amplifier, and the high voltage to all four detectors is supplied by one of four DSA-1000 digital multichannel spectrum analyzers (Canberra). Signals from each detector are collected and processed by a separate DSA-1000, and spectra are collected with a Windows-compatible Genie-2000 software (Canberra). Spectra from each detector are displayed in a separate graphics window and can be saved for offline analysis. Each of the four spectra are analyzed independently with the Levenberg-Marquart fitting algorithm as discussed in Chapter 1 of this thesis (Section 1.5.5).

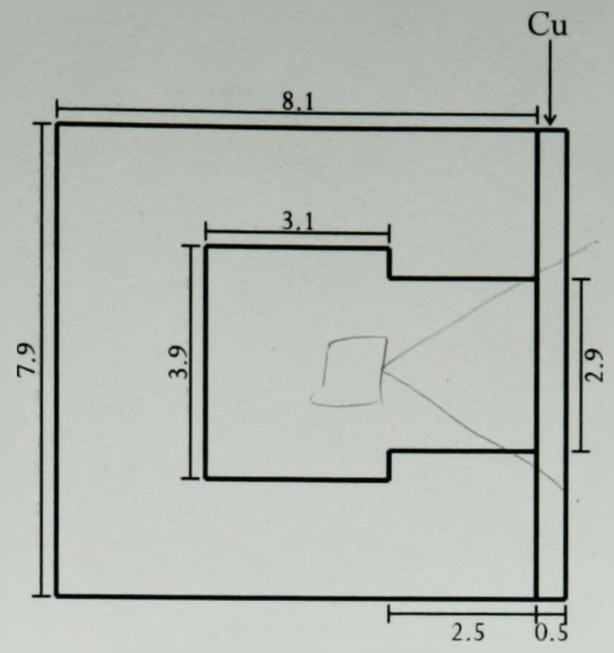

Figure 5.2: Source collimator for the cloverleaf detection system (dimensions in mm, to scale).

For the cloverleaf system, an 8 GBq (original strength of 10 GBq, November 2005) ^{109}Cd source was used as opposed to the 0.25 GBq that was used with the planar system (see Chapter 4). Since four smaller electronically separate detectors are used, the cloverleaf system can handle a stronger source than the planar detector system. The source is encapsulated within a 3 mm by 3 mm cylindrical titanium shell that fits within a tungsten source collimator. The source collimator housing the new source is shown to scale in Figure 5.2. The kidney and torso phantoms had the same dimensions as shown in Figure 1 of Chapter 4.

5.2 Feasibility experiments with the cloverleaf detection system

Bare kidney phantoms filled with mercury solutions ranging in concentration from 0 to 500 ppm were placed 8 mm away from the source collimator exit. Spectra were

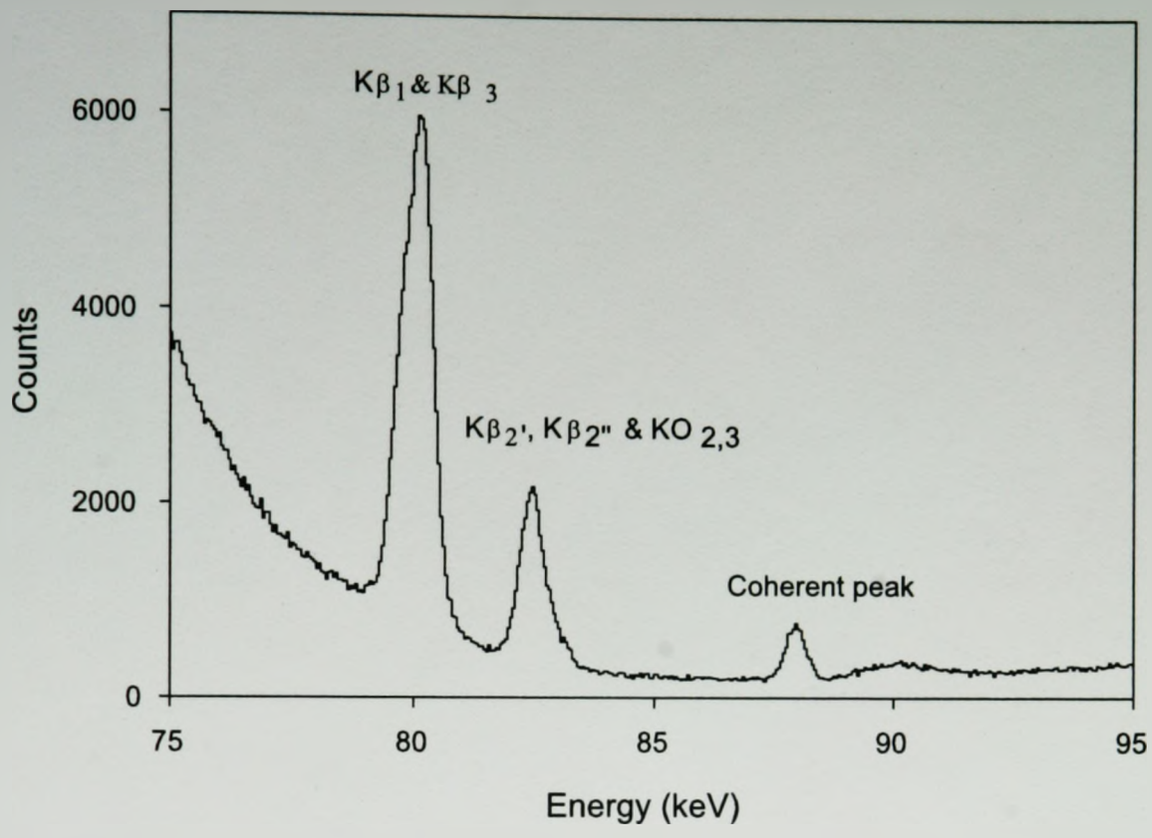

Figure 5.3: Bare phantom spectrum collected with a 500 ppm kidney phantom.

collected for 1800 s real time, and analyzed to extract K x-ray peak areas as described in Section 1.5.5. A sample bare phantom spectrum is shown in Figure 5.3.

The MDL was calculated from the slope of the calibration line that was plotted for each fitted peak and each detector. The results for each peak and detector are listed in Table 5.1.

By combining the individual MDLs (see Equation 2, Chapter 4), a final mercury detection limit of 0.7 ppm was obtained using the bare phantoms. This represents more than a factor of 5 improvement over the planar detection system result of 3.9 ppm. Although the experimental parameters are slightly different in both systems (for example sample-to-source distance and spectrum collection time), the improvement is significant. Based on the positive outcome of the feasibility study,

Table 5.1: MDL values obtained with the cloverleaf detection system and bare kidney phantom.

	MDL ($K_{\beta 1}$) (ppm)	MDL ($K_{\beta 2'}$) (ppm)	MDL ($K_{\alpha 1}$) (ppm)	MDL (coherent) (ppm)
Detector 1	1.8	4.2	3.0	29.3
Detector 2	1.7	3.9	2.8	25.6
Detector 3	1.8	4.1	2.9	28.3
Detector 4	1.8	4.2	3.0	25.6
Total	0.9	2.0	1.5	13.5
Final MDL		0.7 ppm		

torso phantom experiments were carried out to determine the MDL.

5.3 Experiments with the torso phantom

Initial experiments with the cloverleaf detector and the torso phantom (see Figure 1, Chapter 4) yielded a lower peak-to-background ratio compared to those for the planar detector. For example, the $K_{\beta 1}$ peak-to-background ratio for a 500 ppm kidney phantom at 1 cm depth in the torso phantom was 55 for a single cloverleaf detector compared to 96 for the planar detector. Although these values were obtained under slightly different experimental conditions, the peak-to-background ratio was consistently lower than expected for the cloverleaf detector. The MDL from initial calibration measurements with the cloverleaf system was 5.2 ppm when all mercury K x-rays and detectors were included, which is virtually equivalent to the MDL of 5.0 ppm obtained with the planar detector system. Compared with bare phantom studies that yielded a factor of 5 improvement in the MDL, no improvement was

observed in the torso phantom studies.

The cloverleaf system spectrum with the torso phantom includes significantly more background in the vicinity of the mercury K x-rays (see Figure 5.4). Compared with the bare phantom spectrum, the major difference is the increase in area of the Compton scatter peak as well as the addition of a large amount of background due to the pile up of Compton gamma-rays which extends continuously up to $\sim$ 132 keV. Both of these features significantly increase the background present under the mercury K x-rays. Figure 5.5 shows the mercury K_β x-rays and the coherent gamma-ray for both the bare and torso phantoms. Comparison of these two spectra demonstrate that the K_β peaks from the torso phantom are dramatically smaller, leading to a decreased sensitivity. Since $K_{\beta 1}$ and $K_{\beta 3}$ peaks contribute most to lowering the MDL, and because the background under these peaks is increased slightly due to Compton scatter and pile up effects due to increased source strength (although significant increase in background can be observed at energies greater than 83 keV), no significant improvement to the mercury kidney MDL could be determined.

Two main reasons for the increase in the background level from Compton scattering and pile-up processes is the use of the increased source strength (8 GBq *vs.* 0.25 GBq for the planar system) and the presence of a water tank which acts as an infinite scattering medium. In order to maximize the peak-to-background ratio and therefore minimize the MDL, several attempts were made to improve the cloverleaf detection system for the purpose of mercury kidney detection.

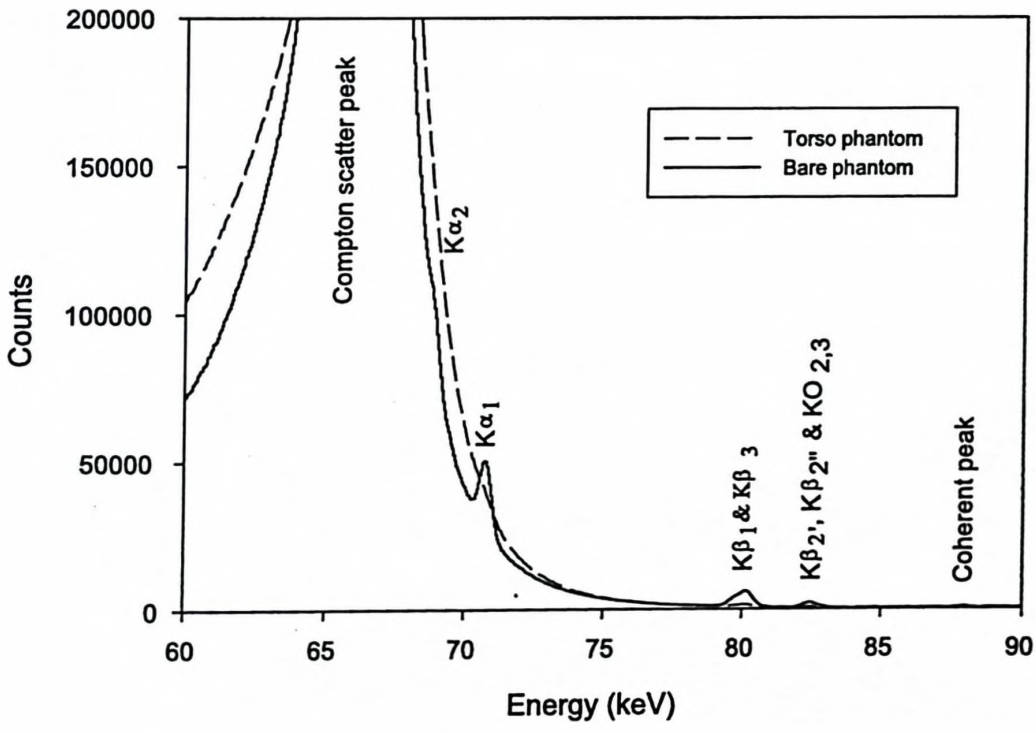

Figure 5.4: Comparison of bare and torso phantom spectra for the cloverleaf system collected with a 500 ppm kidney phantom. Mercury x-rays are not clearly visible in the torso spectrum on this scale.

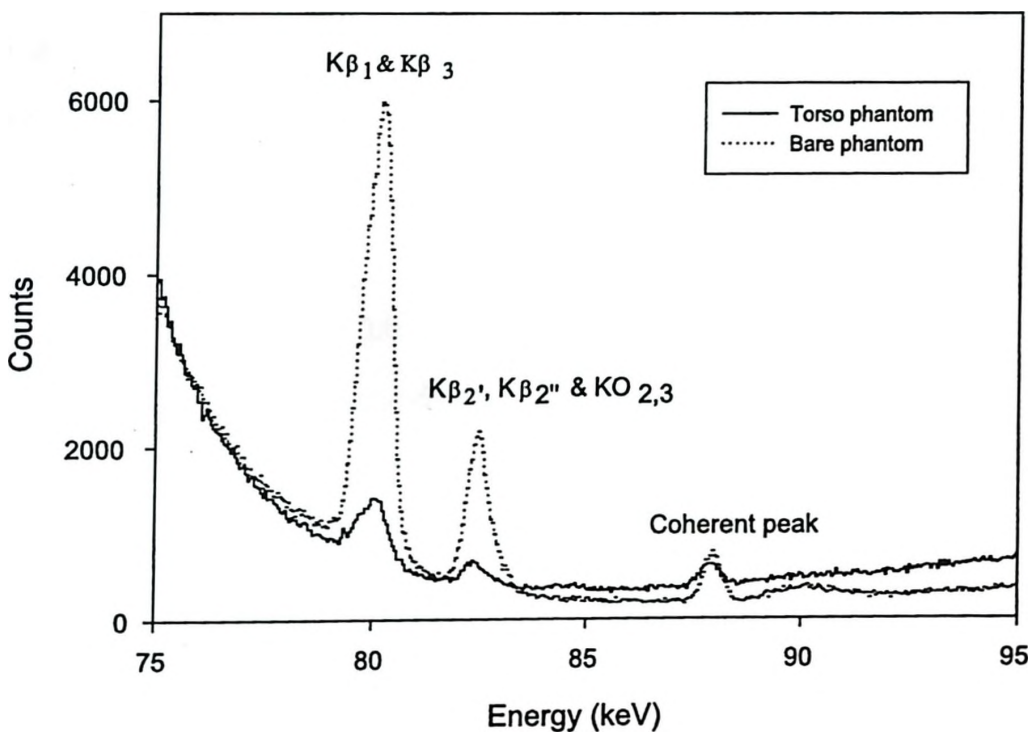

Figure 5.5: Torso phantom spectrum compared with the bare phantom spectrum in the vicinity of the K_β photopeaks, collected with a 500 ppm kidney phantom.

5.3.1 Improvement to the cloverleaf detection system

In order to reduce the background under the mercury K x-rays for the torso phantom studies, the optimal signal shaping time had to be determined. Shaping time is changed in the Genie-2000 interface by varying the rise and flat top times. Although using longer rise time and flat top time settings is desirable in terms of improved energy resolution and reduced background, this leads to larger detector deadtime and reduced peak-to-background ratios. It is not reasonable to operate the system with deadtimes exceeding 40%, and settings as low as rise time of 1.6 μs and flat top of 0.6 μs (settings used to obtain a MDL of 5.2 ppm above) yielded this level of deadtime. In order to find the optimal settings, lower values of rise time and flat top time were investigated. From Table 5.2, the optimal peak-to-background ratios were obtained with a rise time of 1.0 μs and flat top time of 0.4 μs, however, the values were relatively insensitive to the changes in rise and flat top times.

The presence of background due to detector pulse pile-up significantly reduces the system's sensitivity. The Genie-2000 software allows limited control of the pile-up rejection (PUR) settings. The user can turn off PUR, keep the default setting of 1.1x, or increase the PUR setting in 0.2 increments between 1.1x and 2.5x. These settings are arbitrary, however the influence of these PUR settings on the spectrum was investigated. Turning off PUR results in a very high background level while the default and lowest setting of 1.1x reduces the background significantly (see Figure 5.6). The maximum setting of 2.5x reduces the background further, however it also leads to a large amount of good events (in this case mercury K_β x-rays) being rejected (see Figure 5.7). Intermediate settings between the two extrema of 1.1x and 2.5x were investigated, however the optimal PUR setting was determined to be 1.1x as this gave the highest peak-to-background ratio for mercury K x-rays.

Table 5.2: Comparison of resolution and peak-to-background (P/B) ratios (2500 ppm phantom at 0 cm depth in the torso phantom). The setting of 1.0 μs rise time and 0.4 μs flat top gave the best sensitivity and was used for further experiments with cloverleaf detection system. Data obtained with 1.6 μs rise time and 0.6 μs are not included in this table as they were collected at a different tank position, and are not directly comparable.

	0.6 μs rise time/0.3 μs flat top	0.8 μs rise time/0.4 μs flat top
Deadtime (%)	12	15
FWHM (88 keV)	598	556
$K_{\beta 1}$ area	85258.8 $\pm$ 296.8	82027.1 $\pm$ 285.0
$K_{\beta 1}$ P/B	287.3	287.8
$K_{\beta 2'}$ area	20123.3 $\pm$ 146.1	19832.2 $\pm$ 140.6
$K_{\beta 2'}$ P/B	137.7	141.1
$K_{\alpha 1}$ area	382912.7 $\pm$ 1236.3	367710.1 $\pm$ 1158.4
$K_{\alpha 1}$ P/B	309.7	317.4
	1.0 μs rise time/0.4 μs flat top	1.2 μs rise time/0.5 μs flat top
Deadtime (%)	18	21
FWHM (88 keV)	555	514
$K_{\beta 1}$ area	80539.4 $\pm$ 279.1	76203.6 $\pm$ 275.0
$K_{\beta 1}$ P/B	288.6	277.1
$K_{\beta 2'}$ area	19339.7 $\pm$ 137.1	18415.4 $\pm$ 134.9
$K_{\beta 2'}$ P/B	141.1	136.5
$K_{\alpha 1}$ area	367728.0 $\pm$ 1141.7	340536.9 $\pm$ 1070.0
$K_{\alpha 1}$ P/B	322.1	318.3

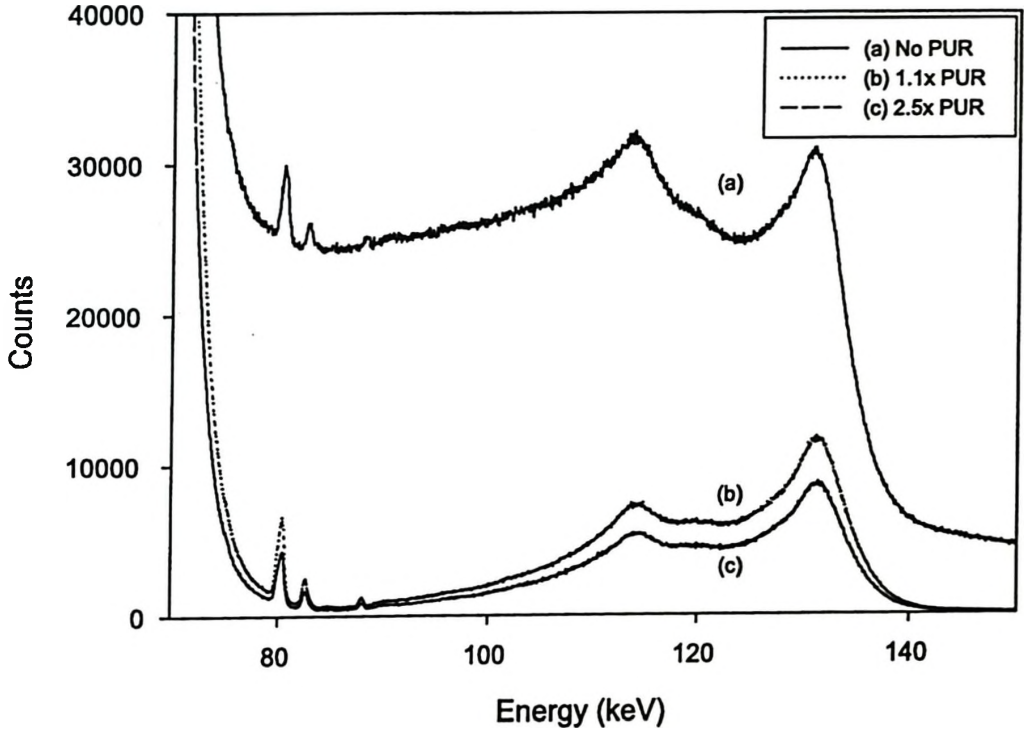

Figure 5.6: Comparison of pile-up rejection (PUR) settings in Genie-2000 software. Spectra were obtained with settings of 1.0 μs rise time and 0.4 μs flat top.

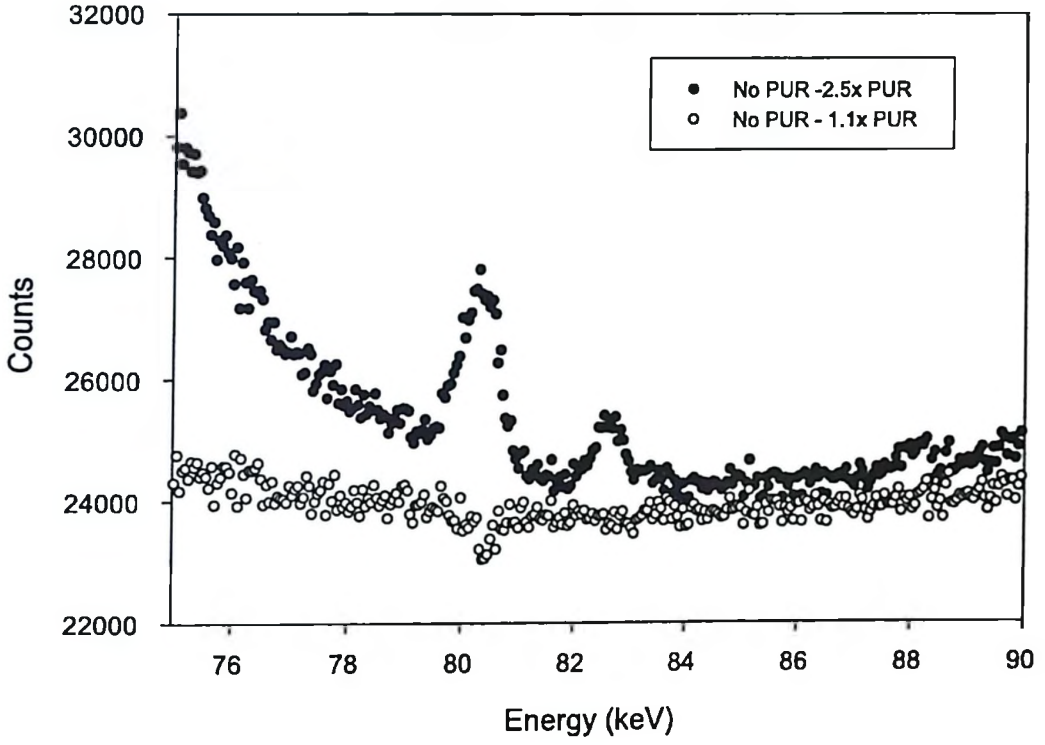

Figure 5.7: Subtracted counts remaining after the subtraction of spectra with PUR turned off and setting of 1.1x, and of PUR turned off and setting of 2.5x. The PUR setting of 2.5x results in rejection of K_β x-rays.

Another consideration in reducing the background is the source strength. The source used for both bare phantom and torso phantom experiments was 8 GBq. A weaker source was available with a 1 GBq strength, and a sample calibration was performed to see if there would be improvement in the MDL. Due to a lower deadtime, longer settings of rise time of 5.6 μs and flat top of 0.8 μs were used thereby improving the energy resolution of mercury K x-rays. Despite a better resolution, the MDL calculated from all four HPGe detector crystals was 6.9 ppm. Although this was higher than the initial MDL of 5.2 ppm using the stronger 8 GBq source, it is anticipated that only a moderate improvement could be obtained with an intermediate source strength.

A large and complex background such as the one present in the torso phantom spectra is difficult to describe when trying to find an appropriate fit function. The fit functions used to fit mercury K x-rays are described in detail in Section 1.5.5, however these fit functions did not give reasonable fits for the torso phantom spectra. Namely, the fits overestimated the background and as a result the calibration line intercept was not zero despite having a good overall reduced χ^2. As this overestimation was relatively uniform for all phantom concentrations, the slope of the calibration line and hence the MDL were not largely affected. However, when trying to determine the mercury concentration in *in vivo* measurements (see Section 5.4.1) this becomes an issue. Attempts at modifying the fit function were investigated including fitting a double exponential background under the K_β peaks, fitting all of the K_β and $KO_{2,3}$ peaks together, including a decreasing exponential background on the lower energy side of a peak and an increasing exponential background on the upper energy side. All of these fitting procedures resulted in either an increased overestimation or underestimation of the background or did not converge in the fitting program due to

infinite covariance between fitted parameters. Overall, the best result was achieved with the original fit functions of Section 1.5.5, and an alternate fit function could not be found. It should be emphasized that while the fit function used here is not entirely optimal, this is not significant when extracting the slope and hence the MDL from the calibration. Further improvements to the cloverleaf detection system should yield a lower background, hence improving the quality of the fit to data (see Section 5.5).

5.3.2 Calibration measurements and detection limit

Using the optimized settings (rise time of 1.0 μs, flat top of 0.4 μs, PUR of 1.1x), the final kidney phantom calibration was performed with mercury concentrations ranging from 0 to 500 ppm. These were placed at a 1 cm depth in the torso phantom, and the torso phantom was placed 4 mm from the collimator exit. Spectra were collected for 1800 s real time. Using the same data analysis procedure described in Section 5.2, MDL values for each detector and K x-ray peak were calculated (see Table 5.3).

Table 5.3: MDL values obtained with the cloverleaf detection system and kidney phantom within the torso phantom.

	MDL ($K_{\beta 1}$) (ppm)	MDL ($K_{\beta 2'}$) (ppm)	MDL ($K_{\alpha 1}$) (ppm)	MDL (coherent) (ppm)
Detector 1	13.2	33.4	29.0	341.8
Detector 2	12.3	34.9	26.3	236.9
Detector 3	13.5	36.1	24.2	218.9
Detector 4	12.4	34.9	23.8	206.9
Total	6.4	17.4	12.8	119.0
Final MDL		5.4 ppm		

By combining the individual results using Equation 3, Chapter 4, the final MDL of 5.4 ppm with the kidney phantom at 1 cm depth in the torso phantom was obtained. This value is comparable to the initial MDL of 5.2 ppm. This insignificant difference is due to small phantom position changes that can cancel out the improvement gained by adjusting the rise time and flat top. This result suggests, however, that the overall system is not sensitive to slight changes in shaping time and other experimental parameters such as phantom position, which is very important in *in vivo* measurements (see Section 5.4). Therefore, the initial settings were sufficient in obtaining a good sensitivity providing the deadtime fraction was kept below 40%.

The dependence of MDL on kidney depth was also measured by immersing the 500 ppm kidney phantom at various depths, collecting the spectrum and extracting the MDL for each depth following the adopted spectral analysis procedure described above. The kidney phantom position dependence is shown in Figure 5.8. As expected, the MDL increases rapidly with kidney depth. Therefore, the current system's mercury sensitivity is relatively low for persons with deep-lying kidneys.

Despite attempts at improving the sensitivity of the cloverleaf system, the final MDL (ranging from 5.2 to 5.4 ppm) was comparable to that of the planar system (5.0 ppm). The cloverleaf system did not improve the MDL as anticipated based on initial bare phantom experiments, mostly due to increased background under the mercury K x-rays. Suggestions for future improvement of the cloverleaf system are described in Section 5.5.

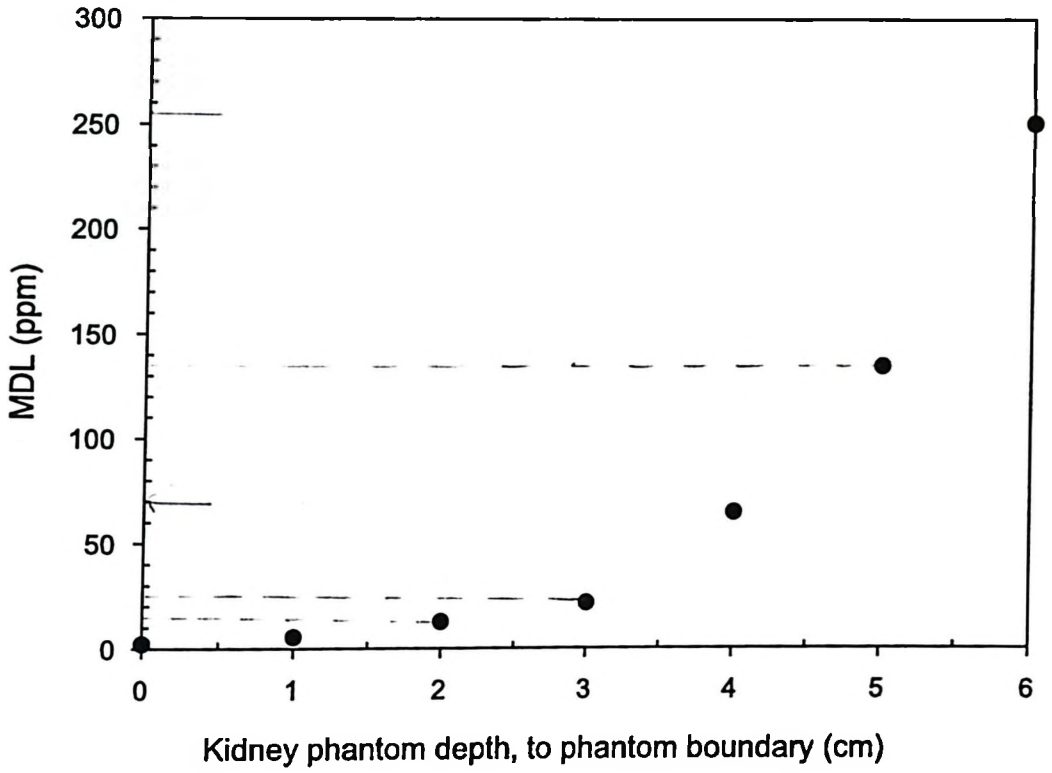

Figure 5.8: Dependence of MDL on 2500 ppm kidney phantom position for the clover-leaf system. Phantom depth is measured to the phantom boundary.

5.4 *In vivo* measurements

The Occupational Nuclear Medicine Research Group at McMaster University was contacted by two individuals regarding non-invasive measurements of mercury body burdens. Both patients believed they had been exposed to mercury in the past and are now suffering or did suffer from related health symptoms. In order to measure mercury levels in the organs of interest, ultrasounds were scheduled to determine tissue thicknesses overlying the left kidney. In each case, the kidney, the liver, and additional sites where the patients believed they may have mercury stores, were measured. The cloverleaf detection system along with the 8 GBq ^{109}Cd source was used to measure mercury burdens in each patient using the previously described technique (Section 5.3.1). Although the MDL results were approximately the same (5 ppm at 1 cm depth), the cloverleaf system was chosen over the planar system due to the fact that several components of the planar system were not in place at the time of the requested measurements. Both patients were measured in April of 2007.

5.4.1 Patient 1

Patient 1 was a 66 year-old male with a history of occupational exposure in a 90-day period between 1964 and 1965. The patient was exposed to mercury from skin contact and vapours when moving, what he referred to as, chloroalkali cells. He has a history of mood disturbances and psychological problems that he believes are related to his mercury exposure history. In 2006, he was evaluated by a neuropsychologist that found he was normal to above normal in various cognitive and motor functioning skills. The physician did not find any evidence of memory loss, spatial perception or mood symptoms that may accompany mercury exposure, however, the patient

has a history of mood symptoms, personality changes, and psychotic episodes that immediately followed his mercury exposure. The patient's major physical ailments include emphysema (patient smokes more than 1 pack of cigarettes per day) and skin cancer.

As an ultrasound could not be performed, the XRF measurement began without the tissue thickness evaluation. Based on the patient's physical size, the tissue thickness overlying the kidney could have been approximately 4 cm. In addition to the kidney, the patient believed other sites that may have mercury stores were the temple and two abdominal sites: the diaphragm and liver areas. Therefore a total of 4 measurements were performed, each lasting 1800 s real time. The spectra were saved and analyzed to determine the concentration of mercury. A kidney spectrum for Patient 1 is shown in Figure 5.9. Since only a proper calibration was carried out with kidney phantoms (so that an estimate could be made based on the approximate kidney depth), other sites only yielded a concentration that could not be reliably corrected for depth. In the case of the liver, a 2 cm depth was assumed and the concentration was corrected for depth based on the kidney depth data (see Figure 5.8).

As discussed in Section 5.3.1, the intercept of the calibration line was not zero, which affected the conversion of the fitted peak area to the overall mercury concentration for *in vivo* measurements. The negative intercept due to overestimation of the background by the fit function therefore was treated as a source of systematic uncertainty. In order to estimate this systematic uncertainty, the calibration intercept was assumed to be zero, and the slope was calculated independent of the intercept. Thus, the uncertainty on the mercury concentration included both the statistical uncertainty from the fit procedure and the estimated systematic uncertainty combined in quadrature. The final results for Patient 1 are listed in Table 5.4.

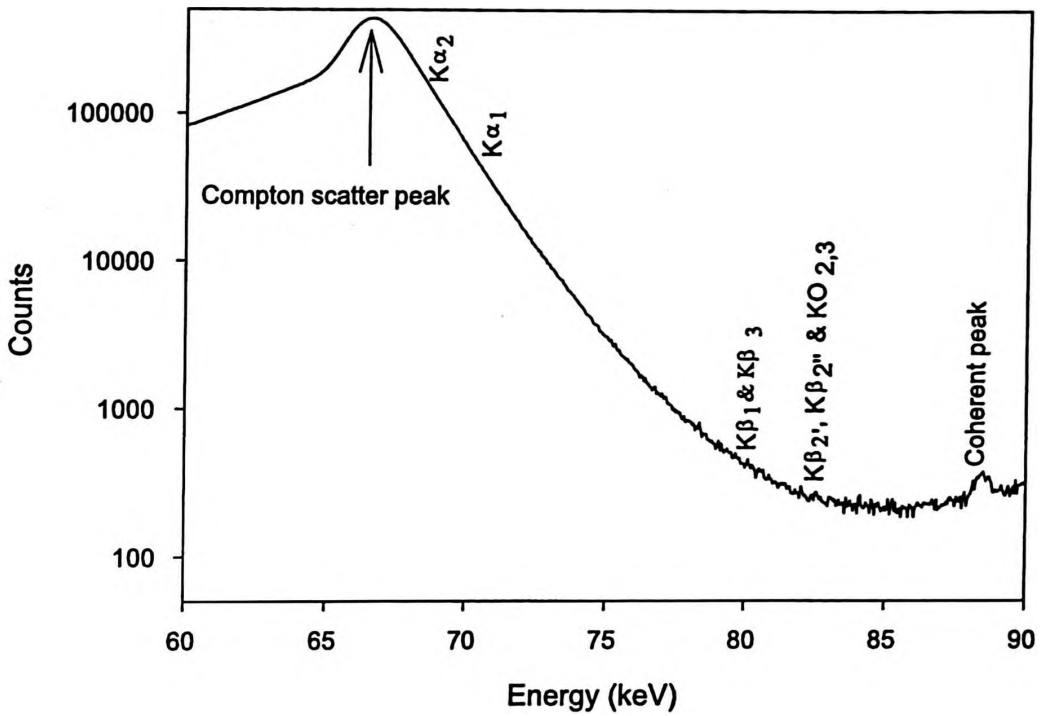

Figure 5.9: A kidney spectrum for Patient 1 collected for 1800 s. The possible positions of mercury x-ray photopeaks are marked ("Counts" are plotted on a log scale).

In order to correct for organ depth in the case of kidney and liver, an appropriate scaling factor was applied to the final result. Since the patient did not have an ultrasound measurement, a rough estimate of organ depth was made. Assuming a 4 cm kidney depth, the scaling factor was 12.8 based on kidney phantom depth measurements (see Figure 5.8), therefore the depth-adjusted result for the kidney was -47.4 $\pm$ 34.6 ppm. Assuming a 2 cm liver depth, the scaling factor was 2.4, therefore the adjusted liver result was -0.7 $\pm$ 11.2 ppm.

None of the measurement sites give a result that exceeds the individual minimum detection limit (MDL as twice the uncertainty in the background). The inclusion of the systematic uncertainty is somewhat conservative, and the temple measurement

Table 5.4: Mercury measurement results for Patient 1 (uncertainty on the measurement is one standard deviation).

Measurement site	Concentration (ppm)	Statistical uncertainty (ppm)	Systematic uncertainty (ppm)	Final result (ppm)	Corrected concentration (ppm)
Kidney	-3.7	2.6	9.5	-3.7 ± 9.8	-47.4 ± 34.6
Liver	-0.3	2.5	9.4	-0.3 ± 9.7	-0.7 ± 11.2
Diaphragm	1.9	2.5	9.1	1.9 ± 9.4	-
Temple	10.9	2.8	9.7	10.9 ± 10.1	-

showed some weak evidence that the temple did indeed have detectable mercury, although it was not quantifiable since a calibration was not performed for the temple site. An exact "less than" figure cannot be given for the organ sites due to the fact that depth measurements were not performed. Based on the estimated kidney and liver depth, Patient 1 had less than 69 ppm of mercury in the kidney and less than 22 ppm of mercury in the liver. Phantom calibrations were not performed for the other two measurement sites, therefore a concentration cannot be given. However, Patient 1 had no detectable mercury in any of the sites measured including the kidney, except possibly at the temple site. This may or may not be due to the relatively low sensitivity of the system, long period of time between exposure and measurement, or large attenuation by the bone in the temple region.

5.4.2 Patient 2

Patient 2 was a 60 year-old female who had a dental mercury amalgam filling in 1998. Shortly after the filling, she experienced symptoms such as dizziness, double vision, drooping eyelids, and difficulty walking. Doctors diagnosed her with multiple

sclerosis, however, she did not believe the diagnosis and came across other individuals that allegedly had similar reactions to amalgam dental fillings. After the removal of the dental filling, she ceased to experience the above symptoms. Scientifically, no evidence has been found that mercury amalgams can cause such a reaction although there is circumstantial evidence of such an "allergic" reaction (Magos and Clark, 2006).

An ultrasound was performed on Patient 2 and the kidney depth and liver were measured to be 1.7 cm and 2.3 cm, respectively. Both the liver and left kidney were measured with the cloverleaf system, in addition to the tibia and temple as requested by Patient 2. A total of 4 measurements, each lasting 1800 s real time, were performed. The data were analyzed to determine the mercury concentration in each measurement site, and a systematic uncertainty was estimated as described in Section 5.4.1. Results of the measurements are listed in Table 5.5.

Table 5.5: Mercury measurement results for Patient 2 (uncertainty on the measurement is one standard deviation)

Measurement site	Concentration (ppm)	Statistical uncertainty (ppm)	Systematic uncertainty (ppm)	Final result (ppm)	Corrected concentration (ppm)
Kidney	3.4	2.7	8.7	3.4 ± 9.1	8.2 ± 10.8
Liver	6.1	2.4	9.4	6.1 ± 9.7	14.6 ± 11.0
Tibia	4.4	2.9	9.0	4.4 ± 9.5	-
Temple	-19.5	3.1	12.6	-19.5 ± 12.9	-

The kidney and liver measurements were corrected for depth. The depth was assumed to be 2 cm for each organ and the scaling factor for this depth was 2.4. The exact ultrasound depth measurements were approximated as 2 cm since data

were available for this depth from the phantom measurements. The uncertainty in the exact positioning of the patient in front of the cloverleaf detector for the XRF measurement means that the ultrasound depth measurement is only a guide. In this case, the corrected concentration for the kidney was 8.2 ± 10.8 ppm, and for the liver it was 14.6 ± 11.0 ppm. Based on these depth corrections, Patient 2 had less than 22 ppm of mercury in the kidney and less than 22 ppm in the liver. Since a calibration was not performed for the other two measurement sites, the concentrations could not be specified and can only be reported in terms of no detectable mercury. These results can be interpreted as either the current sensitivity of the system is too low, Patient 2 did not have mercury exposure related to her dental filling, or that there are no elevated mercury levels in any of the sites measured. In addition, the time period between measurement and exposure was almost 9 years, which may have contributed to no mercury being detected if in fact exposure to mercury took place.

5.5 Future improvements of cloverleaf system

The cloverleaf detection system for torso phantom studies was comparable to the planar detection system described in Chapter 4, despite an anticipated improvement based on bare phantom measurements. This is primarily due to the high background present under mercury K x-rays. Therefore, the key to improving the cloverleaf system for use with the torso phantom and for *in vivo* measurements is to reduce the background, and initial attempts at modifying the shaping time and pile-up rejection settings did not result in a significant improvement to the MDL. In fact, these initial optimization studies showed that the system was not sensitive to slight changes in the electronics pulse shaping times and positioning of the phantoms. For *in vivo*

measurements, this is critical for the positioning of the patients.

In order to reduce the background further, an extensive simulation study needs to be performed to determine the optimal source strength and collimator length. The present collimator length of 2.5 mm, with a 0.5 mm thick copper filter (see Figure 5.2), is relatively short. As a result, the solid angle of the beam may be too large to sample the kidney effectively. This would result in unnecessary background signals from the surrounding water of the torso phantom, leading to the elevated background observed. By optimizing the collimator length, the background due to Compton scattering and pile-up effects would be greatly reduced, which would lead to a significant reduction in the MDL. Furthermore, with a reduction in the background, the quality of fit to the data will be improved, thereby giving a more reliable peak area for each concentration and ensuring that the intercept is zero. As the dominant source of uncertainty in the *in vivo* measurements described here was due to the systematic effect of a non-zero intercept, improving the overall fit to the data can reduce the MDL further. In addition, the current source strength of 8 GBq may be too strong for the system. Although it was shown that a 1 GBq source resulted in virtually no change versus the 8 GBq source, intermediate source strengths need to be investigated. Several source strengths should be simulated, either by varying the thickness of the copper filter or the original source activity that can be purchased in the future. Additional general improvements to the XRF method are discussed in Chapter 6.

Chapter 6

Conclusions

6.1 Discussion and thesis conclusions

There is a need for a non-invasive method of measuring cadmium and mercury organ burdens in order to aid in the prevention of adverse health effects in occupationally exposed individuals. Non-invasive monitoring methods currently used in the work-place involve blood or urine sampling, which may not reflect the total organ burden as they are heavily influenced by recent exposure. Invasive procedures such as biopsies are sometimes employed, however these carry risk to the patient and are not practical for use in routine monitoring of exposure. In this thesis, two non-invasive methods were developed for cadmium and mercury organ burden monitoring: prompt gamma neutron activation analysis (PGNAA) and source-excited x-ray fluorescence (XRF).

Initial research was carried out on the detection of cadmium in the liver and kidneys. The purpose of the work presented in Article I (Chapter 2) was to develop further an existing PGNAA system to lower the minimum detection limit (MDL) of cadmium. This system uses an isotopic neutron source, ^{238}Pu-Be, with a specially designed collimation and shielding apparatus. Prior to this work, the system MDL

was 3.8 mg of cadmium in the kidney (McNeill and Chettle, 1998). Several steps were taken to improve the sensitivity of the system and therefore lower the MDL. First, the optimal neutron source position within the collimator and shielding apparatus was determined. The source is movable and can be moved toward or away from the collimator exit (Figure 1, Chapter 2). By moving the source toward the exit of the collimator in 1 cm intervals, the optimal position was determined to be 6 cm closer to the collimator exit, relative to the original source position. At the 6 cm position, the MDL reaches a minimum while the dose rate increases past this position (see Figure 4, Chapter 2). A second improvement was to determine the optimal HPGe detector for use with the system. Initially, the system had two planar HPGe detectors with 51 mm diameter and 21 mm length. The planar detectors were the first to be tested since it was thought at the time that a thin detector would successfully detec the relatively low energy cadmium 559 keV gamma-ray, and reduce the Compton continuum under this peak thereby decreasing the MDL. When a comparison was made using a coaxial HPGe detector with 58 mm diameter and 57 mm thickness with 35% relative efficiency, the MDL was reduced by about 40% relative to a single planar detector. This was a dramatic improvement that showed the system sensitivity was largely dependent on the size of the germanium crystal in the detector and a thin planar detector did not improve the MDL as initially thought. A two-detector system was created with the addition of a secondary coaxial HPGe detector as shown in Figure 1 of Chapter 2, which further reduced the MDL by an additional 10%. The final improvement was to improve the phantom sizes and positions. The torso phantom position was optimized by measuring the best cadmium peak-to-background ratio at 559 keV and fixing this position relative to the source collimator exit. Also, the size of the liver phantom was increased from 1 L to 2 L to represent the true

liver size better; this step decreased the liver MDL by approximately 25%. The final MDLs after this extensive system optimization were 1.7 mg in the kidney and 3.3 ppm in the liver. These figures represent a more than factor of 2 improvement in the MDL for the kidney, and a factor of 1.4 improvement in the liver MDL. The present system at McMaster University currently has the best cadmium sensitivity in the world (Mattsson and Thomas, 2006), and can be utilized for future *in vivo* measurements.

As an extension to the *in vivo* PGNAA of cadmium, a feasibility study for the measurement of mercury in the kidney was made. Since the elemental thermal neutron capture cross-section of mercury is relatively high (372 b *vs.* 2500 b for cadmium), the optimized system was thought to be able to yield a low mercury MDL. However, the MDL was determined to be 315 ppm, which at the present time is too high for *in vivo* studies that require a MDL less than 10 ppm. The mercury MDL is 23 times worse than the cadmium MDL, although no more than a factor of 10 worse was expected based on several factors including the relative cross-sections Article II (Chapter 3) explains this apparent discrepancy by comparing both cadmium and mercury MDLs with chlorine, which is a well-known neutron activation element. By using the optimized PGNAA system and kidney phantoms containing known concentrations of cadmium, mercury and chlorine, a comparison was made in terms of sensitivity and MDL. First, the system was tested to see whether the measurement sensitivity scales with k_0, a calibration constant used for PGNAA. Once this was confirmed to be as expected, sensitivity ratios of cadmium to chlorine, mercury to chlorine and cadmium to mercury were compared. Cadmium gave a result that was a factor of 2 better than expected in terms of relative sensitivity and MDL of cadmium to chlorine and of cadmium to mercury, and is due primarily to the non-$1/\nu$ nature of

the cadmium thermal neutron capture cross-section and the non-thermal nature of the neutron beam from the ^{238}Pu-Be source (see Figure 1.1). This study also confirmed that the mercury to chlorine sensitivity and MDL ratios yielded results consistent with expectations. In fact, when a more thermalized neutron beam was used at the McMaster Nuclear Reactor thermal beam port, the MDL ratio was 15 instead of 23 with the ^{238}Pu-Be neutron source, and this was much closer to the expected factor of 10. Therefore, the sensitivity of cadmium is enhanced with the current PGNAA cadmium detection system due to the neutron energy spectrum of the ^{238}Pu-Be source, relative to that of mercury which is consistent based on comparisons with chlorine.

In order to improve the MDL of mercury further, an XRF feasibility study was investigated in detail. Previous XRF studies yielded better results than a MDL of 315 ppm obtained with PGNAA. Smith *et al.*, 1982, for example, obtained a MDL of 44 ppm for bare kidney phantoms with source-excited XRF with a ^{57}Co source. In addition, polarized XRF studies yielded an even lower MDL on the order of 25 ppm i the torso (Börjesson *et al.*, 1995, O'Meara *et al.*, 2000). However, all of these studies could not achieve a MDL of less than 10 ppm required for *in vivo* measurements of occupational exposure. Article III (Chapter 4) described the development of a source-based XRF system of mercury. In order to maximize the mercury fluorescence yield, a source has to have a photon energy that is slightly greater than the K-edge of mercury at 83.1 keV. A 0.25 GBq ^{109}Cd source whose gamma-ray energy is 88.0 keV was chosen, and a system comprising of a large surface area planar HPGe detector (50 mm diameter and 19 mm thickness), a DSA-2000 digital multichannel spectrum analyzer and pulse-processing system (Canberra), source collimator, and torso and kidney phantom was used to detect mercury in the kidney (see Figures 1 and 2, Chapter 4). A large part of the detection system development was finding a suitable fit

function that described all of the mercury K x-ray photopeaks. The greatest challenge was fitting unresolved mercury photopeaks on a complex background generated by the approximately 180° Compton scatter of the 88.0 keV gamma-rays. The work presented in Article III succeeded in lowering the MDL to 3.9 ppm for bare kidney phantoms, which represents a more than a factor of 11 improvement over the ^{57}Co source-based system (Smith *et al.*, 1982). With the torso phantom in place, the MDL was determined to be 5.0 ppm at a 1 cm kidney depth. Correcting for the appropriate kidney depth, the MDL was comparable to the polarized systems, but for a lower estimated dose. With these improvements, the MDL of mercury is on the boundary of detectability for *in vivo* measurements and source-based XRF for *in vivo* mercury detection shows considerable promise.

Initial work on improving this MDL further employed ^{109}Cd source-excite XRF and a cloverleaf detection system with a higher source activity (Chapter 5) The cloverleaf detection system relies on the use of four smaller electronically separate HPGe detectors (each with 16 mm diameter and 10 mm thickness) that comprise the cloverleaf detector. With four sets of electronics, the system can process more events and a stronger source (up to about 10 GBq) can be used. The source strength at the time of these studies was 8 GBq, compared to 0.25 GBq used in the planar system. In addition, the resolution of the cloverleaf detectors is about 450 eV compared to 750 eV for the planar detector, meaning that less background is present under the mercury photopeaks, which reduces the MDL further. A significant improvement in MDL was expected (about a factor of 2) with the cloverleaf system, however for bare phantom measurements the improvement was more than a factor of 5. However, when the torso phantom was added to the system, the MDL did not improve compared to the planar detection system, and was still approximately 5 ppm at 1 cm depth in

the torso phantom. This was mainly due to increased background under mercury K x-rays from Compton scatter and detector pulse pile-up, which effectively canceled out the anticipated improvement gained by better resolution and the stronger source. The system did, however, prove to be very robust to various changes in shaping times, pile-up rejection settings, and small phantom position alterations. Future improvements to the cloverleaf system will focus on decreasing the background by designing the optimal source collimator length and source strength through Monte Carlo simulations.

In vivo measurements of two patients with possible mercury exposure were performed on the cloverleaf detection system in April of 2007. Patient 1 was occupationally exposed in the 1960's, and may have had symptoms related to mercury exposure. Patient 2 may have had a possible mercury exposure via a dental amalgam filling in 1998, with possible symptoms arising from this exposure. Each patient had a total of 4 body sites measured, including the liver and left kidney. Additionally, the temple and diaphragm of Patient 1, and the temple and tibia of Patient 2 were measured. No mercury was detected above the individual MDL in any of the sites measured, and there are several reasons for this. The time between exposure and measurement was quite long for both patients, and furthermore, the sensitivity of the current system may have been too low to detect mercury if present in trace amounts. In addition, the attenuation of mercury K x-rays by the bone at the temple site may have hindered the mercury signal, if in fact mercury was present. The current detection system has not been tested for *in vivo* measurements in non-soft tissue sites as the tibia and temple.

6.2 Future directions

6.2.1 Prompt gamma neutron activation analysis

An alternative method of detecting cadmium with neutron activation is to use the accelerator at the McMaster Accelerator Lab. The accelerator can produce neutron beams via the ^{7}Li(p,n)^{7}Be reaction. The main advantage of using an accelerator over the ^{238}Pu-Be source is that the neutron spectrum can be modified to contain more thermal or epithermal neutrons than fast neutrons by selecting appropriate proton energies. The ^{238}Pu-Be neutron source produces a broad neutron spectrum with a mean energy of 4 MeV, therefore many fast neutrons are present that contribute to a higher dose. Epithermal neutron energies are best, because they are moderated into the thermal region by the torso to undergo thermal neutron capture in the kidney or liver. If lower proton energies can be used to produce lower energy neutrons by the accelerator, then the dose-per-neutron captured can be lowered without decreasing the number of prompt gamma-rays from cadmium. This is especially the case for epithermal neutrons for which the neutron activation per unit dose is optimized. Neutron inelastic scatter from germanium in the detector would also be greatly reduced, resulting in smaller background and an improvement in the signal-to-background ratio in the gamma-ray spectrum. This will be especially true if the proton energies can be kept close to the reaction threshold, and hence generating neutrons with energies of less than 500 keV.

Another possibility with the accelerator would be to pulse the proton beam and thus the neutron beam from the accelerator. Smith *et al.*, 1982, reported using a pulsed beam, which was on for 15-25 μs with a repetition frequency of 6 kHz. A similar beam-pulsing technique can be employed, in which the acquisition system can

be off while the beam is on, reducing the number of gamma-rays from the target and from fast neutron slow-down. This is possible since thermal neutron lifetime is long (μs) compared to fast neutron slow-down time (ns). In 2007, a proton pulsing system was developed successfully at the KN accelerator beam line for neutron spectroscopy. It is expected that this pulsing system can be applied to *in vivo* PGNAA in the near future.

As part of system design, simulations would have to be carried out to determine shielding and beam collimation components. In particular, HPGe detector shields have to be designed to reduce possible neutron damage and neutron-related signals in the detectors. Also, optimal neutron beam collimation and neutron moderation has to be designed to reduce neutron energies such that the thermal neutron capture reaction rate is maximized in the kidney and liver. If successful, accelerator PGNAA would greatly reduce the background signal in the gamma-ray spectrum allowing a reduction in the detection limit of cadmium.

The improvements to PNGAA with the accelerator source to lower the detection limit of cadmium can be extended to mercury. In general, XRF is preferred for the detection of mercury, however, PGNAA may be useful for individuals with deep-lying kidneys. At larger depths, the detection limit may be better using accelerator PGNAA, especially with a pulsed neutron beam.

6.2.2 X-ray fluorescence of mercury

One alternative approach to source-excited mercury XRF is to use a source with a lower energy. Although the 88.0 keV ^{109}Cd source is close in energy to the K-edge of mercury at 83.1 keV (see Figure 1.8), there is a possibility of using a source that is even closer in energy to the K-edge. Other sources were considered (see Table 1.8),

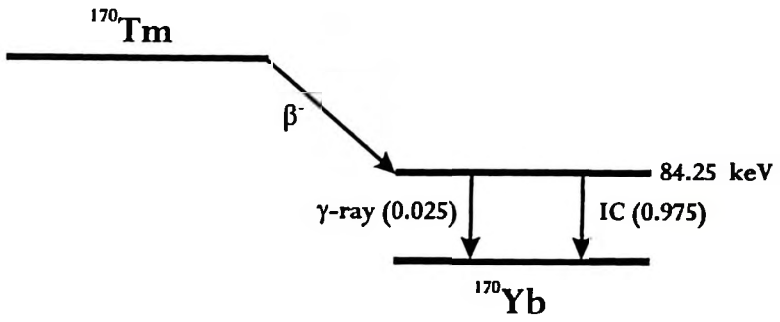

Figure 6.1: Decay scheme of ^{170}Tm (Table of Nuclides).

however, these had even higher energies than ^{109}Cd. Recently another source, ^{170}Tm, became a possibility for XRF due to the fact that it can be manufactured in the McMaster Nuclear Reactor. The thermal neutron cross-section for the ^{169}Tm(n,γ)^{170}Tm reaction is 105 b, which is quite large considering the natural abundance of ^{169}Tm is 100%. Thulium-170 has a half-life of 128.6 d and decays through β^- decay to ^{170}Yb (branching ratio of 99.869%), and through electron capture to ^{170}Er (0.131%). The main gamma-ray energy is 84.25 keV emitted in 2.5% of β^- decays, which comes from the de-excitation of ^{170}Yb (see Figure 6.1). Since the gamma-ray energy is closer to the K-edge of mercury, the photoelectric cross-section is larger at 84.25 keV (7.80 cm^2/g) than at 88.0 keV (6.96 cm^2/g). The slightly larger cross-section would improve mercury detection, but more importantly the Compton scatter peak energy would be lower in energy at 63.4 keV as opposed to 65.5 keV from ^{109}Cd. This would mean that the mercury K_α x-rays (69 and 71 keV) would be located further from the Compton peak and thus contribute more to lowering the detection of mercury by improving the peak-to-background ratio.

Another approach that may reduce the detection limit of mercury is polarized or direct-beam XRF with an x-ray therapy photon source. A new x-ray set for this purpose at the McMaster Accelerator Laboratory is coming online within the next year. This new system will have a variable voltage of up to 320 kV with a current

of 10 mA, and will be capable of generating a polarized, and possibly a direct beam. With a higher tube voltage than the previous system at McMaster (250 kV), the new system could reduce the detection limit of mercury via polarized XRF. If mercury sensitivity is still too low with polarized XRF, the next approach is to try direct excitation. A good example of this technique is an *in vivo* XRF study of platinum in the neck (Szaloki *et al.*, 1999). From Monte Carlo simulations, it is evident that the detection limit of mercury would be lowered at a cost of higher dose with direct excitation (O'Meara *et al.*, 2004). There is a possibility of reducing the dose with various filters while keeping the photon fluence high in the desired energy range.

Using x-ray optics is another possibility for XRF of mercury. X-ray optics have been used to focus and direct beams of x-rays for the purposes of material analysis and medical applications (Bjeoumikhov *et al.*, 2005, Gutman *et al.*, 2007). There are two main types of optical systems: polycapillary optics and doubly-curved crystal optics. In the first example, capillary tubes, usually carbon nanotubes, are used to direct x-rays generated by an x-ray tube (examples of anodes include Cr, Rh and Ag) through the process of total external reflection. Smaller capillary diameters can reflect higher energy photons, however, the reflection efficiency dramatically decreases with higher energies. Polycapillary optics are suitable for applications involving x-ray energies of less than 30 keV (Dabagov and Okotrub, 2004), therefore currently this method is not applicable to mercury since energies exceeding the K-edge at 83.1 keV are required. The second type of optical system utilizes a doubly curved crystal (for example Si) to focus x-rays from a source to obtain a highly monochromatic, intense and small area beam spot. Again, this method is not efficient for higher energy x-rays due to reduced reflection efficiency at higher energies (Lepy *et al.*, 2004). Optics for higher energy x-rays (60 to 100 keV) utilize transmission through two bent Si

Laue crystals and compound refractive lenses which collimate the beam exiting the liquid nitrogen-cooled Laue optics configuration (Shastri *et al.*, 2004). This system is capable of producing 81 keV x-rays with a flux of 10^{11} photons/s and beam size of 2 mm by 0.5 mm at the Advanced Photon Source (Argonne National Laboratory). Such an intense, small area beam may reduce the background under the mercury x-rays and significantly lower the detection limit. The development of high energy x-ray optics is ongoing, and these sytems are not commercially available as is the case for polycapillary optics and doubly curved crystal optical systems for lower energy x-ray applications. High energy x-ray optical systems in the mercury energy range may be more readily available in the future, and may prove to be the appropriate source of x-rays for the XRF of mercury in the kidney.

Future research opportunities described above can improve the non-invasive *in vivo* detection of the cadmium and mercury by prompt gamma neutron activation analysis and x-ray fluorescence. As the sensitivity of these methods increases in the future, *in vivo* measurement may someday be extended to monitoring environmental exposure to cadmium and mercury.

Bibliography

Barregard L, Sallsten G, Conradi N. (1999) Tissue levels of mercury determined in a deceased worker after occupational exposure. *Int. Arch. Occup. Environ. Health* **72** 169-173.

Berkeley National Laboratory Atomic Data: ie.lbl.gov/atom.htm.

Berkeley National Laboratory: ie.lbl.gov/ng.html.

Bevington PR. (1969) Data Reduction and Error Analysis for the Physical Sciences. McGraw Hill Inc., New York NY.

Bjeoumikhov A, Langhoff N, Bjeoumikhova S, and Wedell S.(2005) Capillary optics for micro x-ray fluorescence analysis. *Rev. Sci. Instrum.* **76** 76-82.

Block S, Bryan J, Prevo C, and Montan D. (1967) Laboratory sources enhanced in 0.5 eV to 200 keV neutrons for instrument evaluation. *Health Phys.* **13** 1025-1031.

Börjesson J, Barregard L, Sallsten G, Schutz A, Jonson R, Alpsten M, and Mattsson S. (1995) *In vivo* x-ray fluorescence analysis of mercury: the relation between concentrations in the kidney and in the urine. *Phys. Med. Biol.* **40** 413-426.

Börjesson J, Mattsson S, and Alpsten M. (1998) Trace Element Concentrations

Studied *In Vivo* Using X-ray Fluorescence Analysis. *Appl. Radiat. Isot.* **49** 437-445.

Christoffersson J-O and Mattsson S. (1983) Polarised x-rays in XRF-analysis for improved *in vivo* detectability of cadmium in man. *Phys. Med. Biol.* **28** 1135-1144.

Clarkson TW and Magos L. (2006) The Toxicology of Mercury and Its Chemical Compounds. *Crit. Rev. Toxicol.* **36** 609-662.

CRC Handbook of Chemistry and Physics (2007) 87th ed., Taylor and Francis Group, LLC.

Dabagov SB and Okotrub AV. (2004) On coherent scattering of x-ray in carbon nanotubes. *Spectrochim. Acta Part B.* **59** 1575-1580.

Fedorowicz RP, Chettle, DR, Kennett TJ, Prestwich WV, and Webber CE. (1993) A ^{238}Pu/Be facility for *in vivo* cadmium measurements. In *Human Body Composition*, eds. KJ Ellis and JD Eastman, Plenum Press, New York NY.

Friberg L. (1984) Cadmium and the Kidney. *Environ. Health Perspect.* **54** 1-11.

Grinyer GF. (2004) High precision measurements of ^{26}Na β^- decay. M.Sc. Thesis, University of Guelph.

Gutman G, Strumban E, Sozontov E, and Jenrow K. (2007) X-ray scalpel-a new device for targeted brachytherapy and stereotactic radiosurgery. *Phys. Med. Biol.* **52** 1757-1770.

Howe A, Fung LH, Lalor G, Rattray R, and Vutchkov M. Elemental composition of Jamaican foods 1: a survey and five food crop categories. *Env. Geochem. and*

Health. **27** 19-30.

IAEA Database for PGNAA: www-nds.iaea.org/pgaa/.

Kazantis G. (2004) Cadmium, osteoporosis and calcium metabolism. *BioMetals* **17** 493-498.

Kosta L, Byrne AR, and Zelenko V. (1975) Correlation between selenium and mercury in man following exposure to inorganic Hg. *Nature* **254** 238-239.

Mattsson S and Thomas BJ. (2006) Development of methods for body composition studies. *Phys. Med. Biol.* **51** R203-R228.

Marquardt DW. (1963) An algorithm for least-squares estimation of nonlinear parameters. *J. Soc. Indust. Appl. Math.* **2** 431-441.

McNeill FE and Chettle DR. (1998) Improvements to the *in vivo* measurement of cadmium in the kidney by neutron activation analysis. *Appl. Radiat. Isot.* **53** 699-700.

National Nuclear Data Center: www.nndc.bnl.gov.

Nie H, Chettle DR, Luo L, O'Meara J.(2006) *In vivo* investigation of a new ^{109}Cd γ-ray induced K-XRF bone lead measurement system. *Phys. Med. Biol.* **51** 351-360.

Lepy M-C, Ferreux L, and Plagnard J. (2004) A tunable monochromatic x-ray source for metrological studies in the 1-20 keV range: application to the measurement of attenuation coefficients. *Appl. Radiat. Isot.* **60** 159-165.

O'Meara JM, Börjesson J, and Chettle DR. (2000) Improving the *in vivo* X-ray

fluorescence (XRF) measurement of renal mercury. *Appl. Radiat. Isot.* **53** 639-646.

O'Meara JM, Börjesson J, Chettle DR, and McNeill FE. (2004) Optimization of an *in vivo* X-ray fluorescence mercury measurement system. *Nucl. Intr. and Meth. in Phys. Res. B* **213** 560-563.

Press WH, Teukolsky SA, Vetterling WT, and Flannery BP. (1992) *Numerical Recipes in C*, 2nd ed., Cambridge University Press, Cambridge.

Riget F, Muir D, Kwan M, Savinova T, Nyman M, Woshner V, and O'Hara T. (2005) Contaminants in the Canadian Arctic Biota and Implications for Human Health. *Sci. Total Environ.* **351-352** 312-322.

Satarug S and Moore MR. (2004) Adverse Health Effects of Chronic Exposure to Low-Level Cadmium in Foodstuffs and Cigarette Smoke. *Environ. Health Perspect.* **112** 1099-1103.

Smith JRH, Athwal SS, Chettle DR, and Scott MC. (1982) On the *in vivo* measurement of Hg using n capture and x-ray flourescence. *Int. J. Appl. Radiat. Isot.* **33** 557-561.

Somervaille LJ, Chettle DR, and Scott MC. (1985) *In vivo* measurement of lead in bone using x-ray fluorescence. *Phys. Med. Biol.***30** 929-943.

Szaloki I, Lewis DG, Bennett, CA, and Kilic A. (1999) Application of the fundamental parameter method to the *in vivo* x-ray fluorescence analysis of Pt. *Phys. Med. Biol.* **44** 1245-1255.

Table of Nuclides: atom.kaeri.re.kr/ton/nuc7.html.

Uetani M, Kobayashi E, Suwazono Y, Honda R, Nishijo M, Nakagawa H, Kido T, and Nogawa K. (2006) Tissue cadmium (Cd) concentrations of people living in a Cd polluted area, Japan. *BioMetals* **19** 521-525.

US Geological Survey: www.usgs.gov.

World Health Organisation (1976) *Environmental Health Criteria No. 1: Mercury.* World Health Organization, Geneva.

World Health Organisation (1991) *Environmental Health Criteria No. 118: Inorganic Mercury.* World Health Organization, Geneva.

Wittman R and Hu H. Cadmium Exposure and Nephropathy in a 28-Year-Old Female Metals Worker. (2002) *Environ. Health Perspect.* **110** 1261-1266.

XCOM Photon Cross-Sections Database: physics.nist.gov/PhysRefData/.

Appendix A

The Comparison of Two MCNP Models Used for Prompt Gamma *In Vivo* Detection of Cadmium and Mercury

The article included in this appendix is a result of research involving Monte Carlo simulations performed on the ^{238}Pu-Be neutron source and the thermal beam port at the McMaster Nuclear Reactor. The simulations are performed with MCNP (Version 5) and describe the expected relative reaction rates of cadmium, mercury and chlorine in a kidney phantom, and dosimetry calculations for both detection sites. The complete simulation of the detector spectrum was not performed as the gamma-production data for cadmium and mercury were not available in the current version of MCNP, therefore full comparison with experimental data of Article II was not possible. This research was a collaboration with my colleague Jovica Atanackovic, and

is a complement to Article II presented in Chapter 3.

Available online at www.sciencedirect.com
ScienceDirect
Nuclear Instruments and Methods in Physics Research B 263 (2007) 169–174
NIM B
Beam Interactions with Materials & Atoms
www.elsevier.com/locate/nimb

The comparison of two MCNP models used for prompt gamma in vivo detection of cadmium and mercury

J. Atanackovic *, J. Grinyer, D.R. Chettle, S.H. Byun

Department of Medical Physics and Applied Radiation Sciences, McMaster University, Hamilton, ON, Canada L8S-4K1

Available online 14 April 2007

Abstract

In vivo detection of trace elements is one of the most important research areas at the Medical Physics and Applied Radiation Sciences Department at McMaster University. Prompt gamma neutron activation analysis (PGNAA) used for detection of cadmium and mercury takes place simultaneously at two different experimental sites; the McMaster Nuclear Reactor (MNR) and the ^{238}Pu/Be neutron source site. This particular study consists of two parts. In the first part the water phantoms (125 mL) were used in MCNP simulations. The water phantoms were doped with different concentrations of Cd, Hg and HCl. This is done in order to compare the (n, γ) prompt gamma reaction rate; in fact, the rate of neutron capture by the nuclides of interest; ^{113}Cd, ^{199}Hg and ^{35}Cl. The second part involves, the neutron and photon dosimetry calculations that were performed for both sites using MCNP compatible body builder software developed in Los Alamos. The output of this program is the actual MCNP geometry description for various human anthropomorphic phantoms (different sex and ages). This phantom geometry output is incorporated into the original MCNP geometry and the dosimetry calculations were performed for various organs at risk.

Keywords: MCNP; Body builder cadmium; Mercury; Dosimetry

1. Introduction

At McMaster University, development work for in vivo prompt gamma activation analysis (PGNAA) is taking place at the thermal neutron beam at the McMaster Nuclear Reactor (MNR) and the ^{238}Pu/Be source at the Tandem Accelerator Laboratory. At both experimental sites, the detection of Cd and Hg is the main research area. Particularly, the detection of the most prominent prompt gamma lines of ^{113}Cd ($\sigma_0 = 20{,}600 \pm 400b$; $a = 12.22\%$) and ^{199}Hg ($\sigma_0 = 2150 \pm 48b$; $a = 16.87\%$) are 559 and 368 keV, respectively [1]. Note that σ_0 stands for the thermal neutron capture cross section and a stands for the isotopic abundance of a particular nuclide in the natural element. Cadmium and mercury are heavy metals that accumulate in the kidneys and liver, so the goal was to develop the experimental site which would be appropriate for measuring these elements. For every in vivo neutron activation analysis dosimetry is one of the main concerns, together with a minimum detection limit (MDL). However, the feasibility of the procedure itself depends on the dose received by the organs at risk, as well as the effective dose for the whole body. This further means that if a high dose is observed, the in vivo procedure would not be possible to perform, even if excellent detection limits are achieved. This particular study involves MCNP calculation of the neutron and photon doses for particular organs at risk; both kidneys, both testicles, liver and upper portion of the torso skin. Furthermore, this study observes the reaction rates of the neutron capture by the above nuclides, as well as the neutron capture of the ^{35}Cl nuclide ($43.6 \pm 0.4b$; $a = 75.77\%$) [1]. Extensive MCNP work was done on the thermal neutron MNR site, regarding source (sdef) card and the actual site geometry [2]. It was found that the neutron beam is rectangular, highly collimated (2.54×5.08) cm^2, with over 99% of the neutrons present being thermal [2]. The neutron energy dependence was

* Corresponding author.
E-mail address: atunacjz@mcmaster.ca (J. Atanackovic).

0168-583X/$ - see front matter © 2007 Elsevier B.V. All rights reserved.
doi:10.1016/j.nimb.2007.04.078

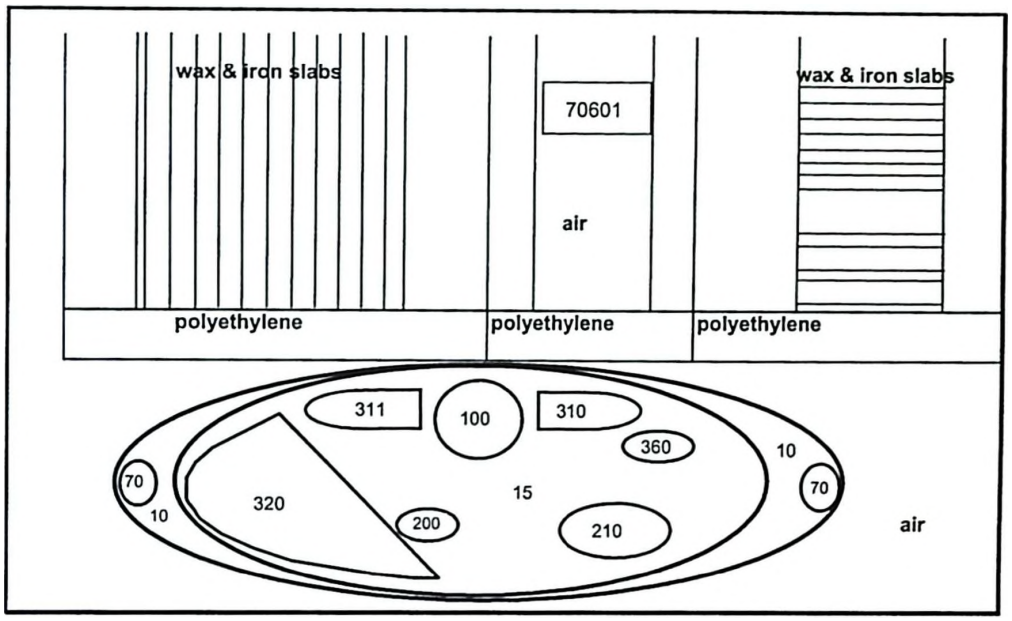

Fig. 1. MCNP geometry of body builder phantom and experimental site for ^{238}Pu/Be source ($pz = 32.5$ cm).

modeled using a Maxwellian distribution, with a total neutron fluence rate of 2.65×10^7 n/cm^2 s at the site [2]. Similarly, for the ^{238}Pu/Be site, the neutron point source is located in front of the Be moderator, at the center of the shielding depicted in Fig. 1. The total neutron source output is 4×10^7 n/s, with a neutron energy spectrum spanned between 0 and 11 MeV [3].

2. Materials and methods

In the first set of simulations; the rate of neutron capture by the given nuclides, the MCNP5 code was used [4]. For the second set of simulations; the dosimetry calculations, MCNP5 was used, together with the body builder code, developed in Los Alamos Laboratory [5]. It was shown elsewhere [2] that a concrete shielding (cave) surrounding the MNR experimental prompt gamma site had no influence on the MCNP output results, therefore, for this study those concrete walls were not included in the MCNP geometry. Also, the laboratory walls surrounding at the ^{238}Pu–Be experimental site were not included into the MCNP calculations since they were far away from the site and they also had no influence on final results.

The reaction rates (neutron capture rates by the above nuclides) at both experimental sites were tallied using f4 tally (average cell fluence), with appropriate fm4 multiplier cards, on 125 mL cylindrical water phantoms doped with different concentrations of Cd, Hg and Cl. The 125 mL phantoms were simulated because they were the best representation of the human kidney, where the actual measurement would have taken place. The Cd concentrations varied from 968 to 0 ppm, Hg concentrations varied from 2500 to 0 ppm, while Cl concentrations varied from 100,000 to 0 ppm. In the MNR case, the water phantom was in the direct neutron beam, while in ^{238}Pu/Be source case, the water phantom was in the water tank (torso simulation), but not in the direct neutron beam. This was done in order to resemble the real experimental setup.

These simulation were the precursors to further, detailed study that would hopefully resolve the discrepancy already encountered in detection limits for the above two nuclides. Particularly, it was found that detection limit for Hg was about 20 times worse than the detection limit for Cd, on both experimental sites while expected ratio should be around 10 [2,6]. The Cl reaction rates were calculated because it would be another comparison for Hg and Cd, since ^{35}Cl has a large number of well known prompt gamma lines of both low and high energies.

Moreover, the body builder code was used to establish the MCNP geometry for a human anthropomorphic male phantom, 21 years of age with all possible organs included. This geometry was incorporated into the already established MCNP geometry for both experimental sites. Figs. 1 and 2 show xy plane cross section ($z = 32.5$ cm) for two sites. From Fig. 2, we can see that the right kidney (cell 311) is located in the direct MNR neutron beam. The beam starts at 26 cm above the right kidney, at the upper face of the big wax shielding (cell 809) and it is parallel to the front face of the HPGe detector (cell 806). From Fig. 1, it is obvious that the left kidney is in the direct beam in ^{238}Pu/Be source case. The point source is located 6 cm above the Be moderator (cell 70601). The actual geometries for the sites are described in more detail elsewhere [2,7]. When the coupled MCNP and body builder geometry was set up for both sites, MCNP dosimetry runs were performed. For photon dosimetry cases, the f6 tally (energy deposition;

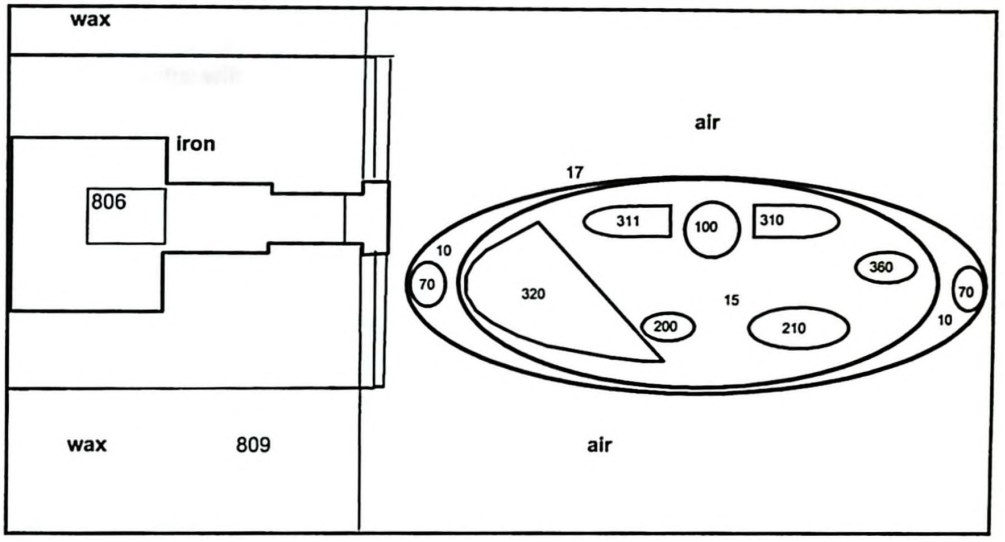

Fig. 2. MCNP geometry of body builder phantom and experimental site for MNR source ($pz = 32.5$ cm).

MeV/g) was used on all mentioned organs at risk. The f6 tally was further normalized using the fm6 input card in order to get the appropriate units for energy deposition rate (Gy/h), which is equivalent to Sv/h (for the photon dosimetry case only). Furthermore, these results were confirmed using *f8 tally (cell energy deposition in MeV). The neutron dose rate was calculated using f4 tally (average cell fluence; cm^{-2}), along with the appropriate fm4 multiplier card and dose equivalent per unit of neutron fluence (de4 and df4 cards) [8]. In the ^{238}Pu/Be case, a more complicated situation is observed, due to the wide spread of the neutron energy spectrum (0–11 MeV). Because of that, another run was performed for this experimental site. The neutron energy spectra were obtained in each organ of interest, using f4 card, together with appropriate fm4 card. The neutron energy steps were assigned according to ICRP recommendation for different neutron radiation weighting factors (see the first two columns in Table 4). This was done in order to benchmark MCNP calculations, using those results and dose equivalent per unit fluence table [8].

3. Results and discussion

3.1. Reaction rate results

As mentioned above, three nuclides of interest were observed. The results of the MCNP simulations are given in the Tables 1–3, for both experimental sites. Note that the relative MCNP errors are not included in the tables. For the MNR site, the errors are less than 0.13% for every run and for ^{238}Pu/Be site, the errors are less than 4.9%. There are three obvious features described in these tables. The first one is a highly linear relationship between the reaction rates and elemental concentrations for all three elements, for both sites. This is reasonable, since this is solely an MCNP calculation. The second one is the fact that much higher reaction rates are observed at the MNR site, because this site has much higher neutron fluence rates, compared to ^{238}Pu/Be site. The third obvious feature is that the highest reaction rates are observed in the ^{113}Cd

Table 1
The rate of neutron capture by ^{113}Cd

Cd concentration (ppm)	^{238}Pu/Be (s^{-1})	MNR (s^{-1})
968	4.32×10^3	2.19×10^7
642	2.87×10^3	1.48×10^7
379	1.69×10^3	8.89×10^6
170	7.59×10^2	4.02×10^6
57	2.54×10^2	1.37×10^6
0	0	0

Table 2
The rate of neutron capture by ^{199}Hg

Hg concentration (ppm)	^{238}Pu/Be (s^{-1})	MNR (s^{-1})
2500	6.71×10^2	3.49×10^6
1500	4.02×10^2	2.10×10^6
1000	2.68×10^2	1.40×10^6
500	1.34×10^2	7.04×10^5
200	5.37×10^1	2.82×10^5
100	2.68×10^1	1.41×10^5
0	0	0

Table 3
The rate of neutron capture by ^{35}Cl

Cl concentration (ppm)	^{238}Pu/Be (s^{-1})	MNR (s^{-1})
100,000	1.06×10^4	5.97×10^7
80,000	8.49×10^3	4.97×10^7
60,000	6.37×10^3	3.87×10^7
40,000	4.25×10^3	2.68×10^7
10,000	1.06×10^3	7.19×10^6
5000	5.31×10^2	3.64×10^6
0	0	0

case, because of its huge cross section for thermal neutrons (much higher than the Hg and Cl cross sections). These valid preliminary MCNP results will be used in further investigations of the prompt gamma line simulations, as well as possible detector modeling and calibrations for both experimental sites in order to assess the discrepancy between Hg and Cd detection limits mentioned above. There is one more feature of interest in this section that predominantly concerns the Cd and Cl reaction rate results at the MNR site. That is the presence of possible self-shielding and flux depression, which is common for elements with very high thermal neutron absorption cross section, like Cd [2,9]. In fact, it can also be seen from Table 3 that there is also a significant self-shielding and flux depression phenomena for Cl at the physiologically unrealistically high concentrations simulated here. Taking into the account the fact that neutron beam at the MNR site is highly thermal, the observed self-shielding and flux depression phenomena in the presence of ^{113}Cd are reasonable. Moreover, they were included in the calculations elsewhere [2]. Therefore, these MCNP calculations confirmed it. Particularly, if we extrapolate the straight line between 0 and 57 ppm phantom, we would obtain slightly higher results for higher concentration phantoms, compared to Table 1 results. For example for 968, 642, 379 and 170 ppm phantoms, we would obtain 6.4%, 4.1%, 2.5% and 1.7% higher results, respectively. Also in chlorine case, we encountered even higher discrepancies; for 10,000, 40,000, 60,000, 80,000 and 100,000 ppm phantoms we would obtain 1.3%, 8.7%, 12.9%, 17.1% and 21.9% higher results, respectively. The higher discrepancies for Cl case are reasonable, since huge concentrations of Cl were simulated. This is pictured in Figs. 3 and 4.

3.2. Dose rate results

The MCNP calculation of normalized number of neutrons for the four ICRP energy ranges (all organs of interest), for ^{238}Pu/Be site is given in Table 4. Again, the relative errors are not included, because they range between 0.5% and 3%. Evidently, from this table, the neutron energy spectrum is largely thermalized in each organ of interest. This is due to the presence of the Be moderator, as well as the moderation of the tissue itself. From the same table it can be seen that the first energy range ($W_R = 5$), for every organ of interest, consists of more than 50% of total number of neutrons (up to 86% for the right kidney). Another important feature is the absence of the testicle calculation. It was observed that MCNP does not sample for any neutrons in testicles, for both experimental sites. This means that neutron energy deposition for testicles is 0. However, we will see later that there is a significant photon energy deposition for testicles. This is predominantly due to 2.2 MeV hydrogen prompt gamma, as well as high energy prompt gammas from nitrogen in the tissue. The fact that we do not observe any neutron dose for testicles, tells us that as we go further away from the area that is hit by neutron beam (for both sites), the equivalent neutron dose becomes negligible, so we have to tally for photon dose only. This would save a huge amount of time for future MCNP dose calculations for other organs. Finally the dose rate (mSv/h) MCNP calculations are given in Table 5. The relative MCNP errors for these calculations varied from 0.1% to 2.7% for MNR site and from 0.2% to 4.4% for ^{238}Pu/Be site. As mentioned, no neutron dose for testicles is observed. The highest dose rate (neutron as well as photon), for MNR site is observed in the right kidney and the

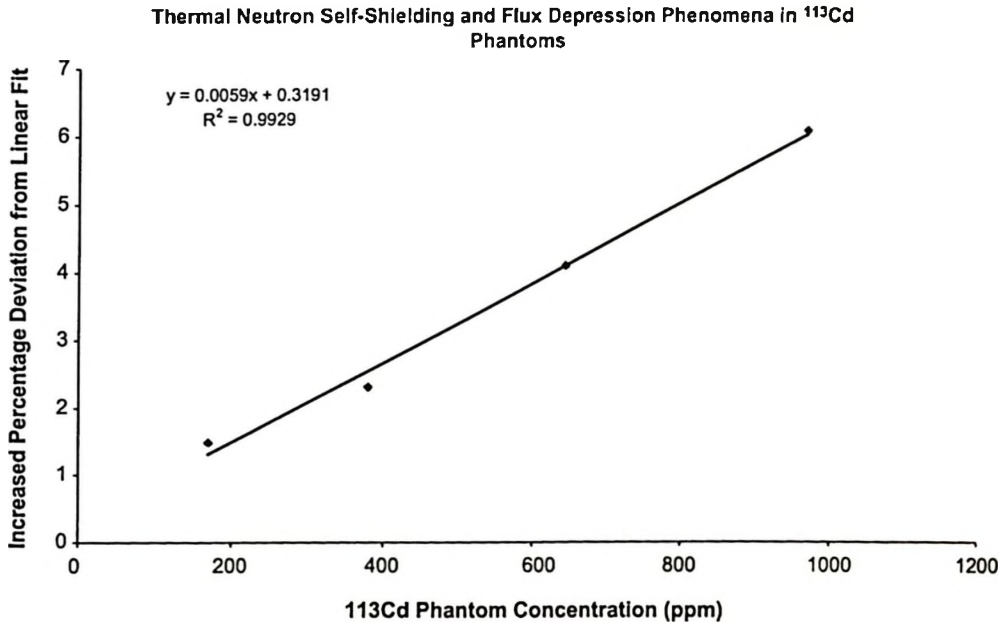

Fig. 3. Thermal neutron self-shielding and flux depression in ^{113}Cd phantoms.

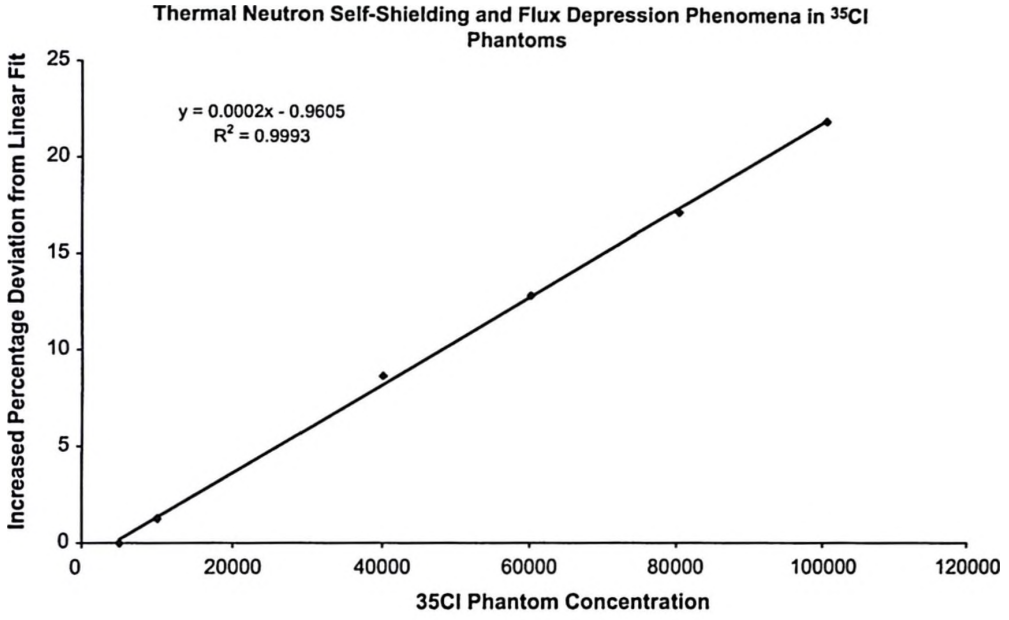

Fig. 4. Thermal neutron self-shielding and flux depression in ^{35}Cl phantoms.

Table 4
Relative number of neutrons in organs at risk for $^{238}Pu/Be$ experimental site

Interval (MeV)	W_R	Left kidney	Right kidney	Liver	Skin
0–0.01	5	0.700	0.861	0.838	0.520
0.01–0.1	10	0.053	0.028	0.020	0.096
0.1–2	20	0.145	0.069	0.072	0.248
2–20	10	0.101	0.042	0.070	0.136

Table 5
MCNP dosimetry results (mSv/h)

	MNR (n)	MNR (γ)	$^{238}Pu/Be$ (n)	$^{238}Pu/Be$ (γ)
Right kidney	213.28	19.478	0.125	0.035
Left kidney	2.24	1.512	2.230	0.066
Liver	6.05	2.357	0.038	0.016
Skin portion	4.99	0.685	0.108	0.014
Testicle 1	0	0.079	0	0.003
Testicle 2	0	0.084	0	0.003

highest dose rate for $^{238}Pu/Be$ is observed in the left kidney. This is reasonable, since these features are actually in the direct neutron beam. Furthermore, the neutron doses are confirmed for both sites by benchmarking, using the MCNP output (described above) for neutron energy spectra. It was found that MNCP calculations agree with benchmark calculation within less than 1% for the MNR site and within 7% for the $^{238}Pu/Be$ site. Obviously, approximately 100 times higher doses are observed at the MNR site (right kidney), compared to the $^{238}Pu/Be$ source (left kidney) because of the higher neutron fluence rate at this experimental site. It should be noted that skin dose rate is averaged over the whole volume of the upper torso skin, while only a small portion of it is hit by the neutron beam, for both cases. Therefore, the area that is hit actually receives a much higher dose than this calculated averaged dose.

Evidently, the dose rates are calculated using the dose equivalent per unit of neutron fluence table, which is based on the ICRP60 step function, described in Table 4 (first two columns). This step function is approximated by a continuous function [10]:

$$w_R = 5 + 17e^{\left(\frac{-(\ln 2E_n)^2}{6}\right)} \quad (1)$$

This would obviously give a radiation weighting factor of 5 for neutrons between 0 and 0.01 MeV. However, a new ICRP [9] recommendation for neutron radiation weighting factor is given by the approximation:

$$w_R = 2.5\left(2 - e^{-4E_n} + 6e^{-(\ln(E_n)^2/4)} + e^{-(\ln(E_n/30)^2/2)}\right) \quad (2)$$

Evidently, this would give a radiation weighting factor of 2.5 for neutrons between 0 and 0.01 MeV (thermal neutrons). Therefore, this would significantly lower the neutron portion of the dose for MNR experimental site, since the neutron beam consists of more than 99% thermal neutrons. Therefore, the neutron dose on MNR site would approximately be half of the value that is calculated here. However, for $^{238}Pu/Be$ site, it was found, by benchmark that only about 8% of the neutron dose is due to thermal neutrons, regardless of the fact that about 70% of the beam is thermalized by the time it comes to the left kidney. This is due to a much higher radiation weighting factors for higher energy neutrons, as well as the greater energy depos-

ited per neutron. Therefore, this tells us that lowering the radiation weighting factor in this case would not decrease the neutron dose significantly.

4. Conclusion

The reaction rates of three nuclides of interest give highly linear relationship with respect to the elemental concentration in the sample. Expected results are obtained using MCNP calculations. However, it was found that there are a flux depression and self-shielding phenomena present at the MNR experimental site, especially for ^{113}Cd and ^{35}Cl phantoms. These MCNP results confirmed the calculations obtained in publication [2]. The results for the Cd case are reasonable, since the neutron beam at this experimental site is 99.96% thermal [2]. They are also reasonable for the Cl case, since huge concentrations were simulated. The reaction rate results will be compared with further MCNP calculations regarding emission of prompt gamma rays of interest for all three nuclides, as well as potential MCNP detector calibration, used for in vivo measurements at both experimental sites.

Reasonable neutron and photon dose rates are observed for five organs that were investigated in this project at the ^{238}Pu/Be site and if desired detection limits are observed for Cd and Hg, the site could be used for vivo measurements. Also, the reasonable doses are observed in MNR case for left kidney, skin, both testicles and liver. However, the high neutron dose rate of 213 mSv/h is observed in the right kidney at the MNR site and because of that the MNR site would not be recommended for in vivo measurements, regardless of the excellent detection limits that are obtained for Cd and Hg [2]. Particularly, the normalized Cd MDL for 125 mL phantoms (in terms of MDL $\times$ (dose)$^{1/2}$) was found to be 0.697 mg(mSv)$^{1/2}$ and 1.107 mg(mSv)$^{1/2}$ for MNR and ^{238}Pu/Be site, respectively [2,6]. This is normalized for a 30 min exposure at both experimental sites. Evidently, a better normalized MDL was obtained at the MNR site, however, the absolute neutron dose to the right kidney is the problem and that is the reason why the MNR site could not be recommended for in vivo usage at this stage. However, it should be noted that the reaction rate, admittedly for a bare phantom, was about 5000 times higher at the MNR site than the ^{238}Pu/Be for either Cd or Hg; whereas the dose in kidney was only 100 times higher. This implies that it will be valuable to continue to investigate the MNR site for potential in vivo measurements. Also, a lower energy source of neutrons than the present ^{238}Pu/Be can be expected to produce improvements, since more than 90% of dose derives from 30% of neutrons with energies greater than 0.01 MeV. As far as further MCNP – body builder calculations are concerned, there is obvious evidence that it is not necessary to tally for neutron dose far away from the area that is actually hit by the neutron beam. This fact holds for both experimental sites and this would save a significant amount of computer time.

References

[1] Brookhaven National Laboratories, National Nuclear Data Cente Available from: http://www.nndc.bnl.gov/.
[2] J. Atanackovic, Optimization of the prompt gamma site at the McMaster Nuclear Reactor for in vivo neutron activation analysis, MSc Thesis, McMaster University, 2004.
[3] S. Block, J. Bryan, C. Prevo, D. Montan, Laboratory sources enhanced in 0.5 eV to 200 keV neutrons for instrument evaluation, Health Phys. 13 (9) (1967) 025.
[4] X-5 Monte Carlo Team, MCNP – A general Monte Carlo N-particle transport code manual, Version 5, Vol. 1, Los Alamos National Laboratory, 2003.
[5] Body Builder for Windows, Version 1.30, manual, White Rock Science, 2004.
[6] J. Grinyer, J. Atanackovic, S.H. Byun, et al., Phantom studies of Cd, Hg and Cl by prompt gamma neutron activation analysis using the ^{238}Pu–Be Source, IRRMA Conference, Hamilton, ON, Canada, submitted for publication.
[7] J. Grinyer, S.H. Byun, D.R. Chettle, Appl. Radiat. Isotopes 63 (2005) 475.
[8] NCRP 38 (10CFR835), Neutron dose equivalent per unit fluence.
[9] Technical Report Series No. 107, Neutron fluence measurements, International Atomic Energy Agency (IAEA), Vienna, 1970.
[10] ICRP: Relative biological effectiveness (RBE), quality factor (Q), and radiation weighting factor (w_R), 33 (4) (2003).